Experimental Study of the ^{3}He and Neutron Spin Structure at Low Q^2 and The Upgrade of the JLab Polarized ^{3}He Target

Nguyen Nu Thi Ton

Hue, Vietnam

B.S., Hue University's College of Education, 2011

A Dissertation presented to the Graduate Faculty

of the University of Virginia in Candidacy for the Degree of

Doctor of Philosophy

Department of Physics

University of Virginia

December, 2019

Dedicated to my parents Phu and Bao

Abstract

In the scattering process off a nuclear or nucleon target, the Gerasimov-Drell-Hearn (GDH) sum rule for real photons (Q^2=0 where $Q^2 \equiv -q^2$ with q the photon's 4-momentum) relates static properties of the target particle's ground state to dynamic properties of all its excited states. On the other side of the Q^2 spectrum, the Bjorken sum rule holds in the Bjorken limit $Q^2 \to \infty$. Bjorken sum rule relates the final structure functions of the proton and neutron to the nucleon axial coupling constant in weak decay. These two sum rules belong to domains where calculations are achievable but use different degrees of freedom: hadronic degrees of freedom at low Q^2 versus partonic degrees of freedom at intermediate Q^2. Meanwhile, different methods have been used to connect the two sum rules at finite Q^2 values: Chiral Perturbation Theory is used to expand the GDH sum rule while Operator Product Expansion is used to expand the Bjorken sum rule.

In recent decades, improvements in polarized beam and polarized target techniques have made it possible to test theoretical predictions in the intermediate Q^2 region. During the Jefferson Lab (JLab) Hall A E97110 experiment, a precise measurement of polarized cross sections was performed at $0.02 < Q^2 < 0.3$ GeV^2 using a polarized ^{3}He target as an effective polarized neutron target. The measured data allowed us to test predictions of Chiral Perturbation Theory at very low Q^2. Furthermore, an extrapolation to the real photon point Q^2=0 tests the GDH sum rule on the neutron.

In order to reach the small angles necessary for the low Q^2 range, a new septum magnet was installed in Hall A for this experiment. Unfortunately, the magnet was mis-wired during initial running. There were therefore two periods for this experiment: the first period had the defective magnet due to mis-wiring; while in the second period, the magnet had been fixed and was working properly. The cross sections and the asymmetries for the first period must be extracted using a difficult and unusual method employing focal plane variables in the spectrometer. In the work described in this thesis, the target-plane and focal-plane method will be established first and

confirmed by elastic scattering cross section measurements from carbon foil and ^{3}He targets. Cross sections and asymmetries of inelastic scattering were then extracted using the same method, which constitute the main physics results of this thesis. Preliminary results on I_{TT}, the integral of the polarized cross section, were also extracted and are presented in this thesis.

In addition to the data analysis of E97110, this thesis includes instrumentation work performed on the polarized ^{3}He target at JLab. For the 12 GeV program of JLab, the polarized ^{3}He target is being upgraded to satisfy new experimental requirements. The new target is a convection-based cell with two transfer tubes rather than a single transfer tube as in the former 6 GeV design. The first stage of the target upgrade aims to produce a 40 cm long, 10 amg target that can withstand 30 μA of electron beam current with an in-beam polarization of 55%, doubling the figure-of-merit from the 6 GeV time. Several studies were conducted at the Test Lab of JLab on the new convection cell. Work and improvement done on the Pulse Nuclear Magnetic Resonance (NMR) polarimetry and its test results will be presented. As this thesis is written, the target is being installed in Hall C of JLab in preparation for a 6-month long running from November 2019 to May 2020.

Acknowledgments

Deciding to do Ph.D is one of the right decisions in my life. In this long journey, I would never succeed without support, help from people surrounding me. I would like to take this opportunity to express my appreciation to all of those who guided me through this exciting journey.

I would like to thank Alexandre Deur, Kent Paschke, Nilanga Liyanage, Tai Melcher, and Xiaochao Zheng for being my committee members.

First of all, I would like to thank my advisor, Xiaochao, for her support and advising. She would always join my weekly meeting and give me suggestion and guidance, and make sure that I follow the plan. Sometimes I got lost, then she would bring me back and give me motivation to move forward. I'm also thankful for her help in correcting many versions of my thesis, it would not look this perfect without her continuous feedback. She set an example for me to believe that one can pursue their passion in career and family at the same time.

I would like to thank Alexandre for being my supervisor at JLab and giving me the chance to work on this challenging project. I remember discussing about the strong coupling constant with him, those discussions made me more interested in physics. He would always give me suggestions and guidance to solve problems I encountered in the analysis.

I would like to thank Jianping Chen for supervising me on both the analysis and the target work. He taught me to multitask and be the expert of what I do.

I would like to thank Kent for always giving me positive feedback for my talk. Those words encouraged me a lot.

I would like to thank Nilanga for supervising me on the HRS optics optimization. I thank him for taking time out of his busy schedule to give me directions, I am impressed by his expertise in optics. And he is a very kind person too.

I would like to thank Vincent Sulkosky for his endless patience. He is one of the kindest people that I know. He would always respond to my emails and never hesitate to give me a hand. Without his help, I would not be able to progress this fast. He

gave me all details and status of the analysis, so I could catch up quickly.

I would like to thank P.Q Hung for introducing me to the Ph. D program. I would never have thought I could obtain a doctor degree abroad without his guidance.

I would like to thank my peers during graduate school. Thanks Hien Nguyen, Nhan Pham, and Sharmistha Sahoo for always being by my side and providing strong support, and for believing in me. I thank Dien Nguyen, Trinh Le and my Vietnamese friends group for fun time we had together.

Lastly, I want to thank Jie Liu for being with me through the good and the challenging times.

This work was supported by Graduate Fellowships from Department of Physics at the University of Virginia and Jefferson Science Association, and Department of Energy, Office of Science, under Award DE-SC0014434.

Contents

List of Figures

List of Tables

Chapter 1

Spin Structure of the Nucleon and the GDH Sum Rule

In this chapter, we will first discuss the formalism for inclusive electron scattering off a nucleus. The internal structure of the nucleon is parameterized by structure functions (inelastic case) or form factors (elastic case). Next, we will examine the theoretical methods that are used to derive the GDH sum rule for real photons. Then we will discuss generalization of the GDH sum rule to virtual photons. After the presentation of the sum rules, we will discuss GDH sum rule results from previous experiments and the importance of the experiment being presented in this thesis.

1.1 Introduction

Protons and neutrons are the building blocks of the atomic nucleus. They are not fundamental particles, and they have a structure. Exploring the nucleon structure is important to our understanding of the structure of matter as more than 99.9% of the mass of any visible object in our daily life is carried by its nucleons. In 1964, M. Gell-Mann and G. Zweig proposed that nucleons are in fact composed of quarks, which are point-like charged particles [1, 2]. This was confirmed experimentally in the 1970s using electron scattering at SLAC.

Among all nucleon properties, understanding its spin constitution is particularly

interesting. The fundamental question we try to answer is: "how do quarks and gluons make the spin of the nucleon?". The nucleon has spin $s = 1/2$. It was originally expected that the quark spins carried most of the nucleon spin, about 70%, with the ∼30% remainder coming from the quark angular orbital momentum. However, experiments at SLAC [3] and CERN [4] performed in the late 1980s and early 1990s contradicted this expectation. The experimental results suggested that only a small percentage of the nucleon spin is carried by the spins of the quarks. This disagreement surprised physicists and is sometimes referred to as "the proton spin crisis". After decades of efforts, both theoretical and experimental, the current understanding is that the quark spins contribute to about 30% of the nucleon spin [5]. Other contributions, specifically the gluon spin and the orbital angular momenta of gluons and quarks, are important.

The following sections will give an introduction about electron scattering, then provide the theoretical background and motivation for the neutron spin structure experiment that is the main subject of this dissertation.

1.2 Electron Scattering

Electron scattering is one of the most important experimental tools to probe the structure of matter. One advantage of doing electron scattering is its accuracy. Firstly, the electromagnetic interaction is weak enough to allow us to treat it perturbatively, the only well-controlled analytic method that is available to us in a quantum field theory. Secondly, it is strong enough that it dominates the weak interaction. Thus electron scattering can be accurately described by the electromagnetic interaction, which is calculable with well-understood Quantum Electro-Dynamics (QED).

The first Born approximation (one photon exchange process) for inclusive scattering[1] of an electron from a nucleon target is shown in Fig. 1-1, where k^μ and k'^μ are the four-momenta of the incoming and outgoing electrons, respectively. Similarly, P^μ and P'^μ refer to the momenta of the nucleon. For inclusive scattering experiments, the

[1] An inclusive scattering is a process in which only the scattered electron is detected.

incoming, outgoing electron momenta and the scattering angle θ are measured. The unknown photon-nucleon vertex in the Feynman diagram depends on two kinematic quantities of the virtual photon: the momentum transfer $Q^2 \equiv -q^2$ with $q = k - k'$ the 4-momentum of the photon (the photon is off mass shell and thus $Q^2 \neq 0$) and the energy transfer $\nu = q \cdot P/M$ where M is the target mass. In the laboratory frame, the target stays at rest, $P^\mu = (M, 0)$ and

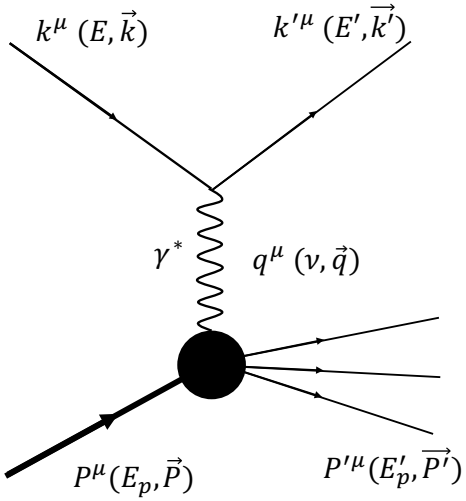

Figure 1-1: One photon approximation of e-N scattering.

$$Q^2 = 4EE' \sin^2(\theta/2), \tag{1.1}$$

and ν is the electron energy loss:

$$\nu \equiv E - E'. \tag{1.2}$$

The invariant mass is[2] defined by

[2]The invariant mass is the total mass of outgoing particles that are not detected in the inclusive scattering process. It is a relativistically invariant quantity and does not depend on the overall motion of the frame.

$$W \equiv \sqrt{M^2 + 2M\nu - Q^2}. \tag{1.3}$$

Another variable is the Bjorken scaling variable

$$x = Q^2/2M\nu, \tag{1.4}$$

which in the parton model, see Section 1.3.3, is interpreted as the fraction of the nucleon momentum carried by the struck quark. For elastic scattering on the nucleon, $W = M$ and thus $x = 1$, whereas for a nuclear target with A nucleons, $x = A$, for the elastic kinematics.

The virtual photon reveals the target's structure. By varying the squared momentum Q^2 and energy ν, one can obtain the excitation spectrum of the target as shown in Fig. 1-2. The spectrum displays elastic scattering, quasi-elastic scattering (present for nuclear target only), the resonance region and the deep inelastic region. We characterize these reactions as follows:

- Elastic scattering: $Q^2 = 2M_A\nu$, where M_A is the nuclear mass. Electrons are elastically scattered off a nuclear target (for a nucleon target, the target mass is the nucleon's mass). The target nucleus stays intact and reacts coherently. The momentum transfer is shared among all the nucleons (or quarks, if the target is a nucleon) and all the nucleons stay in their ground states.

- Quasi-elastic: When ν reaches a certain value, one of the nucleons can be knocked out from the target while the electron elastically scatters off that nucleon. This process is called quasi-elastic scattering. Due to Fermi motion, the cross-section peak appears broadened compared to elastic case. Elastic and quasi-elastic scatterings are parameterized by elastic form factors and response functions, respectively.

- Resonances: At higher excitation energy, nucleon resonances start to appear in the excitation spectrum. In region $1.2 < W < 2.0$ GeV/c^2, the virtual photon starts to be sensitive to individual quarks. It is absorbed by these quarks

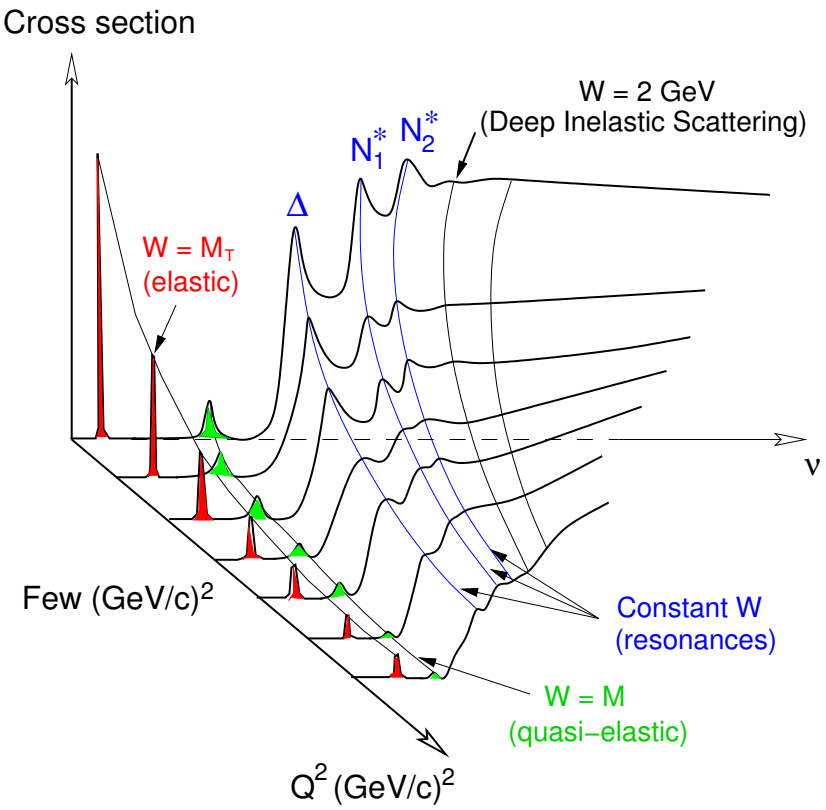

Figure 1-2: A cartoon of cross section as a function of Q^2 and ν for inclusive electron scattering off a nuclear target [6]. M_T is the target mass, M is the nucleon mass, and W is the invariant mass. The excitation peak positions (N, Δ, ...) change when Q^2 and ν change but stay at constant W. For nucleon targets, there is no quasi-elastic peak.

and produces excited states called "nucleon resonances". The first resonance is the $\Delta(1232)$. In inclusive scattering, the numerous other resonances are not as clearly seen as the Δ due to their overlap and a non-resonance background. The region between the quasi-elastic and the Δ-resonance is called the dip region.

- Deep inelastic scattering (DIS): With large enough Q^2 and ν, enters the DIS region, dominated by scattering off quasi-free individual quarks[3]. In this region, the dimensionless Bjorken scaling variable, x, is enough to characterize the reaction to the first order. This is the phenomenon of "Bjorken Scaling".

[3]At large Q^2 (small space-time) interval, the strong coupling constant α_s is small: quarks barely interact with each other and can be considered as quasi-free.

1.3 Structure Functions

In elastic scattering, the target reacts as a whole to the probing electromagnetic field and the target structure is unaffected by the probe. At long distance scales (i.e very low Q^2 and ν) the scattering is approximated by Rutherford scattering [7]. At JLab's energies, however, the exact expression is necessary. The kinematical aspect of the scattering is given by Mott scattering [8] while the structure information of the target is given by nuclear or nucleon form factors. For the inclusive inelastic spectrum, structure functions are used to describe the structure of the target.

1.3.1 Unpolarized Structure Functions

In the laboratory frame, the differential cross section for inelastic scattering of an electron from an unpolarized target is [10]:

$$\frac{d^2\sigma^{unpol}}{d\Omega dE'} = \left(\frac{d\sigma}{d\Omega}\right)_{Mott}\left[2W_1(\nu, Q^2)\tan^2\frac{\theta}{2} + W_2(\nu, Q^2)\right], \tag{1.5}$$

where $(\frac{d\sigma}{d\Omega})_{Mott} = \frac{4\alpha^2 E'^2\cos^2(\theta/2)}{Q^4}$ is the cross section for scattering an electron off a point-like spin-zero target, α is the fine structure constant[4]. W_1 and W_2 are the structure functions that contain information about the target's internal structure.

W_1 and W_2 are usually rewritten in term of two dimensionless structure functions, which depend on Q^2 and the Bjorken variable x:

$$\begin{aligned} F_1(x, Q^2) &= MW_1(\nu, Q^2), \\ F_2(x, Q^2) &= \nu W_2(\nu, Q^2). \end{aligned} \tag{1.6}$$

Both $F_{1,2}$ and $W_{1,2}$ are called unpolarized structure functions (or spin-independent structure functions).

[4]The usual value $\alpha = \frac{e^2}{4\pi\epsilon_0\hbar c} = \frac{1}{137}$ is still valid at JLab's energies.

1.3.2 Polarized Structure Functions

When we take into account the target spin orientation, the difference between the cross section when the electron helicity[5]($\rightarrow$) is parallel to the target spin ($\Rightarrow$) and the one when the electron helicity is anti-parallel to the target spin ($\Leftarrow$) can be expressed as follows [10]:

$$\frac{d^2\sigma^{\rightarrow\Leftarrow}}{d\Omega dE'} - \frac{d^2\sigma^{\rightarrow\Rightarrow}}{d\Omega dE'} = \frac{4\alpha^2 E'}{M\nu Q^2 E}\Big[(E + E'\cos\theta)g_1(x,Q^2) - 2Mxg_2(x,Q^2)\Big], \tag{1.7}$$

where g_1, g_2 are polarized structure functions (or spin-dependent structure functions). In the DIS limit, the longitudinal quark polarization in the nucleon is described by g_1 and their transverse polarization is described by $g_1 + g_2$. From Eq. 1.7, the first term in the bracket dominates when $E \gg M_{target}$, and g_2 contributes to second order.

With a transversely polarized target, the cross section difference becomes:

$$\frac{d^2\sigma^{\rightarrow\Uparrow}}{d\Omega dE'} - \frac{d^2\sigma^{\rightarrow\Downarrow}}{d\Omega dE'} = \frac{4\alpha^2 E'^2}{M\nu Q^2 E}\Big[g_1(x,Q^2) + \frac{2E}{\nu}g_2(x,Q^2)\Big]\sin\theta. \tag{1.8}$$

Equations 1.7 and 1.8 allow one to determine g_1 and g_2 independently if measurements are done for both longitudinally and transversely polarized targets.

1.3.3 Structure Functions in the Quark-Parton Model

The quark-parton model is a theoretical model to describe the nucleon's properties in the DIS limit[6] (this model is not derived from the fundamental theory of QCD). It provides an interpretation of the Bjorken x and of the structure functions. In the quark-parton model, the nucleon is considered as a collection of non-interacting, point-like constituent partons (later identified with QCD's quarks and gluons). Here, a quark which carries a x fraction of nucleon's momentum can absorb a virtual photon if the photon and quark helicities satisfy the helicity conservation law. In the parton

[5]Helicity is defined as $\frac{\vec{s}\cdot\vec{p}}{|\vec{s}||\vec{p}|}$, the spin orientation of the particle with respect to its direction of motion.

[6]The DIS limit is defined so that $Q^2 \to \infty, \nu \to \infty$ but $\frac{Q^2}{\nu}$ is finite.

model, the nucleon's DIS cross section is the sum of the elastic cross sections of individual partons. Therefore, the spin-average quark distribution $F_1(x)$ (corresponding to quark's momentum distribution) and the spin-dependent quark distribution $g_1(x)$ (corresponding to quark's polarization distribution) can be written as [10]

$$F_1(x) = \frac{1}{2}\sum_i e_i^2 q_i(x) = \frac{1}{2}\sum_i e_i^2 [q_i^{\uparrow}(x) + q_i^{\downarrow}(x)], \tag{1.9}$$

$$g_1(x) = \frac{1}{2}\sum_i e_i^2 \Delta q_i(x) = \frac{1}{2}\sum_i e_i^2 [q_i^{\uparrow}(x) - q_i^{\downarrow}(x)], \tag{1.10}$$

where $q_i^{\uparrow}$ ($q_i^{\downarrow}$) is the probability that the spin of a quark of flavor i and carrying a momentum ratio x is aligned parallel (anti-parallel) to the nucleon spin.

In the DIS (or Bjorken) limit, helicity conservation yields the Callan-Gross relation [11], which relates the two unpolarized structure functions as follows:

$$F_2(x) = 2xF_1(x). \tag{1.11}$$

The scaling behavior of structure functions and the above relations are exact only in the Bjorken limit, however, and are only approximative at finite Q^2. The Q^2 evolution equations of parton distribution functions were first derived by Dokshitzer, Gribov, Lipatov, Altarelli, and Parisi (DGLAP equations) [12], which add in radiative corrections due to soft gluon contributions. At lower Q^2, one can use Operator Product Expansion (OPE) method [13] to conduct nonperturbative calculations of quantum field theory where the higher twist corrections and radiative corrections can be separated.

1.4 Real Compton Scattering

The forward Compton scattering amplitude of a photon from a nucleon can be written as follow [10]:

$$T(\nu, \theta = 0) = \vec{\epsilon}^{\prime *} \cdot \vec{\epsilon}\, f(\nu) + i\vec{\sigma} \cdot (\vec{\epsilon}^{\prime *} \times \vec{\epsilon})\, g(\nu), \tag{1.12}$$

where $\vec{\epsilon}$ and $\vec{\epsilon}^{*\prime}$ are the incoming and outgoing photon polarization vectors respectively. Here the incident photon is characterized by the 4-vectors of momentum $q = (q_0, \vec{q})$, and of polarization $\epsilon = (0, \vec{\epsilon}^{\prime})$[7]. The kinematic of the outgoing photon is described by the primed quantities, and $\vec{\sigma}$ is the nucleon spin operator. Equation 1.12 introduces the spin-flip amplitude $g(\nu)$ and the non-flip amplitude $f(\nu)$. The derivation of Eq. 1.12 assumed invariance under rotational and parity transformations. In addition, crossing symmetry was imposed, which implies that Eq. 1.12 is invariant under the transformations $\epsilon' \leftrightarrow \epsilon$ and $\nu \leftrightarrow -\nu$. Hence, $f(\nu)$ is an even function and $g(\nu)$ an odd function, and can be written as follows:

$$\begin{aligned} f(\nu) &= \frac{1}{2}(T_{1/2} + T_{3/2}), \\ g(\nu) &= \frac{1}{2}(T_{1/2} - T_{3/2}), \end{aligned} \tag{1.13}$$

where $T_{3/2,1/2}$ are the scattering amplitudes of the photon-nucleon system with the subscripts $3/2$ or $1/2$ denoting the photon-nucleon system's total helicity.

1.5 Virtual Photon Cross Sections

The inclusive scattering cross section can be written either in term of the four structure functions $F_{1,2}$, $g_{1,2}$, or in term of four virtual photon absorption cross sections [14] as follows:

$$\frac{d\sigma}{d\Omega dE'} = \Gamma\Big(\sigma_T + \epsilon\sigma_L + hP_x\sqrt{2\epsilon(1-\epsilon)}\sigma'_{LT} + hP_z\sqrt{1-\epsilon^2}\sigma'_{TT}\Big), \tag{1.14}$$

[7] For real photon $q \cdot q = 0$ and $\epsilon \cdot q = 0$, which represents transverse polarization.

where $\sigma_{T,L}$ are the absorption cross sections for the transverse and longitudinal virtual photons, respectively. These two cross sections can be obtained from an unpolarized experiment. $\sigma'_{LT,TT}$ are the spin-dependent terms arising in a doubly polarized experiment. They represent the interferences of the amplitudes for longitudinal and transverse photon absorption, and for transverse and transverse photon absorption, respectively. P_x (P_z) is the target polarization parallel (perpendicular) to the virtual photon momentum. $h = \pm 1$ refers to the helicity of the longitudinal polarized electrons. ϵ is the ratio of the longitudinal to transverse polarization components of the virtual photon:

$$\epsilon = \left[1 + 2(1 + \frac{\nu^2}{Q^2}) \tan^2 \frac{\theta}{2}\right]^{-1}, \tag{1.15}$$

and Γ is the flux factor:

$$\Gamma = \frac{\alpha}{2\pi^2 Q^2} \frac{E'}{E} \frac{K}{1-\epsilon}, \tag{1.16}$$

where K is the virtual photon flux for which several convections exist [14] .

The total helicity cross sections are related to the transverse (σ_T) and the "transverse-transverse" (σ'_{TT}) cross section as follows:

$$\begin{aligned} \sigma_T &= \frac{\sigma_{3/2} + \sigma_{1/2}}{2}, \\ \sigma'_{TT} &= \frac{\sigma_{3/2} - \sigma_{1/2}}{2}, \end{aligned} \tag{1.17}$$

where $\sigma_{3/2,1/2}$ are the helicity-dependent photo absorption cross sections and the subscripts refer to total helicity projections of the photon plus target helicities.

These virtual photon absorption cross sections are related to the nucleon structure

functions as follows [15]:

$$\begin{aligned}
\sigma_T &= \frac{4\pi^2\alpha}{MK}F_1, \\
\sigma_L &= \frac{4\pi^2\alpha}{K}\left[\frac{F_2}{\nu}(1+\frac{1}{\gamma^2}) - \frac{F_1}{M}\right], \\
\sigma'_{LT} &= -\frac{4\pi^2\alpha}{MK}\gamma(g_1+g_2), \\
\sigma'_{TT} &= -\frac{4\pi^2\alpha}{MK}(g_1-\gamma^2 g_2),
\end{aligned} \tag{1.18}$$

where $\gamma^2 = Q^2/\nu^2$.

We have discussed Compton scattering amplitudes and virtual photon cross sections. They will be used to derive the spin sum rules in future sections. In the following section, we will discuss an effective theory not relying on the α_s perturbative expansions. It can thus be used in the very low Q^2 domain. Testing such technique is the main goal of our experiment.

1.6 Chiral Perturbation Theory

At low Q^2, the strong coupling constant α_s becomes large so that quarks and gluons arrange themselves in the strongly bound clusters that form hadrons, and perturbation theory expanding in the fundamental coupling α_s is not applicable directly to QCD. In order to describe hadrons at low energy, alternative model-independent approaches are needed. One such approach is the effective theory known as Chiral Perturbation Theory (χPT). χPT is an effective field theory[8] of quantum chromodynamics (QCD) at low energies. That uses a small expansion parameter differing from α_s. This theory assumes that the quark's masses, the pion's mass or momenta of incoming and outgoing particles are negligible compared to the nucleon's mass. The ratio of these quantities to the nucleon mass provides the small expansion parameters.

To understand how χPT works, we first introduce QCD, a local non-Abelian[9]

[8]This particular effective theory treats hadronic fields as the relevant degrees of freedom, instead of the fundamental partonic fields. In addition, the relevant symmetries of QCD are also built in the χPT.

[9]In a non-Abelian gauge theory, field operators do not commute with each other. One consequence

gauge theory that describes the strong interaction. The complete QCD Lagrangian [16] comprises quark and gluon fields which carry *color* charges[10] and interact with coupling strength $g = \sqrt{4\pi\alpha_s}$:

$$\mathcal{L}_{QCD} = -\frac{1}{4g^2} G^{\alpha}_{\mu\nu} G^{\mu\nu}_{\alpha} + \bar{q} i\gamma^{\mu} D_{\mu} q - \bar{q}\mathcal{M}q, \tag{1.19}$$

where $G^{\alpha}_{\mu\nu}$ is the gluon field strength with α the color index and μ, ν the Lorentz indices, q is the quark spinor, D_{μ} is the gauge covariant derivative, γ^{μ} are Dirac matrices connecting the spinor representation to the vector representation of the Lorentz group, and $\mathcal{M}$ is the diagonal quark mass matrix. The values of current u, d, s quark masses ($m_u \simeq 2$ MeV, $m_d \simeq 4$ MeV and $m_s \simeq 93$ MeV) [17] are small compared to the typical light hadronic masses (the proton mass is 938 MeV). The left and right-handed quark wavefunctions can be written as:

$$\begin{aligned} q_L &= \frac{1}{2}(1 - \gamma_5) q, \\ q_R &= \frac{1}{2}(1 + \gamma_5) q. \end{aligned} \tag{1.20}$$

If $\mathcal{M} = 0$, q_L and q_R are not coupled and we thus have two independent particles with left and right helicity[11]. This is the Chiral symmetry. If one sets $m_{u,d,s} \approx 0$, the Lagrangian becomes [18]:

$$\mathcal{L}^0_{QCD} = -\frac{1}{4g^2} G^{\alpha}_{\mu\nu} G^{\mu\nu}_{\alpha} + \sum_{l=u,d,s} \left(\bar{q}_{R,l} i\gamma^{\mu} D_{\mu} q_{R,l} - \bar{q}_{L,l} i\gamma^{\mu} D_{\mu} q_{L,l} \right), \tag{1.21}$$

which means the left and right handed quarks do not interact with each other. The invariance is referred to as the $SU(3)_L \times SU(3)_R$ chiral symmetry of massless QCD. As for all symmetries, a conserved quantity exists, which is the axial current in the case

is that gluons carry color charges and can couple to themselves. In contrast, in QED, photons do not couple directly to each other.

[10] The color quantum number is introduced as an extra degree of freedom in the quark model of hadrons and solved a factor of 3 increases in cross section of the process $e^+e^- \to$ hadron among other experimental evidence of the color charge. In QCD, the color charge of a quark has three possible values: red, green or blue.

[11] For a massless particle, chirality is identical to helicity.

of chiral symmetry. In the real world, however, chiral $SU(3)_L \times SU(3)_R$ symmetry is explicitly broken by finite quark masses $m_{u,d,s}$ and more importantly by spontaneous symmetry breaking. Therefore, the axial vector current[12] is not conserved. This introduces an spontaneous breaking of chiral symmetry in $\mathcal{L}_{QCD}$:

$$\mathcal{L}_{QCD} = \mathcal{L}^0_{QCD} + \mathcal{L}^{sb}_{QCD}, \tag{1.22}$$

Goldstone's theorem states that a spontaneously broken continuous symmetry implies massless spinless particles: the Goldstone bosons. The eight lightest hadrons are $\pi^{\pm}, \pi^0, K^{\pm}, K^0, \bar{K}^0, \eta$. Because the nonzero masses of the light quarks break chiral symmetry explicitly the Goldstone bosons are not exactly massless. However, the explicit breaking can be considered to be small and treated perturbatively. In the limit of vanishing quark masses, $m_u, m_d, m_s \to 0$, the Goldstone boson masses approach zero, $m_\pi, m_K, m_\eta \to 0$, while all other hadrons remain massive in the chiral limit.

The approximate χPT Lagrangian can be obtained by keeping all terms that are consistent with the symmetries of QCD. These terms will be chosen or discarded depending on power counting scheme (p-expansion, the relation between loop diagrams and the momentum expansion) in χPT. In addition, each term will be multiplied by a coupling constant (also called low-energy constants) which represent the relative strength of the interaction at the vertex. When the quark masses are restored, the perturbative theory is valid as long as quark masses or momenta of incoming and outgoing particles are small enough.

The framework of χPT can be extended to the interaction of baryons at low energies, the effective Lagrangian includes the baryon fields. In case of two flavors (u and d), the discussion is narrowed to the nucleons and pions. However, for baryon calculations the power counting rule becomes complicated because the nucleon mass is finite in the chiral limit and is comparable to the chiral symmetry breaking scale.

[12]The requirement of Lorentz invariance of the matrix elements restricts the form of interaction vertex. An axial vector current is one of the five possible combinations of two spinors and the gamma matrices. The axial vector current has the form $\bar{\psi}\gamma^\mu\gamma^5\psi$.

The one-to-one mapping between loop diagrams and chiral orders in the mesonic sectors does not hold anymore in the baryonic case, and an infinite number of loop diagrams contribute to a certain chiral order [19]. To overcome this, the Heavy Baryon χPT (HBχPT) approach was introduced, HBχPT takes advantage of the fact that baryons are heavy, which means that the momenta involved are small, and the theory is expanded in inverse powers of baryon masses [20].

Another approach is Infrared Regularization (IR) [21] which separates the one-loop integral into an infrared part and regular part. The first obeys the power counting rule, the second can be expanded in a power series and be absorbed into low energy constants of the effective Lagrangian.

We have described χPT, the low energy approach to QCD that E97-110 aims to test. In the following, we will discuss the observables measured for such test, namely the generalized GDH sum rule. First we need to introduce the original GDH sum rule.

1.7 The GDH Sum Rule for Real Photons ($Q^2 = 0$)

The Gerasimov-Drell-Hearn (GDH) sum rule [23] relates the absorption cross section of circularly polarized real photons to the anomalous magnetic moment of the target, in our case the nucleon or the ^{3}He nucleus:

$$I(Q^2 = 0) = \int_{thr}^{\infty} (\sigma_{1/2} - \sigma_{3/2}) \frac{d\nu}{\nu} = -2\pi^2 \alpha \frac{\kappa^2}{M^2}, \tag{1.23}$$

where $\sigma_{1/2}$ and $\sigma_{3/2}$ are the photoabsorption cross sections and the subscripts are the total nucleon-photon helicity, ν is the photon energy, κ is the anomalous magnetic moment of the target and M is its mass, α is the fine structure constant ($\approx 1/137$). The integral goes from the photoproduction threshold[13] to infinity. While the left hand side of Eq. 1.23 describes a dynamical property of the target, the right hand side involves ground state properties of the target that are well-measured. The non-

[13] This refers to the single pion production threshold for a nucleon target $\nu_{thr} \approx 150$ MeV, and two body break up for a nuclear target ($\nu_{thr} = 2.2$ and 5.5 MeV for the deuteron and ^{3}He respectively).

zero value of the anomalous magnetic moment requires the existence of an excitation spectrum of the target. For example, the nonzero κ value of the proton implies that it has a substructure. This sum rule can be used for all type of targets, such as proton, neutron, electron[14], etc.

The GDH sum was derived using the dispersion relation and a low energy theorem. It uses the following steps:

1. The Unitarity of scattering matrix relates the absorption cross section to the imaginary part of forward scattering amplitude $\Im f(\nu) \sim \sigma_{T,TT}$. This is the optical theorem [24].

2. Causality implies the analyticity of $f(\nu)$, which allows one to write a dispersion relation. This dispersion relation relates the real part of the scattering amplitude to the integral of $\sigma_{T,TT}$, $\Re f(\nu) \sim \int_{\nu_0}^{\infty} \sigma_{T,TT}(\nu') \frac{\nu}{\nu'} d\nu'$.

3. The Taylor expansion of the real part of scattering amplitude $(\Re f(\nu), \Re g(\nu))$ in term of ν. Combining this expansion with the Low Energy Theorem (LET) [25], which comes from gauge and Lorentz invariances, leads to the GDH sum rule.

The main assumption ad a weak part in the derivation of GDH sum rule is the non-subtraction hypothesis. It assumes that σ_{TT} decrease fast enough toward zero as $\nu \to \infty$.

We have discussed the sum rule for real photons. Next we will discuss the generalized sum rule with exchange of a virtual photon instead of the absorption of a real photon.

1.8 Generalized GDH Sum Rule ($Q^2 > 0$)

The first extension of the GDH sum was proposed by Anselmino *et al.* [26]. A straightforward way to generalize the sum is replacing photoproduction cross sections

[14] For point-like particle, anomalous magnetic moment $\kappa = 0$, hence there is no excited spectrum.

with the electroproduction ones of a virtual photon as discussed in Sec. 1.5. This can be done by substituing:

$$\sigma_{1/2}(\nu), \sigma_{3/2}(\nu) \rightarrow \sigma_{1/2}(\nu, Q^2), \sigma_{3/2}(\nu, Q^2). \tag{1.24}$$

With this approach, one can generalize the sum (the integral) but not the sum rule. In addition, virtual photon cross sections are not uniquely defined quantities since the definition of virtual photon flux K is conventional. The first approach to generalize the entire sum rule was proposed by X. Ji and J. Osborne [27] using the virtual photon Compton amplitude. While the Compton amplitude cannot be measured directly, it can be accessed indirectly by using a dispersion relation. This dispersion relation relates the Compton amplitude to the spin structure functions which have been measured in SLAC, CERN, DESY and JLab. In addition, theories like χPT or Lattice QCD can calculate the virtual photon nucleon Compton scattering. Particularly, at small Q^2, one can calculate Compton amplitudes in χPT. At large Q^2, one uses measurements and evolve them (using OPE). For $\int g_1^{p-n} dx_1$, one uses the Bjorken sum rule. But this concerned the moment directly, not the Compton amplitude.

The forward Compton amplitude for real photon in Eq. 1.12 can be modified to include the longitudinal polarization vector $\hat{q}$ to obtain the virtual Compton scattering as follow:

$$\begin{aligned} T(\nu, Q^2, \theta = 0) = \vec{\epsilon}^{\,\prime *} \cdot \vec{\epsilon}\, f_T(\nu, Q^2) + i\vec{\sigma} \cdot (\vec{\epsilon}^{\,\prime *} \times \vec{\epsilon})\, g_{TT}(\nu, Q^2) \\ + f_L(\nu, Q^2) + i(\vec{\epsilon}^{\,\prime *} - \vec{\epsilon}) \cdot (\vec{\sigma} \times \hat{q})\, g_{LT}(\nu, Q^2), \end{aligned} \tag{1.25}$$

where g_{TT} and g_{LT} are the spin flip amplitudes. These amplitudes can be rewritten in term of spin-dependent Compton amplitudes $S_1(\nu, Q^2)$ and $S_2(\nu, Q^2)$:

$$\begin{aligned} S_1(\nu, Q^2) &= \frac{\nu M}{\nu^2 + Q^2} \Big[g_{TT}(\nu, Q^2) + \frac{Q}{\nu} g_{LT}(\nu, Q^2) \Big], \\ S_2(\nu, Q^2) &= -\frac{M^2}{\nu^2 + Q^2} \Big[g_{TT}(\nu, Q^2) - \frac{Q}{\nu} g_{LT}(\nu, Q^2) \Big]. \end{aligned} \tag{1.26}$$

A dispersion relation gives [27]:

$$\begin{aligned} S_1(\nu, Q^2) &= 4 \int_{\nu_{thr}}^{\infty} \frac{G_1(\nu', Q^2)\nu'}{\nu'^2 - \nu^2} d\nu', \\ S_2(\nu, Q^2) &= 4 \int_{\nu_{thr}}^{\infty} \frac{G_2(\nu', Q^2)\nu'}{\nu'^2 - \nu^2} d\nu', \end{aligned} \tag{1.27}$$

where G_1 and G_2 are related to g_1 and g_2 as:

$$\begin{aligned} G_1(\nu, Q^2) &\equiv \frac{M g_1(\nu, Q^2)}{\nu}, \\ G_2(\nu, Q^2) &\equiv \frac{M g_2(\nu, Q^2)}{\nu^2}, \end{aligned} \tag{1.28}$$

and where $\nu_{thr} > Q^2/2M$ is the elastic scattering condition, ν on the left hand side is an energy taken to the $\nu \to 0$ limit in order to apply the LET. The integral over the photon energy ν' on the right hand side covers all kinematic ranges of electroproduction ($\nu_{el} < \nu' < \infty$). In the $\nu \to 0$ limit Eq. 1.27 becomes:

$$\begin{aligned} S_1(0, Q^2) &= 4 \int_{\nu_{el}}^{\infty} G_1(\nu, Q^2) \frac{d\nu}{\nu}, \\ &= \frac{8}{Q^2} \int_0^{1^-} g_1(x, Q^2) dx \equiv \frac{8}{Q^2} \Gamma_1(Q^2). \end{aligned} \tag{1.29}$$

This represents a Q^2-dependent sum rule provided that one knows how to compute the Compton amplitude $S_1(0, Q^2)$. In regions where g_2 contribution is negligible (such as the DIS region or at the real photon point), combining Eq. 1.23 and Eq. 1.29 gives the GDH integral:

$$I(Q^2) \equiv \int_{\nu_{el}}^{\infty} \frac{\sigma_{1/2}(\nu, Q^2) - \sigma_{3/2}(\nu, Q^2)}{\nu} d\nu = \frac{2M^2}{Q^2} \Gamma_1(Q^2). \tag{1.30}$$

Or in terms of Compton amplitude:

$$S_1(0, Q^2) = \frac{4}{M^2} I(0, Q^2). \tag{1.31}$$

Another form of Eq. 1.30 is written in terms of spin structure functions as follows:

$$I_{TT}(Q^2) = \frac{2M^2}{Q^2}\int_0^1 \left[g_1(x,Q^2) - \frac{4M^2}{Q^2}x^2 g_2(x,Q^2)\right]dx. \tag{1.32}$$

The generalized sum rule recovers the real photon GDH sum when one examines the limit as $Q^2 \to 0$. Since the original sum rule does not include the elastic contribution, we consider only the inelastic contribution:

$$\bar{S}_1(0,Q^2) \equiv S_1(0,Q^2) - S_1^{el}(0,Q^2). \tag{1.33}$$

Expanding it around $Q^2 = 0$ yields:

$$\bar{S}_1(0,Q^2) = -\frac{\kappa^2}{M^2} + \bar{S}_1{}'(0,0)Q^2 + \bar{S}_1{}''(0,0)Q^4 + \ldots. \tag{1.34}$$

where $\bar{S}_1{}'$ and $\bar{S}_1{}''$ are the first order and second order Q^2-derivatives. Applying Eq. 1.31 for the real photon recovers the GDH sum rule, Eq. 1.23.

The generalized GDH sum rule can be used to test theories because a disagreement between the theoretical predictions for S_1 and the measured GDH sum reveals the quality of the approximations involved.

1.8.1 The Sum Rule in The Chiral Domain (Small Q^2)

In the low Q^2 region, one can use χPT to expand $\bar{S}_1{}'(0,0)$ as a power series. Previously, Ji and Osborne's calculation using Heavy Baryon Chiral Perturbation Theory (HBχPT) [27] reveals that the leading order contribution vanishes and that at leading order, $\bar{S}_1(0,Q^2)$ is independent of Q^2. However, the next leading order contribution is strongly Q^2 dependent. There are new calculations beyond HBχPT [36, 37].

1.8.2 The Sum Rule at Larger Q^2

At $Q^2 \to \infty$, another spin sum rule exists: the Bjorken sum rule [28]. This sum rule was originally derived from current algebra. It was rederived in the QCD

framework and extended to finite (but still large) Q^2. The prediction of the Q^2 dependence of the Bjorken sum rule constitutes an important test of pQCD. The Bjorken sum rule states:

$$\Gamma_1^p - \Gamma_1^n = \int_0^1 \Big[g_1^p(x) - g_1^n(x)\Big] dx = \frac{g_A}{6}, \tag{1.35}$$

where superscripts p, n stand for proton and neutron and g_A is the isovector axial charge of the nucleon, measured in neutron β-decay. In the $Q^2 \to \infty$ limit where g_1 is interpretable in the parton model, the first moments Γ_1 of proton and neutron can be written in terms of the light u, d and s quark's parton distribution functions (PDF) as:

$$\begin{aligned} \Gamma_1^p &\equiv \int_0^1 g_1^p(x)dx = \frac{1}{2}(\frac{4}{9}\Delta u + \frac{1}{9}\Delta d + \frac{1}{9}\Delta s), \\ \Gamma_1^n &\equiv \int_0^1 g_1^n(x)dx = \frac{1}{2}(\frac{1}{9}\Delta u + \frac{4}{9}\Delta d + \frac{1}{9}\Delta s). \end{aligned} \tag{1.36}$$

The difference yields a parton model interpretation of the Bjorken sum rule:

$$\Gamma_1^p - \Gamma_1^n = \frac{1}{6}(\Delta u - \Delta d). \tag{1.37}$$

The internal spin structure of the nucleon is probed using weak decay and scattering of polarized leptons from polarized targets: Assuming $SU(3)_{flavor}$various quark flavor contributions to the nucleon spin can be obtained from these processes, each provides a certain linear combination of $\Delta u, \Delta d$ and Δs [29]. One combination of the quark spin content is obtained by the neutron β-decay:

$$g_A = g_3 = \Delta u - \Delta d. \tag{1.38}$$

Combining Eq. 1.37 and Eq. 1.38 yields the Bjorken sum rule.

At large but finite Q^2, QCD radiative corrections and higher twists have to be taken into account. Using OPE, we can separate the perturbative (QCD radiative

corrections) from the nonperturbative (higher twists) parts. The Bjorken sum rule generalized to finite Q^2 reads:

$$\Gamma_1^p - \Gamma_1^n = \frac{1}{6}(\Delta u - \Delta d) = \frac{g_A}{6}\left(1 - \frac{\alpha_s(Q^2)}{\pi} + \dots\right) + HT(Q^2), \tag{1.39}$$

where the first term on the right hand side is the same as Eq. 1.35 except for the QCD radiative correction in power series of $\alpha_s(Q^2)$, which can be calculated using perturbative QCD (pQCD). The second term $HT(Q^2)$ comes from higher twist effects and is non-perturbative.

1.9 Current Data for GDH Sum at Low Q^2

In this section, we discuss current experimental data and theoretical predictions. Particularly, the discussion will be restricted to measurements of the neutron spin structure from a polarized ^{3}He target.

Results for the generalized GDH sum on the neutron, I_{TT}, are shown in Fig. 1-3, where the blue triangles are results from JLab experiment E94-010 [33]. The integration using only this experiment data are shown in open blue circles. The error bars on the data points are statistical and the systematic uncertainties are given by the blue band on the horizontal axis. The blue data show a smooth transition from partonic degrees of freedom (high Q^2) to hadronic degrees of freedom (low Q^2). The results from E94-010 emphasize the importance of treating properly the $\Delta(1232)$ resonance in the χPT calculations. However, the E94-010 data did not reach low enough Q^2 so that they cover the chiral domain where χPT calculations can be accurately tested. The red triangles are results from the experiment discussed here (second period only) [34]. The integration using only this experiment data, and that with an estimate of the unmeasured high W part are represented by the open and solid triangle, respectively. The error bars represent the statistical uncertainties. Uncorrelated and correlated systematic uncertainties are shown by the upper (red) and lower (magenta) bands, respectively. The bands around -50 μb indicate the model uncertainties (red: neutron extraction from ^{3}He; magenta: low-x extrapolation). Our

second period data and E94-010 are consistent over their overlap region.

As Q^2 decreases, our results agree with the χPT calculation from Bernard *et al.* [36]. The calculation from Lensky *et al.* [37] disagrees with the data. The first calculation [36] includes $\Delta(1232)$ explicitly in the third order in the small expansion (It uses dimensional regularization instead of infrared regularization). The latter calculation [37] uses relativistic BχPT that include next-to-leading order term correction including the $\Delta(1232)$.

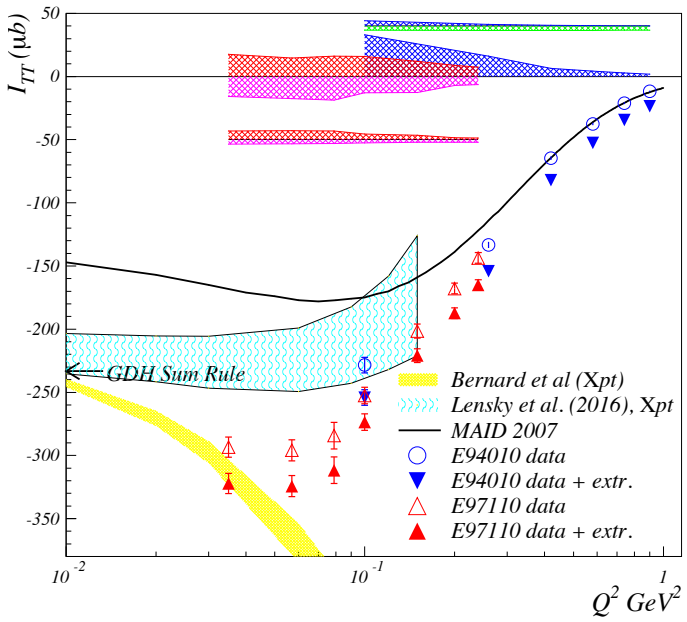

Figure 1-3: Results and expectations for the neutron generalized GDH sum $I_{TT}(Q^2)$. Blue triangles are the JLab experiment E94-010 results [33]. Red triangles are the second period results of JLab experiment E97-110 [34]. The error bar on each data point is statistical, with systematic uncertainties given by bands along the horizontal axis. The solid black line is the MAID model calculation. The two latest χPT predictions at low Q^2 are shown: Bernard *et al.* [36] (yellow band) and Lensky *et al.* [37] (cyan band). The arrow at $Q^2 = 0$ is the GDH sum for the real photon.

1.10 Summary

Theoretical tools for computing the generalized GDH sum rule have been presented in this chapter [15]. At low, i.e below a few tenths of GeV^2, one can use χPT to calculate the Compton amplitude. However, several theoretical predictions in this region disagree with each others. Hence, measurements of the neutron spin structure at low Q^2 will provide a benchmark test of χPT and help guiding their theoretical progress. The discrepancies between data and calculations can be due to some approximation in χPT calculations themselves.

[15] Lattice QCD has started to compute Compton amplitudes such as the ones included in the GDH sum rule. So lattice QCD will give us a prediction too, and it will be based on fundamental QCD principles.

Chapter 2

The Experiment and Its Instruments

Experiment E97-110 was carried out in experimental Hall A at the Thomas Jefferson National Accelerator Facility (TJNAF) in April-May (first period) and July-August (second period) of 2003. The experiment focused on a precise measurement of the moments of the neutron spin structure functions at low Q^2 ($0.02 < Q^2 < 0.3$ GeV^2) using a polarized ^{3}He target as an effective polarized neutron target. The goal of the experiment is to make a bench-mark test of Chiral Perturbation Theory calculations. A secondary goal is to check the Gerasimov-Drell-Hearn (GDH) sum rule by extrapolating the integral to the real photon point.

The kinematic coverage of the experiment is shown in Fig. 2-1. Longitudinal polarized electrons with nine incident energies between 1.1 and 4.4 GeV were scattered from a high-pressure polarized ^{3}He target. The target was polarized in both longitudinal and transverse directions, which allows us to extract both spin structure functions.

Data were taken in two experimental run periods. The first period covered the lowest Q^2 points but with a defective equipment which complicates the data analysis. The second period covered higher Q^2 points, with a properly working equipment. In this thesis, the first period data are discussed. The second period data were analyzed by V. Sulkosky [6].

In this chapter, information on the electron beam, the Hall A beamline, Hall A spectrometers, and target collimator will be presented. I will also give a summary

about the polarized ^{3}He target, which details will be discussed in Chapter 6.

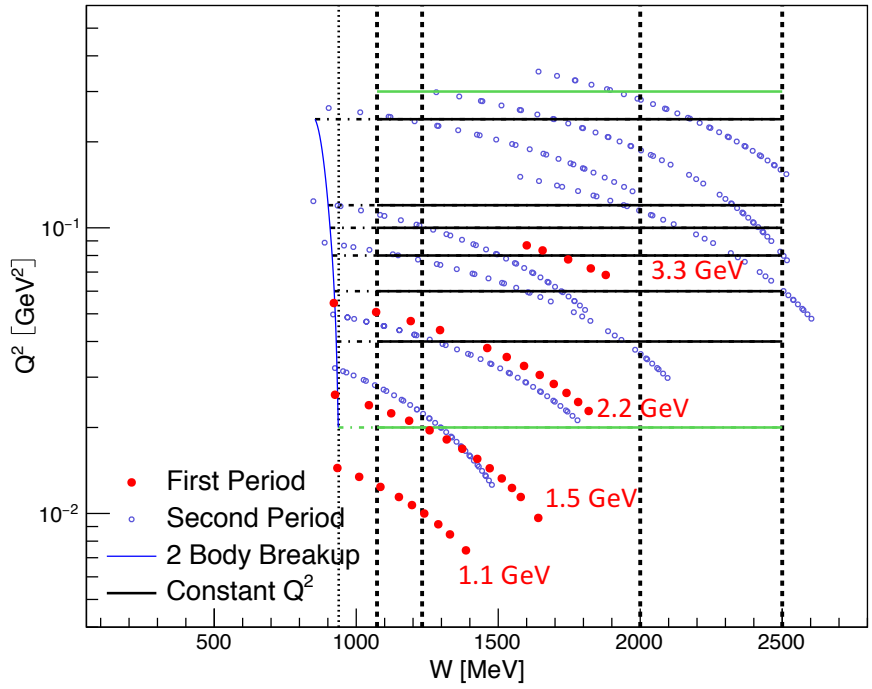

Figure 2-1: Kinematic coverage of experiment E97-110. The horizontal axis is the invariant mass W. The vertical axis is the Q^2. The solid horizontal black lines are the constant Q^2 used for the data analysis of the second period data. The value of $I(Q^2)$ is obtained by integration of the cross section difference over W at these constant Q^2 values. Red points are first period data, taken at four beam energies: 1.1, 1.5, 2.2, and 3.3 GeV and at 6°.

2.1 The Electron Accelerator

The layout of the electron accelerator is shown in Fig. 2-2. Electrons of 45 MeV energy are produced by the polarized source and then are inserted and accelerated by two linacs. They are sent to three experimental halls A, B, C. Until 2012, the highest beam energy was 6 GeV. After the accelerator upgrade in 2014-15, the highest beam energy became 12 GeV for Halls A, B, C and a fourth Hall (Hall D) was added. The maximum current that can be delivered, summed over all four halls, is 200 μA.

The polarized source is a gallium arsenide (GaAs) which was first used at SLAC [38]. Electrons are extracted by shining the laser light on a GaAs photocathode. Electrons are excited from the valence band ($P_{3/2}, m = 3/2$ state) to the conduction band ($S_{1/2}, m = 1/2$ state). A "strain" GaAs cathode is created by growing a thin layer of GaAs on a GaAsP substrate. The strain induces a gap in sublevels of $P_{3/2}$ electrons in the valence band. The gap causes the laser light to be absorbable only by electrons in the $P_{3/2}$, $m = 3/2$ state, and not by other states. Hence, electrons are excited only to the $S_{1/2}, m = 1/2$ state. From there electrons diffuse to the surface and escape into the surrounding vacuum. Ideally, this means the electrons produced are 100% polarized but in reality, polarization between 80-90% are obtained. The spin of emitted electrons can be flipped by using a Pockels cell that controls the polarization of the laser. The Pockels cell is a crystal that acts as a quarter wave plate when a high voltage is applied on it. By flipping the polarity of the high voltage, we can invert the circular polarization of the laser. During E97-110, the beam helicity was flipped provide the rate at which it is flipped with the helicity sequence states following a quartet pattern, either $+--+$ or $-++-$, and the sequence of the quartets was pseudo-random. This helps to minimize the low frequency systematic uncertainty.

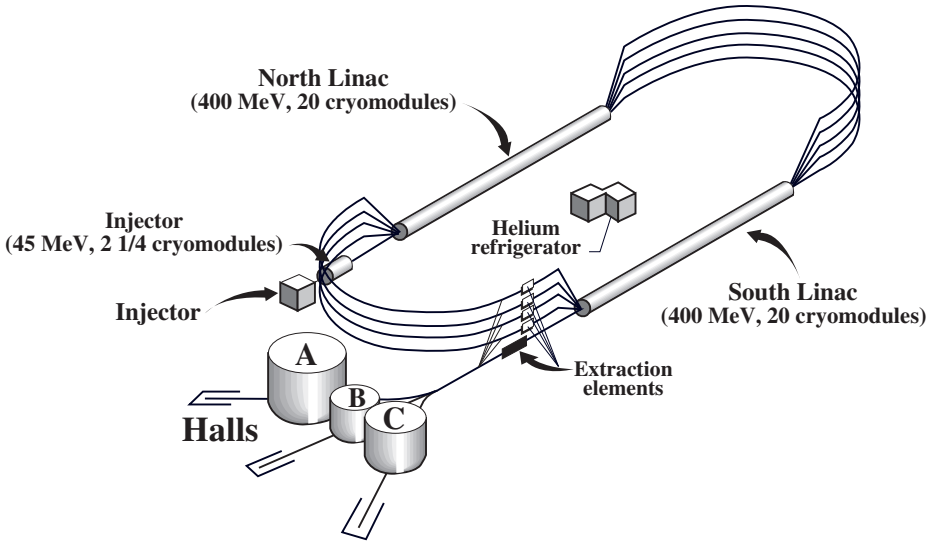

Figure 2-2: Layout of CEBAF (Continuous Electron Beam Accelerator Facility) in 6 GeV era [39]. After passing 5 times through each linac, electron energy can reach 6 GeV. Electron beam can be sent simultaneously to each of the experimental halls.

2.2 Hall A Layout

Hall A is the largest experimental hall among all of JLab's halls. The layout of Hall A is shown in Fig. 2-3. The key elements for E97-110 include the beam line, the polarized ^{3}He target (see Section 2.7 and Section 6), a septum magnet, two High Resolution Spectrometers (Left and Right HRS)[1] and their detector packages, which will be discussed in following sections.

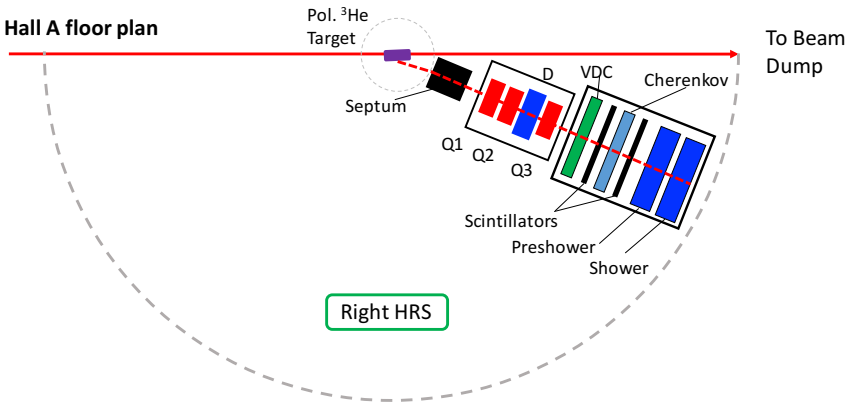

Figure 2-3: Hall A layout. Since only a single septum magnet was available, only right HRS (RHRS) was used for production data taking during E97-110 while the left HRS was used to monitored the beam current using a carbon foil target, as well as charge asymmetry.

2.3 Hall A Beamline

2.3.1 Beam Current Measurement

The beam current is measured by the beam current monitor (BCM), which consists of two cylindrical waveguides (cavities). When the beam passes through the cavities, the voltage output from the cavity is proportional to the beam current. In addition,

[1]The experiment E97-110 only used the right HRS for physics data taking because of the availability of only one septum magnet. The left HRS was used to monitor the beam current using a carbon foil target, as well as charge asymmetry.

a Unser (a parametric current transformer) provides an absolute calibration of the cavities. The Unser, being unstable over a time scale of several minutes, cannot be used to monitor the beam current continuously.

The voltage output from a cavity is split into two parts: sampled and integrated data, as shown in Fig. 2-4:

- For sampled data: The output from an amplifier is sent to a high-precision digital AC voltmeter. Once every second, the RMS of the input signal provides a digital output. This output is proportional to the beam charge accumulated during that time. Then it is sent to a computer through GPIB.

- For integrated data: The output from an amplifier goes through a RMS-to-DC converter. Then it is sent to a Voltage-to-Frequency (VTOF) converter, whose output frequency is proportional to the DC input voltage. With the VTOF, no signal is lost on the way as it is transported to the VME scalers.

The upstream and downstream BCMs are each connected to three amplifiers with $\times 1$ (no amplification), $\times 3$ and $\times 10$ gains. For experiment E97-110, the $\times 3$ gain signals were used for beam currents above 5 μA and the $\times 10$ gain signals for currents below 5 μA.

The beam charge is extracted from the scaler readings by:

$$Q_{BCM\times G,Hel}(\mu C) = \frac{\frac{N_{BCM\times G,Hel}(count)}{t_{Hel}} - offset_{\times G,Hel}}{calibration\ constant_{\times G}(count/\mu A)} t_{Hel} \tag{2.1}$$

where *count* is from upstream or downstream scaler reading with different gains $\times 1$, $\times 3$, $\times 10$. The helicity is denoted Hel and can be plus, minus or ungated. The offset $offset_{\times G,Hel}$ for each gain G and each helicity was obtained from cosmic runs (no beam). t_{Hel} is the run time length for each run with helicity +, - or ungated. $calibration\ constant_{\times G}$ is the constant used to convert from upstream or downstream BCM reading to current values with different gains. These calibration constants are given in Table. 2.1.

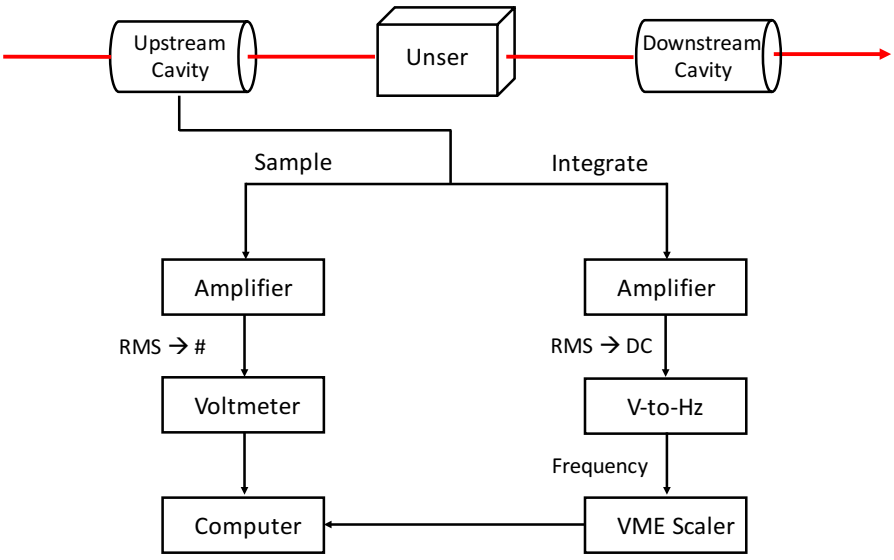

Figure 2-4: Schematic of beam current monitors.

Amplification (×G)	Upstream Cavity	Downstream Cavity
×1	1338.4	1335.5
×3	4100.7	4140.9
×10	12467.5	13015.1

Table 2.1: BCM calibration constants for E97-110 in unit of counts/μA [40].

2.3.2 Beam Position Measurement and Raster

The transverse position of the beam on target and the angle with respect to the nominal beam direction are measured by two Beam Position Monitors (BPMs) located 7.524 m and 1.286 m upstream of the target center. Each BPM has 4-wire antenna tuned to the fundamental frequency of the beam. When the beam passes through the BPM system, a signal is induced that is proportional to the distance from the beam. The absolute position of the BPMs can be calibrated by two superharps (wire scanners) which are located adjacent to each of the BPMs. The BPMs have a resolution of 20 μm at 10 μA [6].

The typical beam at JLab has a width of $\approx 200\mu$m. In order to avoid overheating

the thin glass end windows of the polarized ^{3}He target, the electron beam is rastered to a larger cross-sectional size. The raster hardware is located 23 m upstream from the target. For experimental E97-110, instead of the usual sine modulation, a new "triangular" raster was used, which copied the Hall C design [41]. The raster uniformly distributed the beam inside a square area with the dipole magnetic field varying in a triangular waveform over time. During the experiment, different raster sizes were used, and the most often used raster size was a 4 mm $\times$ 4 mm square.

2.3.3 Beam Energy Measurement

An accurate knowledge of the beam energy is very important for the analysis because it determines all kinematic variables. Currently, there are three independent methods for measuring the beam energy [39]: the eP measurement, based on elastic electron proton scattering; the Arc measurement, based on the beam deflection in a known magnetic field; and the so-called Tiefenbach energy which relies on a parameterization of the beam transport in CEBAF. We describe the just two method in details since they pertain to Hall A.

The first method, eP measurement, measures the electron scattering angle θ_e and the proton recoil angle θ_p in elastic reaction ^{1}H(e,e'P). The beam energy is given by:

$$E_{beam} = M_p \frac{\cos\theta_e + \sin\theta_e / \tan\theta_p - 1}{1 - \cos\theta_e}, \tag{2.2}$$

with M_p the proton mass. The arrangement of the measuring apparatus is shown in Fig. 2-5.

The electron beam hits the target, a thin CH_2 plastic film, then the scattered electron and the recoil proton are measured in coincidence by two sets of detectors. The scintillator provides the trigger and Cherenkov detectors are utilized for electron identification. The scattering angles are determined by Silicon Strip Detectors (SSD). The resulting uncertainty on the beam energy from the eP method is $\leq 2 \times 10^{-4}$ GeV.

The second method, the Arc measurement, determines the beam energy by measuring the deflection angle of the beam in 40 m arc section of the beamline consisting

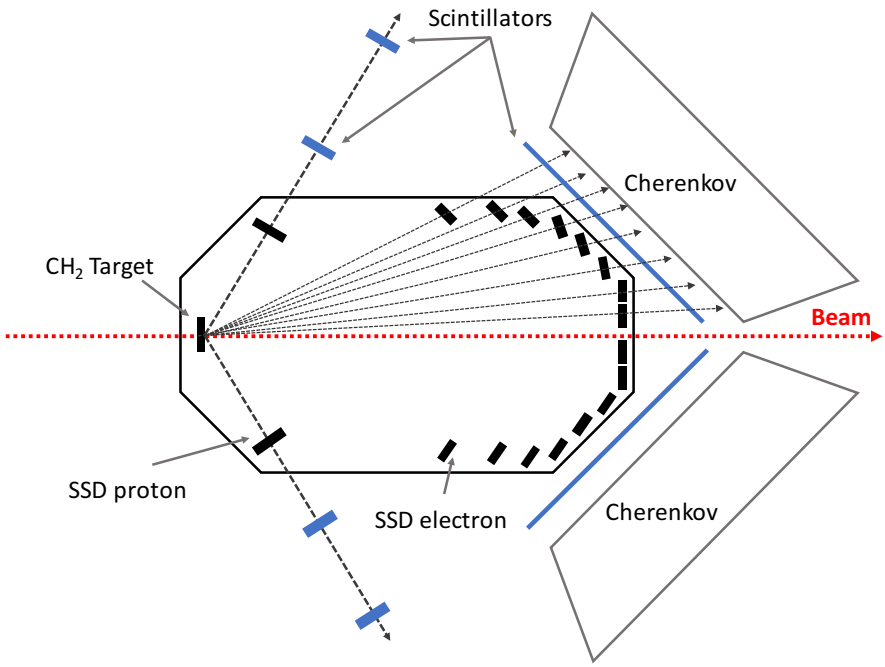

Figure 2-5: Sideview of eP measurement apparatus. Proton detectors include two sets scintillators and a silicon micro-strip detector (SSD proton). The recoil proton is detected at an angle of about 60°, in coincidence with the scattered electron, which is detected at an angle range from 9° to 41°. The electron detector consists of SSD, scintillator planes and Cherenkov counters.

of eight bending magnets. The momentum of the electron beam is related to the field integral along the path of the beam, $\int \vec{B} \cdot \vec{dl}$, and the total bend angle θ as follows:

$$p = k \frac{\int \vec{B} \cdot \vec{dl}}{\theta}, \tag{2.3}$$

where $k = 0.299792$ GeV·rad·T^{-1}m^{-1}/c. The magnetic field integral is measured by using a 9th identical dipole (reference magnet) located outside of the arc and connected in series with the other eight. The actual bending angle is measured by using two pairs of wire scanners, one before and one after the arc. The Arc energy measurement provides an absolute measurement to the 2×10^{-4} GeV level.

The beam energy is also monitored online with Tiefenbach measurement ("Tiefenbach energy"), which relies on the same principle as the Arc energy measurement. Instead of a direct measurement in the arc section, this method extracts the angle

from monitored beam positions with the magnetic transfer function. It is thus non-invasive but at a cost of the precision, which approximately amounts to 5×10^{-4} GeV level[2].

During the experiment, only Tiefenbach measurement was used for the first period [42]. Beam energy for the second period is discussed in V. Sulkosky thesis, Ref. [6].

2.3.4 Electron Beam Polarimetry

Møller Polarimetry

This method uses high energy polarized electrons scattering off a fixed target of polarized electrons of known polarization. By measuring the asymmetry of the scattered electron rates with beam and target polarization parallel or antiparallel, the beam polarization can be obtained. The Møller polarimetries consists of a magnetized ferromagnetic foil that provides the polarized electron target (a magnetized ferromagnetic foil provides the polarized atomic electron target, its polarization is determined by the foil magnetization measurements), and a detector to measure the helicity dependent rate of the scattered electrons.

The polarized Møller scattering cross section is given by [39]:

$$\sigma = \sigma_0 \Big[1 + \sum_{i=X,Y,Z} A_{ii} P_i^t P_i^b \Big], \tag{2.4}$$

where P_i^t, P_i^b are components of the target and the beam polarizations along the i^{th} axis, respectively. The analyzing power A_{ii} depends on the scattering angle in the CM frame, θ_{CM}. σ_0 is the unpolarized Møller cross section:

$$\sigma_0 = \Big[\frac{\alpha(1+\cos\theta_{CM})(3+\cos^2\theta_{CM})}{2m_e \sin^2\theta_{CM}} \Big]^2, \tag{2.5}$$

with m_e is electron mass. If we define the z-axis to be along the beam direction, and the y-axis perpendicular to the scattering plane (OXZ-plane), A_{ii} can be written as:

[2] At its best performance, the uncertainty is 5×10^{-4} GeV, on average the uncertainty is $\approx 10^{-3}$ GeV.

$$A_{ZZ} = -\frac{\sin^2\theta_{CM}(7+\cos^2\theta_{CM})}{(3+\cos^2\theta_{CM})^2},$$
$$A_{XX} = -A_{YY} = -\frac{\sin^4\theta_{CM}}{(3+\cos^2\theta_{CM})^2}. \tag{2.6}$$

The analyzing power is maximum at $\theta_{CM} = 90°$: $|A_{ZZ}| = 7/9$ and $|A_{XX}| = 1/9$.

The Møller polarimetry is conducted at very low beam currents. Asymmetry measurements are performed instead of cross sections. The target is oriented at an angle of $\pm 20°$ with respect to the beam in the horizontal plane. With this orientation, one can access both longitudinal and transverse beam polarizations. However, when the average of the two target directions is taken, the transverse component cancels out.

Compton Polarimetry

The Compton polarimeter is based on Compton scattering. Installed at the entrance of the hall, the Compton polarimeter consists of a magnetic chicane, a photon source, an electromagnetic calorimeter, and an electron detector. The polarization is extracted from the asymmetry measurement of Compton scattering of a circularly polarized photon beam by the electron beam. The beam polarization P_b is extract from:

$$P_b = \frac{A_{exp}}{P_\gamma A_{th}}, \tag{2.7}$$

where A_{exp} is the experimentally measured asymmetry, P_γ is the photon polarization and A_{th} is the Compton analyzing power.

For experiment E97-110, the statistical uncertainty from the Compton polarimeter was (3-5) %, larger than average of other experiments because the beam currents used were low. Hence, the Møller polarimeter was the main source of beam polarimetry for this experiment.

During the first run period, a sizable beam current bleedthrough from Hall C

beam was discovered in the Hall A beamline. This bleedthrough consists of polarized beam, with different polarization than the Hall A beam polarization. It can thus result in a large correction to the beam polarization. The bleedthrough from Hall C in Hall A is dependent on the beam currents from the two halls and the Hall A slit position. A correction to beam polarization is applied for second period [40] which gives beam polarization uncertainty around 3.5%. For first period, the bleedthrough correction is not as good as second period, so it is estimated to be around 4%.

2.4 High Resolution Spectrometers (HRS)

Hall A is equipped with two similar High Resolution Spectrometers, the "Electron" Spectrometer (Right HRS or "Electron-Arm") and the "Hadron" Spectrometer (Left HRS or "Hadron-Arm"). The spectrometers main characteristics are summarized in Table. 2.2. Each spectrometer consists of three quadrupoles and a dipole (QQDQ) superconducting magnets. The first quadrupole (Q1) focuses in the vertical plane and Q2, Q3 focus in the horizontal plane. The dipole spreads the charged particle positions at the detector plane based on their momentum. These magnets also bends up the charge particle with one type of charge, while blocking the neutral particles and bending down the particles of opposite charge. This results in a very clean environment for detectors, and hence with low noise level. The shielding around the detector hut makes this even cleaner. The spectrometer's central momentum P_0 is related to the magnetic field of the dipole by

$$P_0 = \sum_{i=1}^{3} \Gamma_i B_0^i = \Gamma_0 + \Gamma_1 B_0 + \Gamma_2 B_0^2 + \Gamma_3 B_0^3, \tag{2.8}$$

where Γ_i are the spectrometer constants, and B_0 is the dipole magnetic field. To measure Γ_i the absolute electron energy is required. For the HRS, calibrations for Γ_i were obtained using elastic peak position measured in elastic $^{12}C(e,e')$ scattering along with ARC and e-p energy measurements for the beam energy[3][53].

[3]The location of the elastic peak in δp is related to the scattered electron momentum by

$$E' = \Gamma B_0(1+\delta p)$$

Bending angle	45°
Optical length	23.4 m
Momentum range (HRS-L)	$0.3 - 4.0$ GeV/c
Momentum range (HRS-R)	$0.3 - 3.2$ GeV/c
Momentum resolution	1×10^{-4}
Dispersion at the focus (D)	12.4 m
Radial linear magnification (M)	-2.5
Angular Range (HRS-L)	$12.5 - 150°$
Angular Range (HRS-R)	$12.5 - 130°$
Angular acceptance (horizontal)	± 30 mrad
Angular acceptance (vertical)	± 60 mrad
Angular resolution (horizontal)	0.5 mrad
Angular resolution (vertical)	1.0 mrad
Solid angle at $\delta = 0$, $y_0 = 0$	6 msr
Transverse length acceptance	± 5 cm
Transverse position resolution	1 mm

Table 2.2: Nominal Hall A spectrometers characteristics [39].

2.5 HRS Detector Package

The detector package for R-HRS is shown in Fig. 2-6. The following components of the R-HRS were used for this experiment:

- Two planes of thin scintillators to generate triggers.
- A gas Cherenkov detector for particle identification.
- Vertical drift chambers (VDCs) for the determination of position and angular coordinates of the particle tracks.

2.5.1 Scintillators

The HRS-R spectrometer contains two plastic scintillator planes (S_1 and S_2) separated by 2 m to trigger the data acquisition. Timing resolution for each plane is about 0.3 ns. The triggers are sent to the trigger supervisor (TS), which determines if the data acquisition (DAQ) should record the event. When the event rate is high, there can be a high deadtime, which is the fraction of events not recorded by the

where Γ is the spectrometer constant.

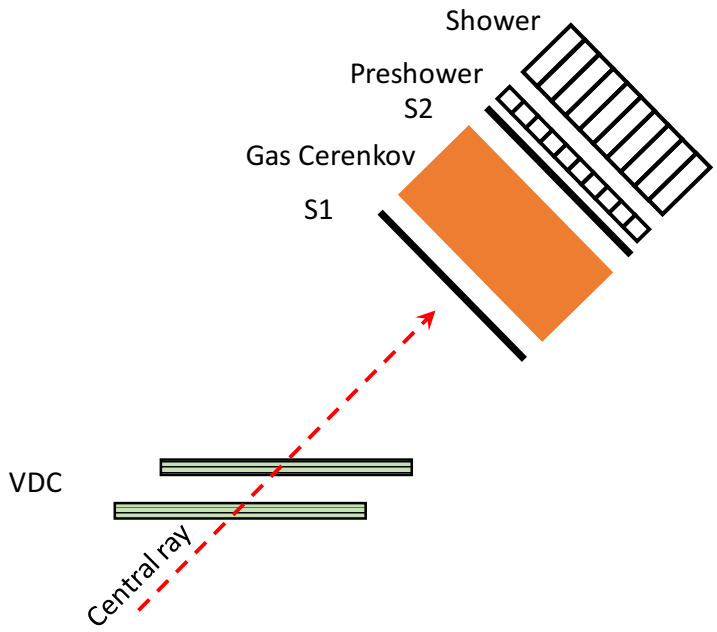

Figure 2-6: Detector package for HRS-R.

DAQ. This deadtime can be decreased by reducing the number of recorded events by a prescale factor (an integer) *ps* at the TS. For every *ps* events, only one is sent to the DAQ system.

2.5.2 Gas Cherenkov Detector

The Gas Cherenkov is mounted between the two scintillator planes and filled with CO_2 at atmospheric pressure with an index of refraction $n = 1.0004$. The Cherenkov detector is used to differentiate between particles with different masses but similar momentum. Particles with velocities exceeding threshold velocity, $\beta_{thresh} = 1/n$, produce Cherenkov radiation. For E97-110, the Cherenkov separated electrons from other negatively charged particles such as pions. For 1 atm CO_2, $n \approx 1.0004$ resulting in a threshold momenta of 17 MeV/c for electrons and 4.8 GeV/c for pions.

2.5.3 Vertical Drift Chambers

The Vertical Drift Chambers (VDCs) provide the particle's tracking information. A VDC package consists of two VDCs, see Fig. 2-7. The lower VDC is located near the ideal focal plane of the HRS. A VDC has two wire planes (U and V planes), which allow detection of both coordinates of a particle track in the plane of the VDC. Position in the two VDCs allows determination of the direction of the track. The resulting position and the angular resolution at the focal plane are approximately 225 μm (FWHM) and 0.5 mrad (FWHM), respectively.

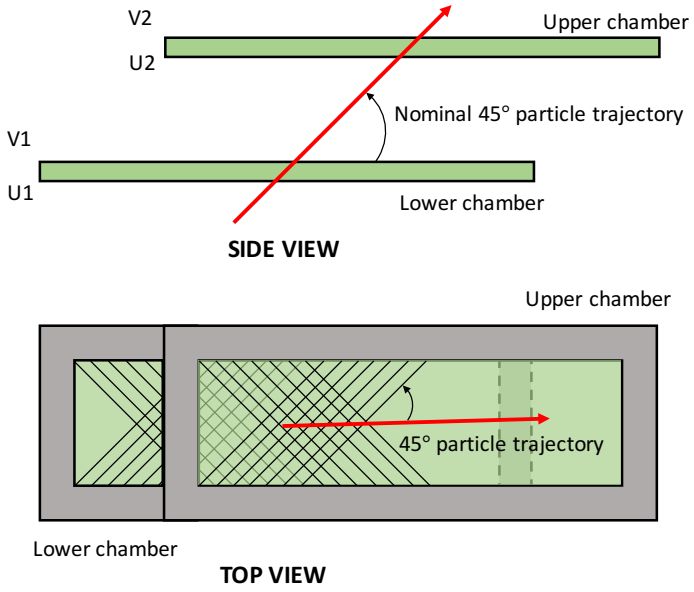

Figure 2-7: Schematic layout of the VDCs. Reproduced from [39].

2.5.4 Electromagnetic Calorimeter

For HRS-R, the shower and preshower provide additional particle identification (PID). These two together are called "total shower" detector. Signals from the total shower is linearly proportional to the energy deposited by the incoming particles. Electrons lose energy by electromagnetic showers and most of theirs energies are

typically deposited in the first layer. When these electrons reach the second layer, they will deposit all the remaining portion of their energies. On the other hand, heavier particles such as pions do not trigger large electromagnetic shower and deposit only part of their energies in the total shower detector. Hence, the total shower can provide a good separation between electrons and pions in an independent way of Cherenkov (otherwise, we would use two Cherenkovs, since they individually have better PID than shower detectors).

2.6 Collimator

For E97-110, a set of collimator was used to block events coming from the target's glass windows. Traditionally, software cuts on the reconstructed target variables were used to remove these events. However, due to the small scattering angle, the transverse position acceptance is about a factor of two smaller and the resolution is a factor of two worse compare to scattering at 12.5°. In addition, the cross section from scattering off the glass creates a sizable contamination to the physics of interest. Without the use of dedicated collimators, described below, a significant contamination from the glass windows would penetrate into the ^{3}He, nitrogen events, which cannot be removed by acceptance cuts.

For the E97-110 experiment, three sets of specially designed target collimators were used:

- BRI6 - for 6° data with the ice cone cell (for first period).
- BRS6 - for 6° data with the standard cell (for second period).
- BRS9 - for 9° data with the standard cell (for second period).

The collimators are located upstream and downstream. The upstream collimator blocks events from the upstream window and the downstream from the downstream window. With the collimators in place the effective target length is approximately cut in half. The layout and position of collimators can be found in V. Sulkosky thesis [6].

In addition to the target collimators, a collimator was placed around the sieve slit to shield the septum entrance from stray events. These stray events come from the beam line on its way toward the beam dump. The collimator around the sieve slit was a 3 cm thick piece of tungsten.

2.7 The Polarized ^{3}He Target

2.7.1 Introduction

^{3}He can be considered effectively as a polarized neutron target. Free neutron has a decay lifetime of 885.7 ± 0.8 s [43], so a free neutron target for scattering experiment is not practical. Two nuclear targets, deuteron and ^{3}He, are typically used as effective polarized neutron targets. A deuteron with spin 1 is primarily a neutron and a proton in an S-state each with spin 1/2 alligned, with a small probability ($P_D \sim 5\%$) to find them in D-state in which case the spins of the neutron or proton can be up or down. The ground state wavefunction of ^{3}He is dominated by the S state ($\sim 90\%$). In this state the proton spins are antiparallel due to the Pauli exclusive principle [44] and the remaining 10% are contributions from S' and D states. Hence, the spin 1/2 of ^{3}He is mostly carried by the neutron spin, making it an efficient effective neutron target.

2.7.2 How to Polarize ^{3}He?

There are two ways to polarize a ^{3}He target. The first one is metastability-exchange optical pumping (MEOP) [45]. In MEOP, a RF (radio frequency) field is applied to bring the ^{3}He atoms from ground state (singlet state) to a metastable state (triplet state). Metastable states of ^{3}He are optically pumped directly and subsequently transfer their polarization to other ground state ^{3}He nuclei during metastability-exchange collisions. The second method is spin exchange optical pumping (SEOP) [46]. In SEOP, optical pumping is used to polarize the unpaired electron of alkali atoms mixed with the ^{3}He. Then polarization is transferred from the alkali atoms to the ^{3}He nuclei via hyperfine interaction. At JLab, we use the latter method

to polarize ^{3}He. The details of the SEOP method will be discussed in the next section.

Optical pumping

Optical pumping is a process in which laser light is used to polarize the electron spins of atoms. The most popular atoms we use are alkali because they possess a single unpaired valence electron. Rubidium and potassium are used for our case, with the unpaired electron in $5S^1$ state. Consider the ground state of the valence electron with orbital angular momentum $L = 0$ and spin $1/2$, the total electron angular momentum is $J = 1/2$. The first excited state is the P state with $L = 1$. With fine structure interaction $\vec{L} \cdot \vec{S}$, the P state splits into the $^2P_{3/2}$[4] and $^2P_{1/2}$ states.

The $^2S_{1/2} \rightarrow^2 P_{1/2}$ and $^2S_{1/2} \rightarrow^2 P_{3/2}$ transitions are referred to as the D1 and D2 lines. Let's define the quantization axis along the direction of the magnetic field. The ground and excited state sublevels start to split into two states with magnetic quantum number $m_s = \pm 1/2$ under an applied magnetic field see Fig. 2-8[5]. With absorption of circularly polarized photons (e.g. σ^+), electrons in the ground state $5S_{1/2}(m_s = -1/2)$ go to excited state $5P_{1/2}(m_s = 1/2)$. In the excited state two effects occur. The first is electron decay back to the two ground states $5S_{1/2}(m_s = \pm 1/2)$ and the second is collisional mixing with $5P_{1/2}(m_s = 1/2)$ in the excited state. The collision of excited electrons with buffer (nitrogen) gas mix the two sublevel of excited states. In other words, the buffer gas randomizes the P states, thus rapidly equalizing the sublevel populations of the excited states. If the photon helicity is in the same direction as the main field, the electrons eventually will go to $m_F = +3$ state. As a result, electrons decay equally back to two ground states sublevel. Eventually, all electrons will accumulate in the $5S_{1/2}(m_s = +1/2)$ state because this state cannot absorb the σ^+ light. As mentioned, to maximize polarization efficiency, a small amount of nitrogen buffer gas is needed. This is because electrons can go from $5P_{1/2}$ to $5S_{1/2}$ with the emission of photons with the same wavelength as the

[4]The standard notation to describe energy levels is $^{2S+1}L_J$.

[5]For optical pumping only, the applied magnetic field is not necessary as long as it is above a certain limit ($\gg$ 2 mG) [47] to prevent fast mixing of two ground states sublevels. For our case, we need a magnetic field in order to keep the field homogeneous. So the noble gas polarization relaxation can be reduced.

laser light, but unpolarized. These unpolarized photons will decrease the pumping efficiency. Nitrogen is a diatomic molecules, it has a variety of energy levels of rotation, translation, and vibration and thus can absorb the energy emitted by the electron decay. For a nitrogen density of ~ 0.1 amg the quenching time is much smaller than decay time, and nearly all electrons can go from excited state to ground state without emitting a photon (quenching).

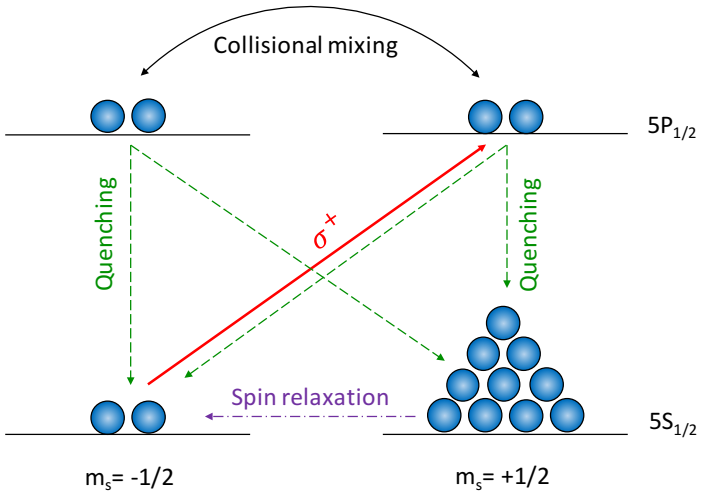

Figure 2-8: Optical pumping of Rb by a right-handed circularly polarized laser. Figure from Ref. [48]

The average alkali polarization is determined by the ratio of the optical pumping rate R and electron spin destruction rate Γ_{SD} [49]:

$$P_{Rb} = \frac{R}{R + \Gamma_{SD}}. \tag{2.9}$$

The optical pumping rate R depends on the laser photon flux per unit frequency and the light absorption cross section. The electron spin destruction rate Γ_{SD} is mostly due to the spin rotation interaction between Rb atoms and other atoms. The

spin-rotation interaction, with a strength of [50]

$$H_{SR} = \gamma \vec{N} \cdot \vec{S}, \tag{2.10}$$

causes spin relaxation by coupling $\vec{S}$ to the rotation angular momentum $\vec{N}$ of the alkali-metal-noble-gas pair, with γ the spin-rotation interaction coefficient.

Spin-exchange

The second step is the spin-exchange through which the polarized alkali atoms transfer their (electron spin) polarization to the ^{3}He nuclei. The spin-exchange process is dominated by binary collisions. Alkali atoms interact with ^{3}He nuclei through both isotropic hyperfine interaction and spin-rotation interaction. The isotropic hyperfine interaction is the one producing spin-exchange and is described by [51]:

$$H_{KS} = \alpha \vec{K} \cdot \vec{S}, \tag{2.11}$$

with α is the coupling constant for Fermi-contact interaction. The hyperfine interaction couples the noble-gas (^{3}He) nuclear spin $\vec{K}$ to the alkali-metal (Rb) electronic spin $\vec{S}$. The probability of spin-exchange, or the spin-exchange cross section, during binary collision (for which the duration of collision is much shorter than the time between collisions) is proportional to α^2, and depends on the overlap of the alkali-metal valence-electron wavefunction with the noble-gas nucleus. The overlap effects between Rb and ^{3}He cause an enhancement of the hyperfine interaction between Rb electrons and ^{3}He nuclei [46]. As a result the interaction is strong enough to cause the polarization of the ^{3}He nuclei.

In conclusion, the spin exchange is due to hyperfine interaction between the Rb electrons and the ^{3}He nuclei. The interaction gives rise to both a transfer of the polarization to ^{3}He and a shift of the Rb Zeeman frequency due to the ^{3}He polarization. The later effect will be used for EPR polarimetry see Section 6.3.

2.7.3 JLab ^{3}He Lab Setup

The target system at JLab includes a laser/optic system, an oven, the ^{3}He cell and three pairs of Helmholtz coils. The cell is held at the center of the target where the pumping chamber of the cell is mounted inside the oven that is heated to 250°C. Three pairs of Helmholtz coils are used to create a uniform magnetic field in three dimensions. The magnetic field average strength is 25 G and a typical gradient in the region occupied by the cell is 2-10 mG/cm.

Laser and optic system

The optic system is described in detail in [6] and a schematic diagram is shown in Fig. 2-9. The divergent laser beam is focused by a lens mounted after the optical fiber. This linearly polarized light is separated into S and P waves by a beam splitter. The P wave part is reflected by a 3 inch mirror, then passes through a quarter waveplate and becomes circularly polarized light. The S wave part passes through a quarter waveplate twice to make the S wave becomes a P wave, then it passes through another quarter waveplate to become a circularly polarized light. The polarization handedness of the light is determined by the fast and slow axes of the quarter waveplate. These axes are oriented at an angle of 45° with respect to the horizontal plane.

Target cell

The target cell is a glass cell containing high pressure ^{3}He gas with 130 - 140 micron thick end windows. The glass walls of the cells were approximate 0.7 mm thick. The thin glass walls were needed to reduce the radiation length of the electrons passing through the glass at scattering angles of 6° or 9°. A typical target cell of the 6 GeV era is shown in Fig. 2-10. The cell consists of two chambers: the pumping chamber and the target chamber. The pumping chamber is where alkali atoms be polarized. They then transfer their polarization to ^{3}He through spin exchange collisions. The target chamber is where the electron beam passes through and interacts with the polarized ^{3}He.

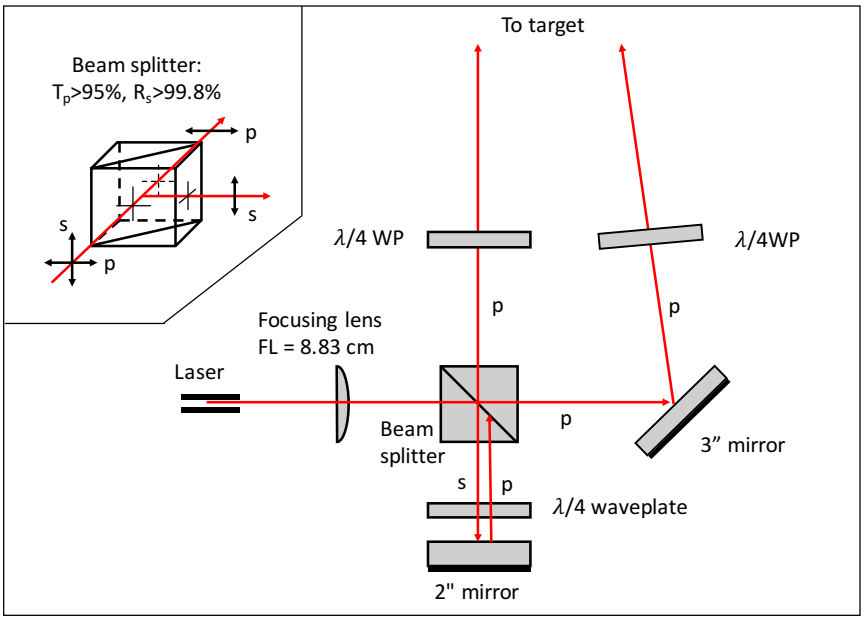

Figure 2-9: Laser optic setup (top view)[67].

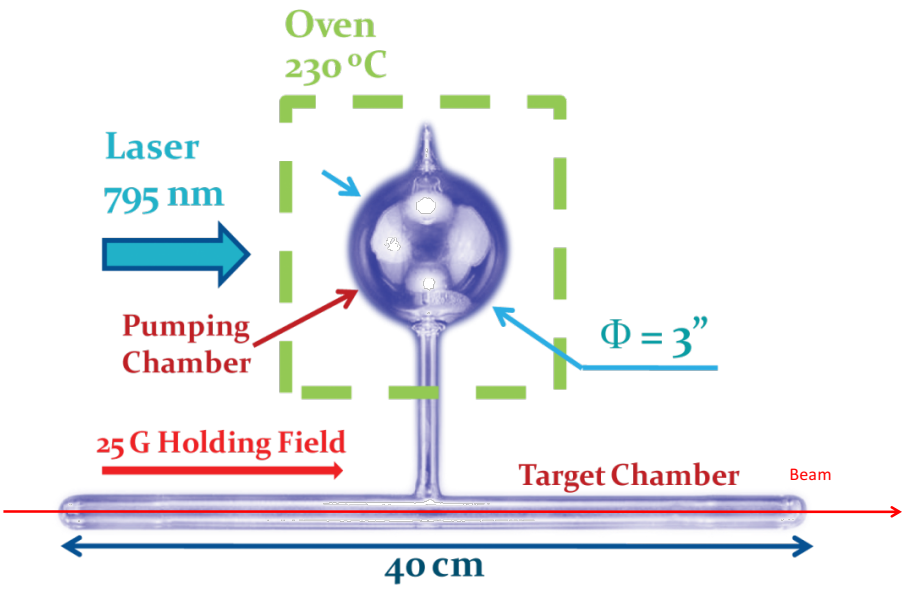

Figure 2-10: A standard 40 cm long target cell used during E97-110.

For low beam energies at 6°, even the thin 0.7 mm walls was not sufficient to reduce the electron's energy loss, so a new design was developed for E97-110 that consisted of an asymmetric cone for the downstream part of the target chamber. The "ice cone" cell is shown in Fig. 2-11. The scattered electrons at 6° from the chamber center would only traverse the end target window of 240 μm thick. This cell reduces the radiation length from the glass walls by a factor of 30. For the first period, the "ice cone" cell was used and the standard cell was used for second period [6]. The characteristics of the "ice cone" cells used in the first period are listed in Table 2.3.

Because the production cell contains ^{3}He and nitrogen, one has to subtract nitrogen contribution to obtain that from clean ^{3}He. Hence, reference cells are used to subtract glass and nitrogen. The shape of the reference cell is the same as the ^{3}He cell, see Table 2.3. The reference cell is either vacuum or filled with nitrogen.

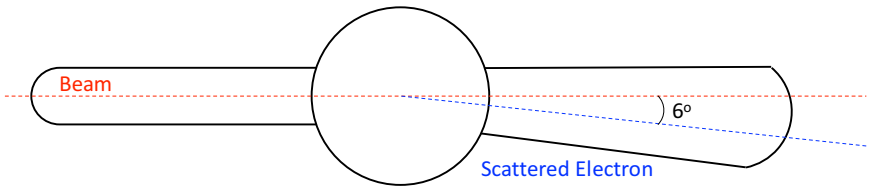

Figure 2-11: Top view of the "ice cone" target cell used during E97-110 (figure not to scale).

Target Polarization

There are two polarimetries to measure the ^{3}He polarization: Nuclear Magnetic Resonance (NMR) and Electron Paramagnetic Resonance (EPR). Details of these polarimetries will be discussed in Chapter 6.

Target Cell	Type	Ave. Density	Entrance	Center	Exit
Proteus	Production	7.9 amg	127 μm	204 μm	234 μm
Proust	Reference	7.0 amg	133 μm	378 μm	384 μm

Table 2.3: Characteristics of the "ice cone" cells used in the first period of E97-110. These cells were studied at the University of Virginia [42]. The target densities are online values. The entrance, center, and exit stand for thickness of glass at entrance window, center of side walls and exit window.

During experiment E97-110, both NMR and EPR measurements had been carried out every six hours. Online target polarization was found to be (29-42)%. A careful study to correct for field gradient produced by the septum magnet is ongoing to extract the final target polarization [63].

2.8 Analysis Flow Chart

Fig 2-12 gives an overview of analysis procedure to extract the spin structures. Raw counts are recorded at detector plane, these counts include a lot of information. In order to extract only clean electron that scattered from ^{3}He at target plane, one needs to apply many corrections. The analysis include: correct for detector efficiency, deadtime, optic study, acceptance study, dilution, background subtraction, and radiative corrections. These steps will be discussed in detail in the next several chapters.

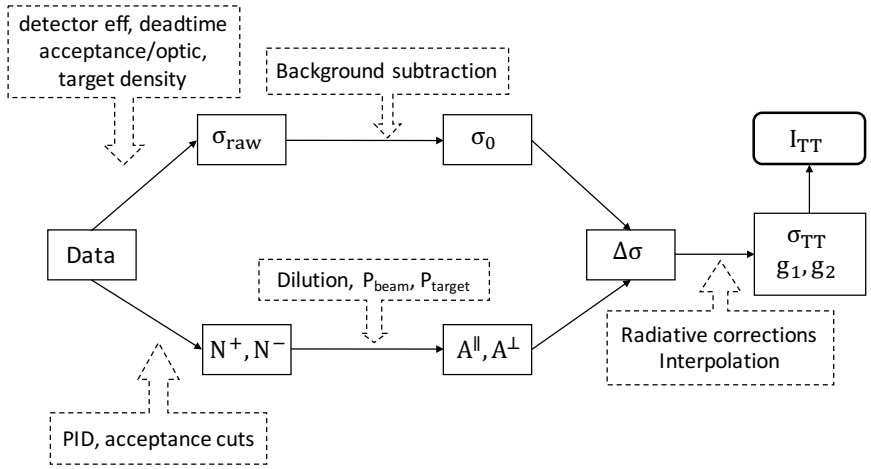

Figure 2-12: Analysis flow chart for extracting cross section differences for experiment E97-110.

Chapter 3

Optics of HRS

In this chapter the optics of HRS will be discussed. In the last section I will show the optic results for the defective septum magnet.

3.1 Septum Magnet

In order to reach the small angles (6° and 9°) necessary for covering the low Q^2 domain, a septum magnet was built and inserted between the HRS and target chamber for this experiment. The minimum angle of HRS without the septum is 12.5°. The main reason for the angle limitation is that the HRS cannot be moved closer to the beamline without Q1 hitting the beam pipe. The schematic setup of the HRS with septum is shown in Fig. 3-1. Since only one septum was available at the time of the experiment, the left spectrometer (HRS-L) was used to detect scattered electrons from a carbon foil target positioned downstream of the main target. Data from HRS-L was used to monitor false asymmetries and the luminosity. Unfortunately, the septum magnet was initially defective due to a mis-wiring of its coils. There are two periods for this experiment: the first period had the mis-wiring problem, while in the second period, the magnet had been fixed and was properly working. The remainder of this thesis will only discuss data from HRS-R in the first period.

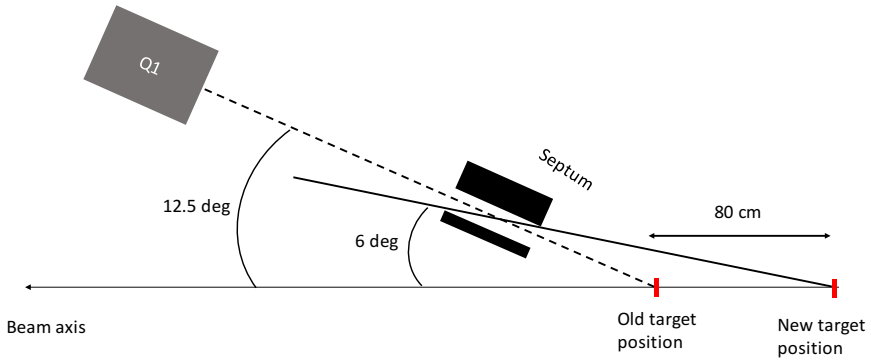

Figure 3-1: A schematic plot of the septum magnet. To accommodate the septum, the target was moved 80 cm upstream.

3.2 Spectrometer Optics

Spectrometer optics is used to relate the measured positions and angles of the scattered electron at the focal plane to its kinematic variables at the scattering vertex. The variables at scattering vertex X_{target} can be mapped to detected variables $X_{detector}$ by the optical matrix $X_{target} \approx MX_{detector}$. M can be written as

$$M \sim M + M^2 + M^3 + \cdots$$

where M is the first order term, and the rest are higher order terms.

In principle, optics can be obtained from field maps based on a well-known magnetic field. However, it would take a large effort to compute it this way. In addition, if there is a misalignment between magnets, then it will introduce a large systematic uncertainty to reconstructed quantities. In order to avoid these complications, several calibration measurements are usually performed to determine the optics using particles of known kinematics, and vertices such as by using sieve slits, multi carbon foils or elastic scattering. Sieve slit is the name for a plate with multiple holes placed at the HRS entrance, which can be used to determine the angular information of

the track. Target foils at different locations along the beamline help to calibrate the reconstructed vertex z. With elastic scattering from a foil target, scattering momenta can be calibrated.

For a focusing spectrometer (such as HRS) with small opening angle, the matrix for optic do not need high orders and most coefficients are zero. But this will not work for a non-focusing spectrometer (mis-wired septum). In this section the calibration procedure used to determine the optic matrix elements for the first period of the experiment E97-110 is described, which is non-conventional due to the mis-wired septum.

3.2.1 Coordinate Systems

In this section, a brief description of various coordinate systems will be presented. For details see Ref. [54].

Target Coordinate System (TCS)

The z axis of the TCS is defined by the line perpendicular to the central sieve slit hole. $\hat{z}_{tg}$ points to the spectrometer. In the ideal case, the z_{tg} axis passes through the hall center. The x_{tg} axis is parallel to the sieve slit surface and pointing vertically down. The distance between the hall center to the midpoint of the central sieve slit hole is defined to be the constant L as shown in Fig. 3-2. The out-of-plane angle (θ_{tg} vertical angle) and the in-plane angle (ϕ_{tg} horizontal angle) with respect to the HRS's central ray are defined as $\theta_{tg} = \tan^{-1}(\frac{dx_{tg}}{dz_{tg}})$ and $\phi_{tg} = \tan^{-1}(\frac{dy_{tg}}{dz_{tg}})$ respectively, and θ_0 is the central angle of the spectrometer.

Focal plane Coordinate System (FCS)

The FCS is obtained by rotating the detector coordinate system around its y-axis by an angle ρ, where ρ is the angle between the local central ray and the $\hat{z}$ axis of the detector coordinate as shown in Fig. 3-3. As a result, the $\hat{z}$ axis of the FCS rotates as a function of the relative momentum $\frac{\Delta p}{p}$.

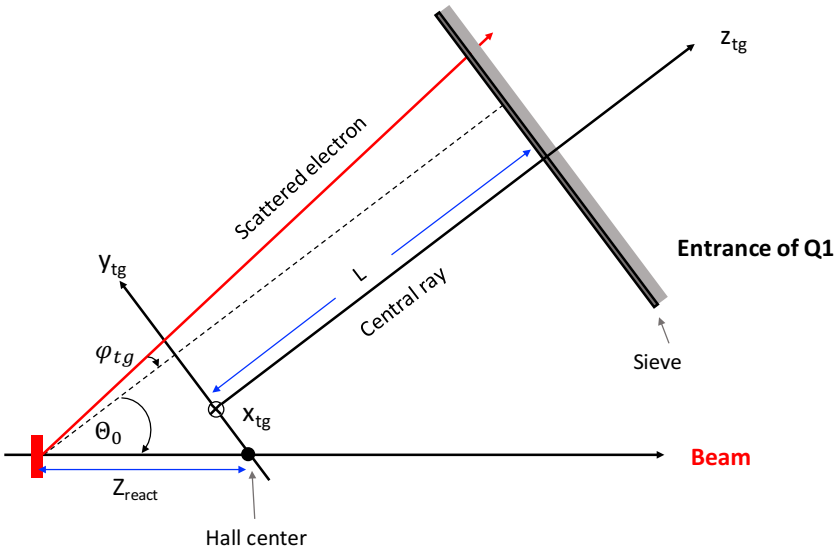

Figure 3-2: Target coordinate system for electron scattering from a thin foil target. The x_{tg} points into the page.

The angles at focal plane are given by $\theta_{fp} = \frac{x_{fp}}{z_{fp}}$ and $\phi_{fp} = \frac{y_{fp}}{z_{fp}}$.

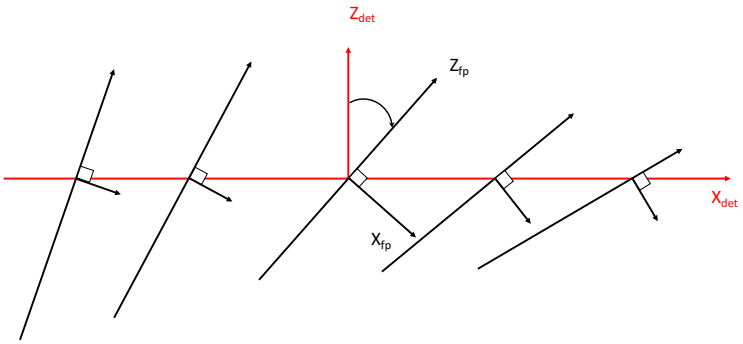

Figure 3-3: The focal plane (rotated) coordinate system as a function of the focal plane position.

3.2.2 Optimization Method

The detector and target quantities are related by the optic matrix elements. The first order relationship between the target coordinates and the focal plane coordinates is shown in Eq. 3.1:

$$\begin{bmatrix} \delta \\ \theta \\ y \\ \phi \end{bmatrix}_{tg} = \begin{bmatrix} \langle\delta|x\rangle & \langle\delta|\theta\rangle & 0 & 0 \\ \langle\theta|x\rangle & \langle\theta|\theta\rangle & 0 & 0 \\ 0 & 0 & \langle y|y\rangle & \langle y|\phi\rangle \\ 0 & 0 & \langle\phi|y\rangle & \langle\phi|\phi\rangle \end{bmatrix} \begin{bmatrix} x \\ \theta \\ y \\ \phi \end{bmatrix}_{fp} \tag{3.1}$$

The dipole spreads particles with different momenta across x_{fp}. So δ_{tg} is strongly correlated with x_{fp} [1]. For the standard i.e without septum HRS configuration, all the quadrupoles are focusing. For simplicity, we can ignore the dipole effect (the spread in x_{fp} due to different momentum), then the correlation between target and focal plane quantities can be shown in Fig. 3-4. ϕ_{tg} is related to y_{fp} and ϕ_{fp} and θ_{tg} is related to x_{fp} and θ_{fp}. There is no correlation between the two angles θ_{tg} and ϕ_{tg}. These relations are shown in Eq. 3.1, in which the mid-plane symmetry of the spectrometers requires the null (zero) elements. Eq. 3.1 is the first order approximation. For standard HRS, the second order contributions are small because the magnets are well made and well aligned [54].

However, the addition of the mis-wired septum magnet invalidates all symmetries. Now, all terms become necessary and appear in the matrix. Fortunately, x_{fp} still represents well the momentum. The complete relation between target variables and focal plane variables can be described by a set of tensors. These tensors are polynomials in x_{fp} and can be written as follows:

$$\begin{aligned} \theta_{tg} &= \sum_{j,k,l} T_{jkl} \theta_{fp}^{j} y_{fp}^{k} \phi_{fp}^{l}, \\ T &= \sum_{i=0}^{m} C_i x_{fp}^{i}, \end{aligned} \tag{3.2}$$

[1] x_{fp} is the long side of the VDC and (+x) is pointing away from the HRS dipole.

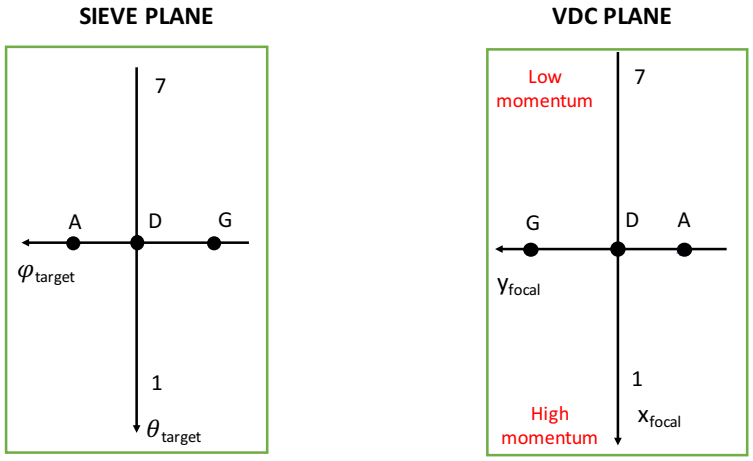

Figure 3-4: Simple picture of particle positions in sieve plane and detector plane. Due to three focusing quadrupoles, particles appear in reverse order at the detector plane in the horizontal direction. For a given HRS magnetic setting, the higher in momentum, the larger in bending radius.

where the C_i are the optics matrix elements for the target coordinate. The indices indicate the power of the focal plane variables. The matrix elements are determined by minimizing χ^2 of the calculated value and the survey actual value.

The matrix to obtain target variables from focal plane variables, i.e. Eq 3.1, is called the Reverse Matrix. Similarly, we can obtain the Forward Matrix which provides focal plane variables from measured target quantities. For the mis-wire septum, we have a sieve slit hole map for each different settings. Each sieve hole location at focal plane depends on a specific combination of target variables.

The optic data include:

- Five scans of the ^{12}C elastic peak that calibrates the spectrometer momentum. They are taken at $DP \equiv \frac{P_0 - P_{12C}}{P_{12C}} = -3\%, -2\%, 0\%, 2\%, 3\%$, with respect to P_{12C}, the momentum of elastically scattered electrons off ^{12}C. By changing the spectrometer central momentum P_0, the carbon elastic peak appears different locations at the focal plane[2]. For a given magnetic field, the higher in momen-

[2]For a given momentum, the higher the magnetic field, the smaller the bending radius (negative x_{focal}) and vice versa. For elastic carbon settings, suppose elastic peak for $DP = 0\%$ setting appears at the middle of the focal plane ($x_{fp} \sim 0$), then a $DP = -2\%$ elastic peak will appear on positive x_{fp} and on negative x_{fp} for a $DP = 2\%$.

tum, the larger in bending radius. Hence, high momentum particle appear at positive x_{focal} as shown in Fig. 3-4. For example, for setting $DP = -2\%$, P_0 is smaller by 2% and the fraction of momentum $\delta p = \frac{P_i - P_0}{P_0}$ for the elastic peak is positive because the momentum of a particle elastically scattered from carbon does not change.

- A set of three thin ^{12}C foils that calibrates the y_{tg} acceptance. The foil thickness is 10 mils (254 μm). Foil locations are $Z = \pm 10$ cm and 0 cm.

- Sieve slit collimator runs to calibrate the horizontal and vertical angles. Due to the mis-wired septum, only the bottom two rows of the holes have understandable optics and are used in the analysis.

For E97-110, the sieve slit configuration is shown in Fig. 3-5. Two holes are 2.7 mm in diameter, and the remaining holes are 1.4 mm in diameter. The larger holes are used to determine the orientation of the image at the spectrometer focal plane. The four columns closest to the beamline are spaced 0.48 cm apart. The next columns are spaced 0.6 cm apart. The vertical spacing between holes is 1.3 cm. Due to the mis-wiring, only the last three rows (1, 2, 3) are visible at the focal plane, the rest did not pass the spectrometer.

In addition to the sieve slit collimator, a set of target collimators were used to block events coming from the target's glass windows [6]. In previous experiments using the polarized ^{3}He target, analysis cuts on the reconstructed target variables (y_{tg}) have been used to remove these events. However, due to the small scattering angles of E97-110, software cuts are not reliable due to the inaccurate reconstruction of the target variables. Hence to remove glass contamination, collimators were necessary.

3.3 Optimization Routine and Results

Due to the abnormal behavior of the septum magnet, the standard optimization package for Hall A [54] cannot be used. In this section, I will provide the procedure that was developed for E97-110 to perform the optics calibration.

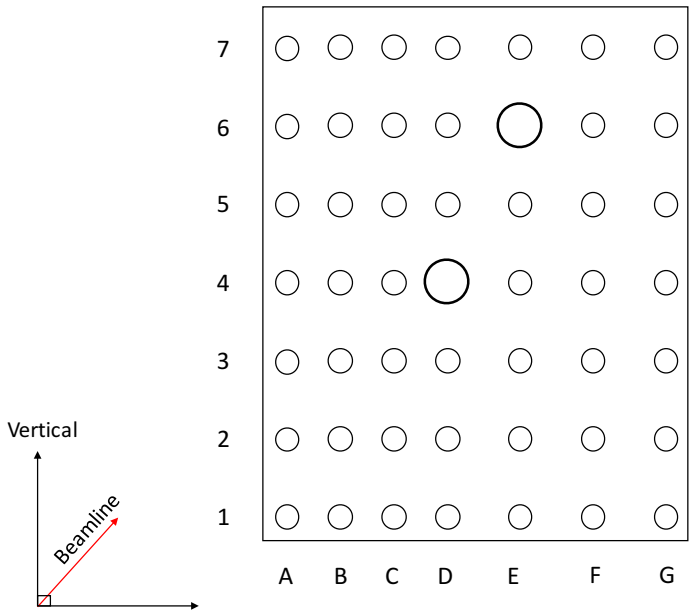

Figure 3-5: Geometric configuration of the sieve slit used during E97-110. Column A is closest to the beamline.

3.3.1 Forward Matrix

The forward matrix is obtained by matching the measured focal plane quantities to the simulated quantities transported to the focal plane using the forward optical matrix. The optimization is done by using TMinuit [55] to get the minimum χ^2

$$\chi^2 = \sum_i^N \frac{y_{data} - y(x_i)}{\sigma_i}, \tag{3.3}$$

where y_{data} are the measured quantities $(x_{fp}, y_{fp}, \theta_{fp}, \phi_{fp})$ and $y(x_i) = f(\delta, y_{tg}, \theta_{tg}, \phi_{tg})$ with f the forward matrix. There is a maximum number of parameters to use for the matrix because of the limited number of data points. In order to determine which term to add into the transport matrix, one needs to check the relation between the two quantities of interest. For example, in order to determine how y_{fp} depends on y_{tg}, one should study the pattern of the sieve slit with different y_{tg}, while other target

quantities are fixed[3]. The number of optic settings limits the higher order terms that can be added to Eq. 3.2. Data from all calibration runs, provided in Table 3.1, are used to determine the matrix elements. There are total 175 data points. However, only 155 data points are used to do optimization because of several reasons. The holes in bold texts are not included in the optimization either because the hole is not completely visible, or the bending is too strong (such as for $DP = 3\%$ case). The forward matrix elements determined from these data are provided in Table 3.2. Fig. 3-6 shows the focal plane quantities from data and simulation. In addition, the mis-wired septum magnet breaks all symmetries so all terms that are necessary for an accurate transport from sieve slit to focal plane.

Furthermore, scattered electrons from the target with the same y_{tg}, ϕ_{tg}, and θ_{tg} should appear at the same locations at focal plane. However, it is not the case for this mis-wired septum, the optics is found to depend on central momentum as well. Hence, the forward matrix need to have central momentum dependence.

3.3.2 Reverse Matrix

The target quantities (δp, y_{tg}, θ_{tg}, ϕ_{tg}) can be obtained from focal plane (detector) quantities (x_{fp}, y_{fp}, θ_{fp}, ϕ_{fp}) using the reverse matrix, given by Eq. 3.2. The coefficients for each reconstructed target quantities are listed in Table 3.3.

The reconstructed δp, y_{tg} are shown in Fig. 3-7 . From this, we can see that the resolution in y_{tg} is about 10 mm. To compare, the y_{tg} resolution (FWHM) for the second period of running of E97110 (with a properly wired septum magnet) is about 4 mm. The reconstructed angles θ_{tg} and ϕ_{tg} are shown in Fig. 3-8. The angles are not as well reconstructed as δp because of the limited optic data. The invariant mass $W - M_C$ is also shown in Fig. 3-7, where M_C is the ^{12}C mass.

[3]One should choose column D (near the center), a fixed row and choose $\delta p = 0$. Because only the first, second and a small part of third row reach the focal plane, with different choice of θ_{tg}, the cross term $\theta_{tg} y_{tg}$ can be determined.

E(GeV)	Run	DP %	Z (cm)	Hole seen
1.1	1869	-3	-10	1(**A**,B,C,D,E,F), 2(D,E,F)
			0	1(A,B,C,D), 2(C,D,E), 3(**E**,F)
			+10	1(A,B,C), 2(**A**,B,C,D), 3(D,E)
1.1	1816	-2	0	1(A,B,C,D,E), 2(C,D,E,F), 3(**E**,F,G)
1.1	1866	0	-10	1(A,B,C,D,E,F), 2(D,E,F,G), 3(F,G)
			0	1(A,B,C,D,E), 2(C,D,E,F), 3(E,F,G)
			+10	1(A,B,C), 2(**A**,B,C,D), 3(D,E)
1.1	1809	2	0	1(A,C,B,D), 2(D,E,**F**), 3(**E,**F,**G**)
1.1	1863	3	-10	1(D,E)
			0	1(B,C,**D**), 2E
			10	1(A,B), 2(C,**D**)
1.5	1566	-2	-10	1(B,C,D,E,F), 2(D,E,F)
1.5	1565	0	-10	1(B,C,D,E,F), 2(D,E,F,G)
1.5	1578	2	-10	1(B,C,D,E,F), 2(E,F)
2.2	2074	-3	-10	1(B,C,D,E), 2(D,E,F)
			0	1(A,B,C,D), 2(**B**,C,D,E)
			10	1(A,B,C), 2(**A**,B,C,D)
2.2	2071	0	-10	1(B,C,D,E,F), 2(D,E,F,G)
			0	1(A,B,C,D,E), 2(C,D,E,**F**)
			10	1(A,B,C), 2(**A**,B,C,D)
2.2	2068	3	-10	1(**D**,E), 2(**E**,F)
			0	1(B,**C**,D), 2(E)
			10	1(**A,B**), 2(C,D)

Table 3.1: Optic data with different beam energies, momenta and foil positions. $-10, 0, +10$ cm are the upstream, center and downstream foils, respectively. For each foil the visible sieve holes are listed. The numbers correspond to row number see Fig. 3-5. The hole label maps for run 1566 and 1578 were obtained by interpolating from $DP = 0, \pm 3$ %.

3.4 Mis-wired septum Magnet Behavior

The septum magnet is used to bend particles from a scattering angle of $6^\circ \pm 2^\circ$ to $12.5^\circ \pm 2^\circ$ so they can enter the HRS. During the first period, because the bottom coil of the septum magnet worked properly while the top coil was wired with the wrong polarity, particles were bent in the wrong (opposite) direction if they enter the top half of septum. Fig. 3-9 shows how the magnetic field behave for two coils with current running in the same and opposite direction. The proper configuration on the left panel of Fig. 3-9 display a uniform field acting as a dipole that bend all

the particles. The defective configuration on the right panel showed the configuration with which the first period had to run with. The configuration is that of a quadrupole, unable to properly bend all the particles toward the HRS.

3.4.1 Sieve Slit Pattern

Because of the mis-wired septum, particles that enter the top part of the septum, which corresponds to the fifth, sixth and seventh rows of the sieve slit as shown in Fig. 3-5, are not deflected to the HRS entrance. At the middle of the magnet (4th row), the net field from the septum is zero, so particles entering the septum at $\Theta_0 = 6°$ and more importantly $\theta_{tg} = 0$ felt no field at all. Only particles going through the last three rows of the sieve slit—the first, second and the third rows—would reach the HRS entrance. Since the distance between sieve holes is not symmetric around the center of the sieve (column D), particles going through different holes are bent with different strength. In addition, particles are bent upward (downward) if they are on the left (right) side of column D as shown in Fig. 3-10. Further from the bottom row, the effect from the top coil becomes stronger, while that from the bottom coil becomes weaker. Consequently, most of the particles could not reach the HRS entrance. Fig. 3-10 shows the effect of the mis-wired magnet. Columns C, D, E represent different ϕ_{tg} and $\phi_{tg} = 0$ for D. In the sideview, the red arrows represent the magnetic field direction. The blue arrows show the force exerted on the electrons. With different momentum settings (current settings), the bending[4] is different. This is shown in two colors: pink for low B field and light green for high B field, respectively. As shown in the side view of entrance of HRS, the green band is bent more than the pink band. The bands in focal plane are flipped due to the HRS quadrupoles.

3.4.2 Sieve Pattern With Different Target Positions

Table. 3.1 shows the sieve hole pattern observed for different magnet configurations for the multifoil carbon target. The reason for the observed pattern is as follow:

[4]Here, the bending comes from septum magnet, not the HRS yet.

The magnetic field at the first row (1A through 1G in Fig. 3-11) has enough strength, so most of these holes are seen regardless of the foil z position. Starting from the second row (row 2), the field strength is weaker compared with the first row, so the bending will not be enough to bring particles to the HRS entrance. A clear pattern can be seen from the upstream ($z < 0$) to the downstream ($z > 0$) foils: the scattering angle from upstream is smaller compared with the downstream one, see Fig.3-11, and thus needs stronger magnetic field to bend toward the HRS entrance, especially for holes on the small angle edges (A, B, C). However, the field strength is not enough so only 2D, 2E, 2F, 2G are seen. For downstream foil ($z > 0$), the opposite happens: the field bending for the larger angle edge (D, E, F, G) is too large and only 2A, 2B, 2C are seen.

The result for the forward and backward transport matrices is listed in Table 3.2 and Table 3.3, respectively. One example of x_{fp} and δp is written as follows:

$$\begin{aligned} x_{fp} = &-0.4 + 13.9\delta p - 35.2\delta p^2 - 21.8\phi_{tg} + 32.8\phi_{tg}^2 - 15.3y_{tg} + 12.5\theta_{tg} - 68.6\theta_{tg}^2 \\ &+ 172.9y_{tg}\theta_{tg} + 252.4\theta_{tg}\phi_{tg} - 1.0P_0\theta_{tg} + 1.52P_0\phi_{tg} + 1.3P_0y_{tg}, \end{aligned} \tag{3.4}$$

where the coefficients are from the x_{fp} column in Table 3.2, kept to one significant figure after the decimal point.

$$\delta p = 0.007 + 0.077x_{fp} + 0.113y_{fp} + 0.507\theta_{fp} + 0.405\theta_{fp}x_{fp} + 4.014\theta_{fp}^2, \tag{3.5}$$

where the coefficients are from the δp column in Table 3.3, kept to three significant figures after the decimal point.

Parameter	x_{fp} (m)	y_{fp} (m)	ϕ_{fp} (rad)	θ_{fp} (rad)
Offset	-0.414179	-0.051197	0.039396	0.045596
δp	13.8555	-0.652497	-0.893291	-0.040309
δp^2	-35.1653	-	-	-
ϕ	-21.7796	0.531578	1.89858	2.63222
$\phi\delta p$	-	-29.1303	-21.8079	-
ϕ^2	32.7665	25.7656	-10.1326	
y	-15.2961	0.194259	1.60488	1.57033
$y\delta p$	-	-17.6567	-15.3232	-
$y\phi$	-	22.1518	-	-
θ	12.4787	1.8026	-1.23964	-1.12437
θ^2	-68.7814	-10.664	-	-
$\theta\delta p$	-	20.3194	29.008	-
θy	172.863	-	-	-13.0275
$\theta\phi$	252.423	-5.46078	20.8642	-31.1391
P_0	0.035416	0.001714	0.000741	-0.004017
$P_0\theta$	-0.969692	-0.10275	0.057364	0.010362
$P_0\phi$	1.51612	-0.057778	-	-0.051289
$P_0 y$	1.29891	-	-	-
Input σ_i	9 mm	0.6 mm	2.8 mrad	1.8 mrad
χ^2 /n.d.f	2.96	5.29	1.67	1.29
# parameters	14	15	12	10

Table 3.2: Coefficients for the forward matrix. The parameters are quantities at the target location. There are in total 51 parameters (14 for x_{fp}, 15 for y_{fp}, 12 for ϕ_{fp}, 10 for θ_{fp}). The number of data points used for optimization is 155. The input σ_i is determined by choosing a single hole and applying a Gaussian fit. The terms which are not included are not used in the optimization. P_0 is central momentum of HRS.

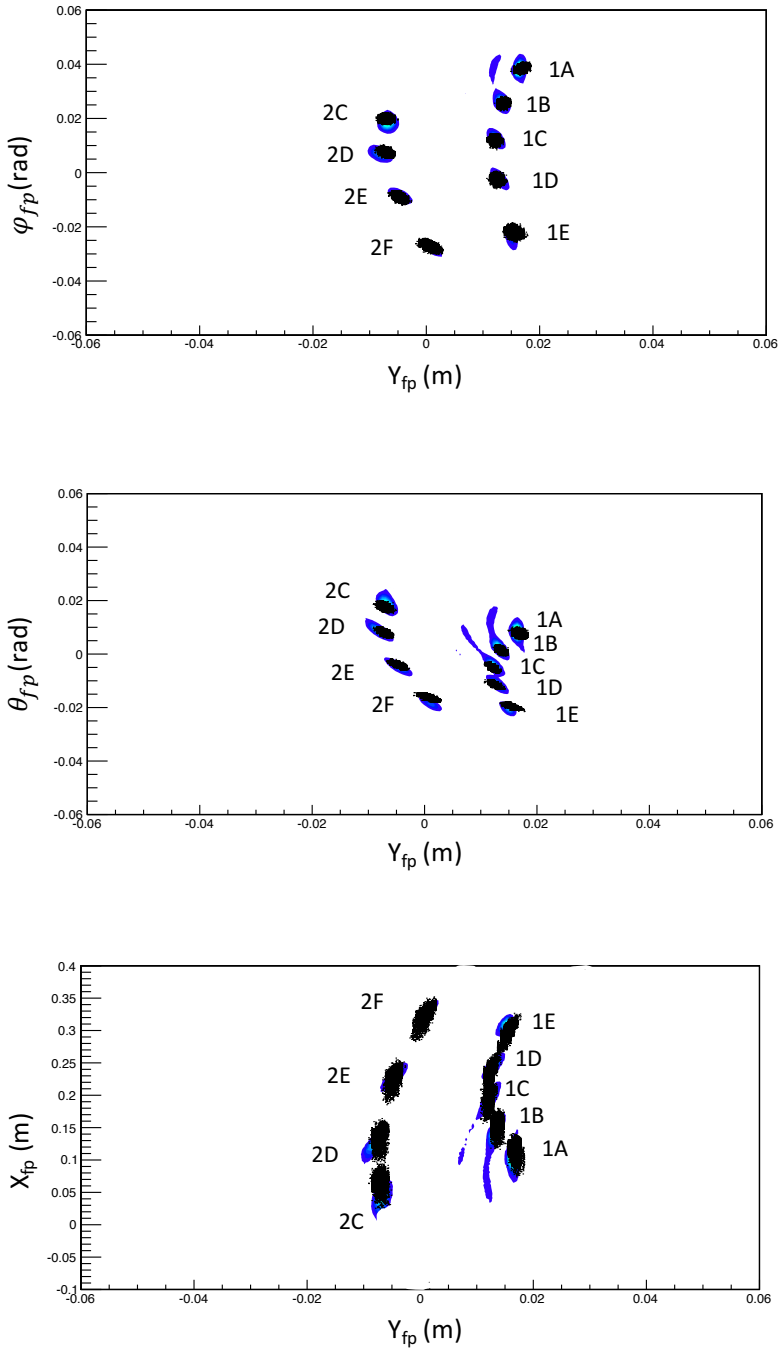

Figure 3-6: Experimental and simulated data at the focal plane. The forward matrix is used in a simulation to transport particles from target to focal plane. The horizontal axis is y_{fp} (m) for the three panels. Simulation is in black color and it is on the top of data which are in color points. These data are from elastic carbon with sieve slit in for setting $DP = -2\%$ and $Z = 0$ cm (run 1816). The labels in the figures indicate the sieve slit holes as shown in Fig. 3-5.

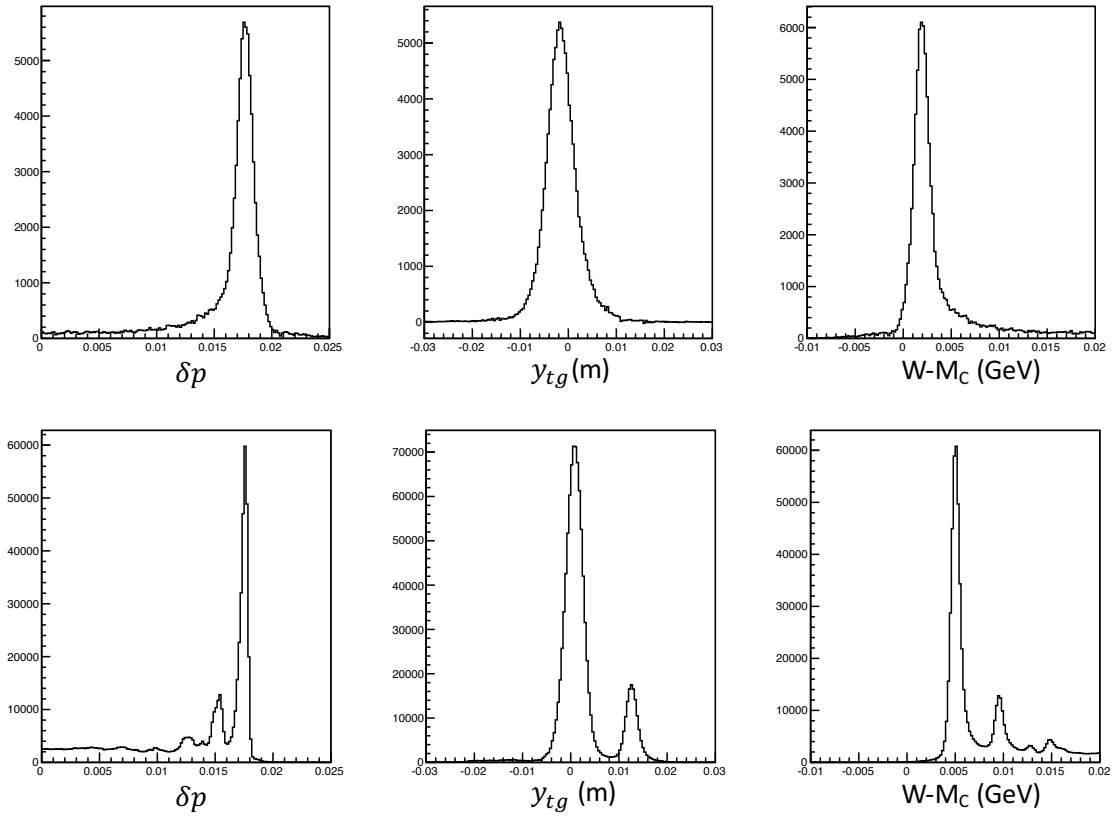

Figure 3-7: Reconstructed δp (left), y_{tg} (center) and $W - M_C$ (right). The top three plots are data from first period for central foil ($z = 0$) with $\delta p = -2\%$ and without sieve slit (run 1909). Focal plane limit cuts, analysis cuts (θ_{tg} vs ϕ_{tg} to choose 1CD & 2CD, PID) are applied. For comparison of resolution, the bottom three plots are data from second period (properly wired septum) for multifoil ($z = -20, 0, +10$ cm) with $\delta p = -2\%$ and without sieve slit (run 2401). As one can see, the resolution of all 3 variables are poorer in first period due to mis-wired septum. Here kinematic between two periods are not the same as one can clearly observe carbon excited state peaks from second period.

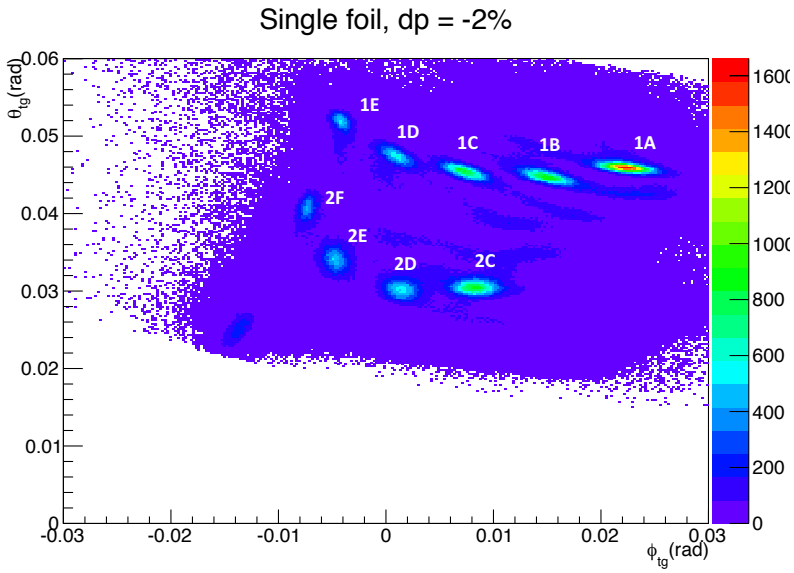

Figure 3-8: 2D plot for optic run taken with sieve slit. ϕ_{tg} is the horizontal angle, θ_{tg} is the vertical angle.

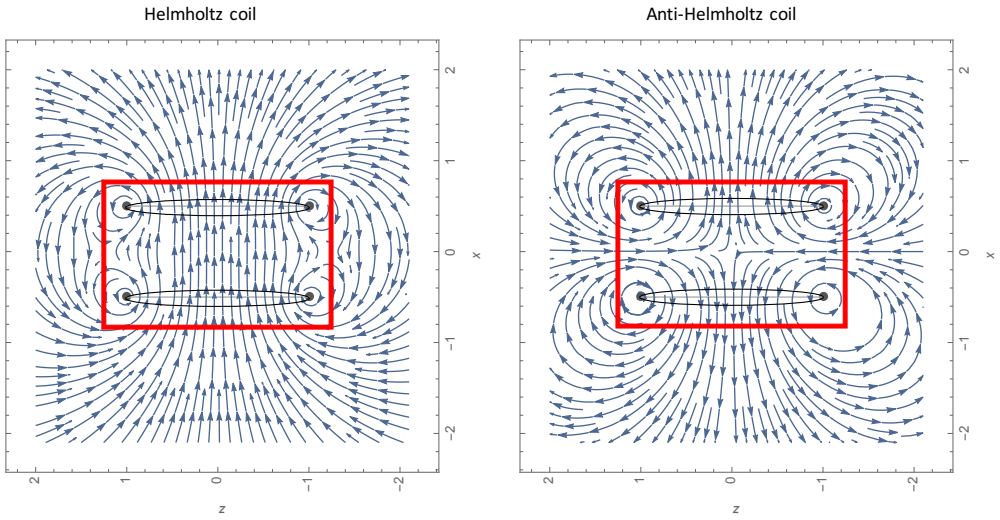

Figure 3-9: Magnetic field strength for two configurations: The left panel shows the proper septum configuration used in the second period: field from 2 coils with current running the same direction. The right panel shows the defective configuration used during the first period: field from 2 coils with current running in opposite direction. The configuration left creates a uniform magnetic field inside the red box (second period). The right configuration creates a very different field (first period).

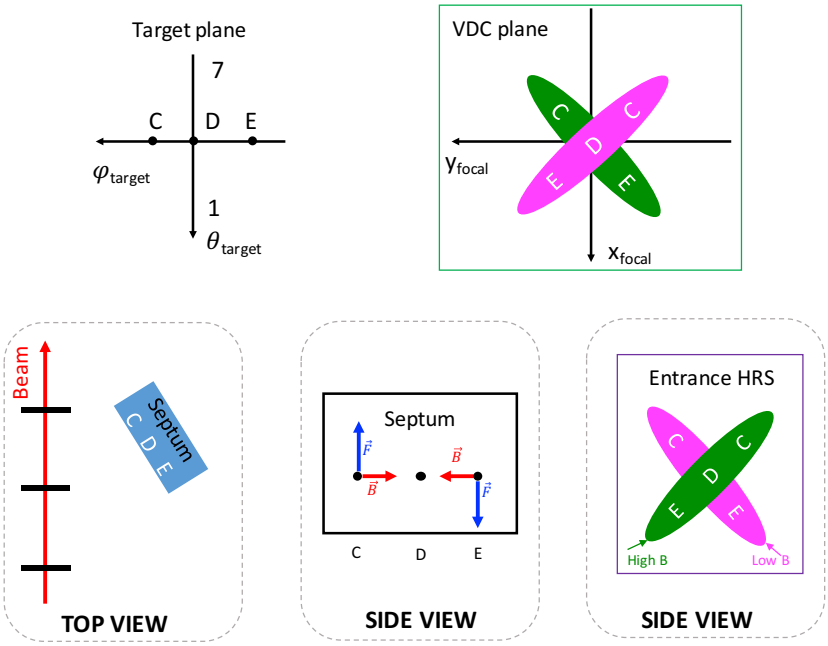

Figure 3-10: The mis-wired septum bent particles with different scattering angle ϕ_{tg}. Column D is at the center of the sieve slit. Top left plot shows columns C, D, E in the target plane, 1 represents first row, 7 represents 7th row in the sieve slit as shown in Fig. 3-5. Top right plot shows how different magnetic field strengths of the septum make the particles arrive at different locations at the focal plane, the green band is with high septum current, the pink band is with lower septum current. The bottom left plot shows the top view in Hall A. The bottom middle plot shows how the magnetic force exerted on different directions for electron on the left or on the right of the magnet's middle plane. As seen from Fig. 3-9, the magnetic field is pointing at different directions for a constant θ. The bottom right plot shows the side view of the HRS entrance with differents strength of septum magnet.

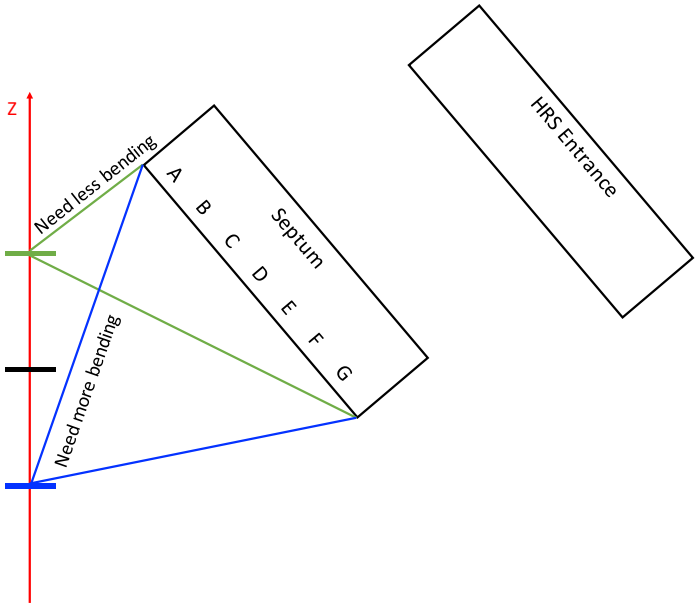

Figure 3-11: Sieve slit with carbon foils at three locations ($z = \pm 10, 0$ cm). Due to weaker magnetic field in second row, upstream (blue color foil) can be seen only D, E, F, G and A, B, C, D for downstream (green color foil). The difference comes from different in scattering angles. (Relative locations are not exact scale).

Parameter	δp	y_{tg}	θ_{tg}	ϕ_{tg}
Offset	0.006575	0.0015	0.038	0.0023
x_{fp}	0.077224	0.0056	-0.0038	-0.007
y_{fp}	0.112585	0.384	0.693	0.235
θ_{fp}	0.507202	0.513	-2.269	-0.039
ϕ_{fp}	–	-0.395	0.041	0.410
$\theta_{fp}x_{fp}$	0.404832	–	–	–
$y_{fp}\phi_{fp}$	–	3.650	–	-16.356
$y_{fp}\theta_{fp}$	–		–	16.0
$\theta_{fp}\phi_{fp}$	–	-16.369	–	–
y_{fp}^2	–	7.230	–	-1.740
θ_{fp}^2	4.01425		–	5.575
ϕ_{fp}^2	–		–	
# parameters	6	8	5	9

Table 3.3: Reverse matrix coefficients used to reconstruct target quantities. The parameters are in term of focal plane quantities. The terms which are not included are not used in the optimization.

Chapter 4

Elastic Scattering Analysis

In this chapter the analysis of the elastic carbon, ^{3}He, and N_2 cross sections will be discussed. Carbon elastic cross section is well-known, so it is used to calibrate the HRS optics and acceptance. Analyzing elastic carbon data is the first step for the cross section analysis of the experiment because the target length, target density, and the momentum of elastically scattered electrons are well defined. Once carbon elastic data are well-understood, elastic scattering from the extended ^{3}He cell is analyzed to confirm the reliability of the cross section extraction and assess the effects of extended targets. Results presented in this chapter show that the focal-plane and target-plane method works well in extracting cross sections from both foil and extended targets. This method will be used to extract polarized inelastic cross sections, which constitute the main physics results of this thesis, and will be presented in the next chapter.

4.1 Carbon Elastic Cross Section

The elastic Born cross section can in principle be extracted from data as follows:

$$\frac{\sigma_{exp}^{Born}}{d\Omega} = \frac{N_{raw}}{N_{tg}} \times \frac{PS_1}{LT \times Q/q \times \epsilon} \times \frac{RC}{\Delta\Omega_{geo} \times Acc}, \tag{4.1}$$

where:

- PS_1 is the prescale factor for event type T_1.

- N_{raw} is the number of elastic events after applying detector and acceptance cuts.
- ϵ is total efficiency including trigger, tracking and PID cut efficiencies.
- RC is the radiative correction factor, defined as $\frac{\sigma_{Born}}{\sigma_{radiated}}$.
- Acc is the angular acceptance correction factor.
- $\Delta\Omega_{geo}$ is the geometric solid angle.
- Q/q is the number of beam electrons incident on the target, with q the electron charge 1.6×10^{-19} C.
- N_{tg} is the number of target particles seen by the beam per unit area (target density times target length).

The correction factors RC and Acc are included in the elastic simulation [62] and thus do not need to be corrected for. In other words, the simulation calculates the actual experimental cross section rather than the Born one. The $\Delta\Omega_{geo}$ is the actual geometry of the distribution of detected particles at the detector plane.

4.1.1 Simulated Cross Sections

In order to obtain simulated cross sections, the same cuts as data are used. These include cuts to define the solid angle and a cut on W. The solid angle is determined based on the sieve hole positions (the actual carbon cross section run is without the sieve slit in). For this analysis, because of the imperfect transport matrices from the mis-wired septum, the hole positions are not well-reconstructed and Acc can not be accurately determined. On the other hand, the focal plane variables agree well between data and simulation. Therefore, a method based on the focal plane and target variables is developed and the cross section was determined by comparing data to a simulation.

The simulated cross section is obtained by the following steps:

1. Using a carbon sieve slit run, a cut on the reconstructed quantities is used to select the center of a sieve hole at the target plane. The sieve holes are identified from the sieve position data (Fig. 3-8). This cut, applied for multiple sieve holes, are used to defined a polygon region.

2. The phase space at the target is determined using target quantities generated by the Monte Carlo (M.C.)'s phase space configuration (no physics event generator, multiple scattering and photon radiations turned off). The quantities used are the ones originally generated (not the one reconstructed). By choosing a 2D ϕ_{target} and θ_{target} range (reconstructed angles), the solid angle is simply calculated by $\Delta\theta_{or} \times \Delta\phi_{or}$ (the originally generated angles). This phase space is the solid angle one needs to use for the data.

3. The M.C. is then run with elastic event generator and photon radiations enabled. We count the number of events that remain inside the area defined in step 2 and that survived a cut on the initial $W - M_C$ (with M_C the carbon mass) distribution, i.e. before photon radiation, transport and reconstruction are applied. We name number *tacc*.

4. Once the simulated particles are transported to the focal plane, a 2D cut on the focal plane is applied. This 2D cut is defined by boundaries formed by y_{fp} and ϕ_{fp} as in Fig. 3-6, which is a function of momentum δp, details are listed in A.1. The number of events that survive the cut in step 2, focal plane cut and a cut on radiated $W - M_C$ distribution are counted. This number is named *cacc*. We then sum the computed elastic cross section σ_i, where i design a surviving event of given θ, ϕ, radiation effected δp and y_{tg}, over all surviving events. The simulated cross section is calculated as [62]:

$$\langle \frac{d\sigma}{d\Omega} \rangle = \frac{\sum_{i=1}^{cacc} \sigma_i}{tacc}. \tag{4.2}$$

4.1.2 Experimental Cross Sections

In our method, factors RC and Acc are folded in the simulated cross section, and we extract the experimental cross section as:

$$\frac{\sigma_{exp}}{d\Omega} = \frac{N_{raw}}{N_{tg}} \times \frac{PS_1}{LT \times Q/q \times \epsilon} \times \frac{1}{\Delta\Omega_{geo}}, \tag{4.3}$$

The experimental cross section is obtained with the following steps:

1. PID cuts are applied to select electrons and single track events. The PID cuts for Right HRS are:

   - Gas Čerenkov: $\sum$ ADC > 350.
   - Lead glass counters: $E_{psh} > 0.105\ p_0$, $E_{psh} + E_{sh} > 0.78\ p_0$.

   where $\sum$ADC is the summed ADC signal of the gas Čerenkov detector, E_{psh} and E_{sh} are respectively the energy deposited in the preshower and the shower counters in MeV, and p_0 is the HRS central momentum in MeV/c.

2. We then subtract the background (mostly coming from the ^{4}He gas that fills the target chamber) to obtain the pure carbon spectra, see Fig. 4-1. Data without target were taken to determine this ^{4}He background. Since the no-target run (background) and carbon run (carbon plus background) are not taken in exactly the same conditions (such as integrated current, prescaler, livetime, efficiency), a scale factor must be applied. The scale factor applied to the ^{4}He run is:

$$\text{Scale factor} = \frac{PS_2}{PS_1} \times \frac{LT_1 \times \epsilon_1 \times Q_1}{LT_2 \times \epsilon_2 \times Q_2}, \tag{4.4}$$

   where PS are prescaler factors, ϵ denotes the total detector efficiency, Q is the electron beam integrated charge, and subscripts 1 and 2 are for the carbon and ^{4}He background runs, respectively. There is a difference in photon radiation effects when subtracting ^{4}He from carbon run [1]. However, this difference is

[1] An electron does not lose much energy when crossing ^{4}He compared with crossing carbon. Hence when subtracting the two spectra, the subtraction is not perfect due to invariant mass (or DP) distributions being slightly different.

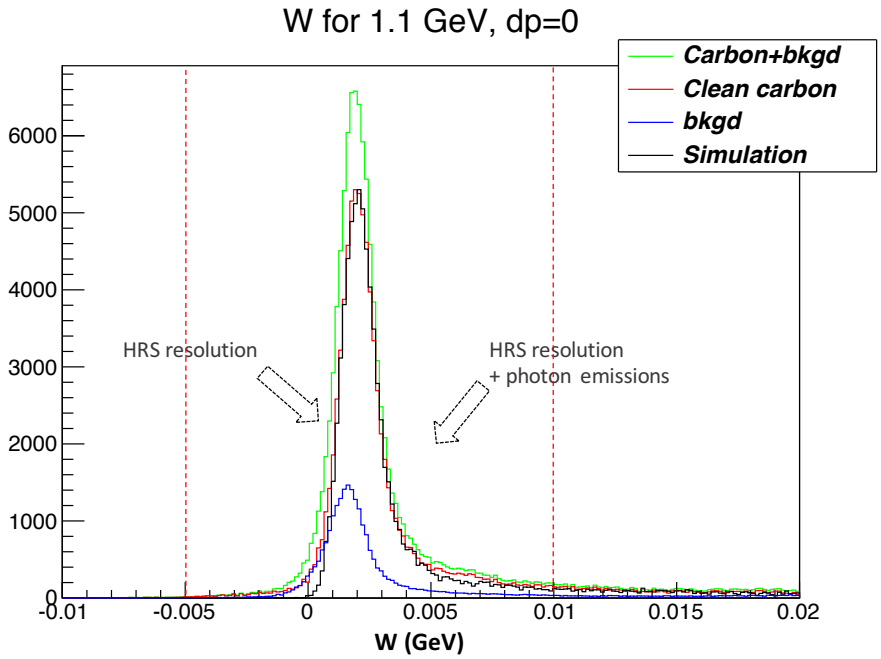

Figure 4-1: $W - M_C$ spectrum for single carbon foil. Green is the raw carbon run (run 1899), Blue is no target (i.e mainly ^{4}He) run (run 1898), Red is the clean carbon (Blue subtracted from Green with appropriate scale factor) and Black is the simulation. The width on the left side of the peak is mostly due to HRS resolution. On the right side, the shape of the peak (tail) results from the convolution of HRS resolution and the secondary photon emissions (Bremstrahlung). The larger the radiation length, the bigger the tail is. The vertical axis is the yield normalized by charge, efficiency, livetime, and prescale factor. The red dashed lines show the -0.005 $<$ W $<$ 0.01 GeV cut used in the analysis. An additional scale factor was applied to have the matching in height between two spectra.

negligible.

3. A 2D cut on the focal plane to choose event stay inside flat acceptance area. Then another 2D cut at reconstructed θ_{tg} and ϕ_{tg} is applied as shown in Fig. 4-2. Holes 1C, 1D, 2C & 2D are chosen for the cut because these holes appeared for all momentum settings. Since the sieve positions are a function of y_{tg} and momentum, the positions are different for each momentum setting. Table 4.1 lists the sieve positions that were used to obtain the cross section. In addition, a cut on the invariant mass $W - M_T$ is added to select the elastic peak. No cut on y_{tg} is necessary for these runs, since they are taken with a single carbon foil

at $y_{tg} = 0$. We cannot analyze multifoil carbon runs because the combination of mis-wired septum and target collimator blocks most of the events originated from the upstream and downstream foils.

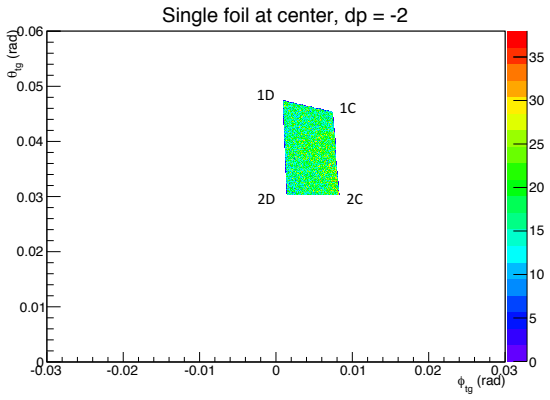

Figure 4-2: Cut to select the (1C, 1D, 2C, 2D) area from experimental data. This cut is applied to target reconstructed quantities (ϕ_{tg}, θ_{tg}).

4. Cut on invariant mass $W - M_C$. A loose cut -0.005 < W < 0.001 GeV (red dash lines in Fig. 4-1) is applied in order to stay away from the peak region which is sensitive to secondary photon emissions (essentially external and internal Bremstrahlung, see Section 5.4). Besides, there is a small contribution from nuclear excited states of carbon which is not visible in the W-spectrum because of the wide width of the elastic peak. This contribution is estimated by subtracting the simulated W-spectrum from the data[2]. The number of residual counts provides the contribution from ^{12}C excited state. Then we take the ratio of this number to the total number of counts from data within the chosen W cut ($-0.005 < W < 0.01$ GeV). A W-spectrum showing both simulation and data is provided in Fig. 4-1.

5. We then correct for the various detector inefficiencies: PID, trigger and multitrack inefficiencies. The normalizations for each run used in the ^{12}C analysis are given in Table 4.2. The N_{raw} in Eq. 4.3 is determined at this stage.

[2]This method of subtraction make assumption that the normalization is good enough. It gives a rough idea of how much the contribution from excited state is.

Energy	dp = -2 %		dp = 0 %		dp = 2 %	
	ϕ_{tg}	θ_{tg}	ϕ_{tg}	θ_{tg}	ϕ_{tg}	θ_{tg}
1.1 GeV	0.009205	0.029676	0.015501	0.033456	0.019807	0.037648
	0.003033	0.030742	0.005401	0.032434	0.007751	0.034223
	0.000862	0.048579	0.000550	0.044983	-0.000548	0.041738
	0.006246	0.047371	0.006014	0.046525	0.006263	0.045879
1.5 GeV	0.011117	0.028855	0.015932	0.033179	0.020248	0.037331
	0.003680	0.030644	0.005756	0.032312	0.008377	0.034021
	0.001050	0.048253	0.000511	0.044675	-0.000584	0.041518
	0.006548	0.046910	0.006307	0.046004	0.006090	0.045286
2.2 GeV			0.016110	0.032375		
			0.006620	0.031878		
			0.000885	0.044495		
			0.007051	0.045268		

Table 4.1: Experimental sieve slit hole centers from reconstructed θ_{tg} (rad) and ϕ_{tg} (rad) for three beam energies for which the elastic reaction was measured (only large W data was taken at $E = 3.3$ GeV). For 2.2 GeV, only dp=0 % is available. These boundaries are used in simulation and data for elastic carbon analysis. For each setting, the sieve hole center position is given in ϕ and θ. They correspond to (from top to bottom) 2C, 2D, 1D, 1C.

Target (run #)	PS	LT	Q [μC]	ϵ_{PID}	$\epsilon_{multitrack}$	$\epsilon_{trigger}$
Carbon (1899)	100	0.996	1575.9	0.98	0.749	0.9994
^{4}He (1898)	25	0.996	758.2	0.98	0.927	0.9986

Table 4.2: Normalization factors for elastic carbon target and ^{4}He (no-target) runs.

6. $N_{tg} = \rho_{12C} \times L$ where $\rho_{12C} = 1.933$ g/cm^3 is carbon density and $L = 0.0254 \pm 0.000508$ cm is the carbon thickness.

7. Finally, the counts should be normalized to the geometrical solid angle $\Delta\Omega_{geo}$. It is determined either from the sieve survey (area of sieve holes from the above cut), or it can be determined from the simulation. For run 1899 with four holes (1C, 1D, 2C, 2D), solid angle $\Delta\Omega_{\text{sieve survey}} = 98.9 \times 10^{-6}$ sr from survey information [56] and $\Delta\Omega_{sim} = \Delta\theta_{or} \times \Delta\phi_{or} = 90.0 \times 10^{-6}$ sr from the simulation. The latter is used in calculating the experimental cross section. The difference in the solid angles between survey and simulation is due to the forward and reverse transport matrices, and will be taken into account as part of the uncertainties.

In addition, the HRS+defective septum resolution is determined from carbon spec-

trum. The 1.5 GeV setting was taken at the beginning of the running period, hence the amount of ice is smaller compare to the rest (the subject of ice building up will be discussed in next section). Consequently, the HRS+septum resolution for this energy setting is better, $\delta p/p = 2.8 \times 10^{-4}$. For 1.1 and 2.2 GeV, $\delta p/p = 4.0 \times 10^{-4}$ due to more ice accumulating on the surface of the insulating polystyrene foam. These numbers will be used for other different targets.

4.1.3 ^{12}C Cross Section Uncertainties

The following section lists all the systematic uncertainties for experimental and simulated carbon elastic cross section analysis.

Experimental Data

- Statistic: $< 1\%$.
- Beam current: 2%. The uncertainty on the beam current in Hall A is typically $\sim 1\%$ [39]. However, since the E97110 runs were usually conducted at smaller than usual beam current (1 or few μA) due to high rates, we use 2% as our uncertainty.
- Target length, density: 2% [56].
- VDC efficiency: $< 3\%$[3]. VDC multitrack efficiency is studied in [57]. The upper limit of systematic uncertainty of VDC efficiency is given by the VDC inefficiency.
- Acceptance: 0%. In this document, only single carbon foil results are studied within the very small solid angle defined in Table 4.1 (see also Fig. 4-2). Furthermore, the elastic peak is at $|\delta p| \leq 2\%$. Therefore we assumed that the acceptance is well-defined.
- Solid angle: 6%. This uncertainty comes from how well we determine the sieve center, typically $\Delta\phi = 6.0 \pm 0.2$ mrad, $\Delta\theta = 16.6 \pm 0.4$ mrad.

[3]Some elastic runs have low efficiency. On average $\epsilon_{VDC} \approx$ 1-2%.

All these uncertainties are uncorrelated and can therefore be added in quadrature. The resulting total systematic uncertainty in the extracted experimental cross section is about 8%.

Simulation

- Transport functions: 10%. The solid angle used in the experimental cross section does not perfectly match with the sieve survey solid angle as mentioned in step 6 of the procedure of obtaining the experimental cross section. This is due to the imperfect transport functions (both forward and backward).
- Beam energy: ± 0.5 MeV ($< 1\%$).
- Ice thickness: 10 ± 3 mm ($\sim 6\%$). During the experiment, ice from air humidity built up on the surface of the polystyrene foam that thermally isolated the septum bore from the target chamber. The precise amount of ice is unknown and it was scrapper off periodically during the experiment. The ice thickness is estimated by comparing the radiative tail of $W - M_C$ spectra of the carbon elastic peak between data and simulation. Ice thickness uncertainty from the second period is typically 1.5 mm [61]. However, this number cannot be determined exactly for the first period due to non-perfect transport, and we double the typical 1.5 mm uncertainty.
- Spectrometer angle: $5.91^\circ \pm 0.04^\circ$ ($\sim 3\%$ in cross section) [56].

Like for experimental uncertainties, these error are essentially uncorrelated and can thus be added quadratically. Total systematic uncertainty for the expected cross section from simulation is about 12%.

4.1.4 ^{12}C Elastic Cross Section Results

Table 4.3 shows simulated and experimental cross sections for all the three beam energies (1.1, 1.5 and 2.2 GeV) for which the elastic reaction was measured, and three HRS momentum settings. They agree within uncertainties. This gives us the

confidence that the focal-plane and target based cross section extraction method works well, at least for the single foil data presented so far.

Energy / DP	Run	HRS Momentum Resolution	Cor %	σ_{sim} (μb)	σ_{data} (μb)	Rel. dif. %
1.1 GeV				(syst ± 13%)	(syst ± 8%)	
Dp = -2%	1909	5.0×10^{-4}	2	5046	4639	8%
Dp = 0%	1899	4.0×10^{-4}	1	5258	5164	2%
Dp = 2%	1889	4.0×10^{-4}	0	5293	5576	-5%
1.5 GeV						
Dp = -2%	1636	2.8×10^{-4}	5	1658	1640	2%
Dp = 0%	1603	2.8×10^{-4}	5	1719	1649	4%
Dp = 2%	1599	2.8×10^{-4}	5	1725	1825	-6%
2.2 GeV						
Dp = 0%	2078	3.0×10^{-4}	18	106	103	3%

Table 4.3: Comparison of cross sections from simulation (σ_{sim}) and experimental (σ_{data}) for a single carbon foil at $z = 0$ with three different beam energies and different central HRS momentum setting (DP). The cuts on W are the same for all setting: $-0.005 < W < 0.01$ GeV both on simulation and data. The third column is the HRS momentum resolution. The fourth column (Cor %) is the correction due to contribution from ^{12}C excited states. The last column is the relative difference: Rel. Dif. $= \frac{\sigma_{sim}-\sigma_{data}}{\sigma_{sim}}$. The ice thickness is 8 mm, 15 mm, and 20 mm for 1.5, 1.1, and 2.2 GeV, respectively.

4.2 Elastic ^{3}He and N_2 Cross Sections

The procedure to extract cross sections of ^{3}He and N_2 elastic scattering is the same as carbon. The reason we analyzed N_2 elastic cross section is to verify with a number of nucleus than ^{3}He that our analysis method worked. Beside this important check, the N_2 cross section is not used in the main analysis. However, applied analysis cuts will be different due to the extended length of ^{3}He and N_2 target cells. There will be no cut on the target length due to poorly reconstructed y_{tg}.

4.2.1 Simulated Cross Sections

The simulated cross section for an extended target is obtained by the following steps:

1. Simulate elastic ^{3}He or N_2 cross section with target length of 34.3 cm (specific target collimator configurations can be found in [6]). This is the total length of ice cone cell (see Section 2.7 and Fig. 2-11) with its windows positioned at 15.04 cm downstream and 19.25 cm upstream.

2. Generate with the MC elastic events for extended target with sieve slit and target collimators. Choose an optimal region in θ_{tg} versus ϕ_{tg} plane, analysis cuts are based on this region. These cuts will be used in experimental cross section extraction as well. The boundaries for these cuts are shown in Table 4.4.

   In the ^{12}C elastic analysis, we chose 2D cut on (θ_{tg} vs ϕ_{tg}) from selected sieve slit hole centers from experimental data. For the ^{3}He and the N_2 elastic analysis, we chose the optimal area that as large as possible and still cover enough events inside. This area is determined from simulation with extended target and sieve slit on configuration.

3. The rest is the same as step 2 through step 4 of the section discussing simulating the elastic cross section of the carbon analysis.

4.2.2 Experimental Cross Sections

The experimental cross section is obtained the same way as for the elastic carbon analysis:

1. We subtract the background (contributions from cell glass windows, two-step process and nitrogen gas inside ^{3}He) to obtain pure ^{3}He. There are three types of runs for one kinematic setting: empty cell (the reference cell with vacuum inside), reference run (the reference cell filled with nitrogen gas) and production

Energy	dp = -2 %		dp = 0 %		dp = 2 %	
	ϕ_{tg}	θ_{tg}	ϕ_{tg}	θ_{tg}	ϕ_{tg}	θ_{tg}
1.1 GeV	0.012291	0.044039	0.012683	0.045982	0.014483	0.048538
	0.005598	0.028701	0.009747	0.031564	0.015540	0.035245
	-0.002779	0.037188	-0.004306	0.035552	-0.006733	0.033252
	0.001253	0.050992	0.001018	0.047413	-0.000313	0.043272
1.5 GeV			0.012242	0.045219		
			0.009795	0.031545		
			-0.003938	0.035355		
			0.001086	0.046733		
2.2 GeV			0.013583	0.044397		
			0.010217	0.031207		
			-0.003288	0.035808		
			0.000470	0.046288		

Table 4.4: Boundaries in the reconstructed θ_{tg} (rad) and ϕ_{tg} (rad) for three beam energies. These boundaries are cuts applied on elastic extended target (^{3}He and N_2) analysis. For each setting, the four points from top to bottom correspond to sieve holes 2C, 2D, 1D, 1C, respectively.

run (^{3}He cell). At first, we subtract the empty cell run (after proper normalization) from nitrogen cell run, which gives the yield from pure nitrogen. Then we subtract this pure nitrogen yield from the production run after applying a scaling factor that accounts for the difference between nitrogen density inside the reference cell and the nitrogen density inside the ^{3}He cell.

2. The number of target ^{3}He is given by $N_{tg} = \rho_{^3He} \times L$ where $\rho = 7.9$ amg and $L = 34.3$ cm. There is no analysis cut on y_{tg} (there are hardware cuts provided by the target collimators [6]).

3. The rest is the same as steps 1 and 3 through 7 in extracting the experimental cross section from elastic carbon.

In Table 4.5, estimates of the systematic uncertainties on the unpolarized ^{3}He elastic cross sections are given. The uncertainty on the target density is from preliminary online result and will be improved with further study [63]. The uncertainty from the acceptance is from carbon elastic cross section results.

Source	Systematic Uncertainty
Target density	$< 5\%$
Carbon normalization uncertainty	8%
$\delta\sigma_{\text{exp}}/\sigma_{\text{exp}}$	10%

Table 4.5: Experimental ^{3}He unpolarized elastic cross section systematic uncertainty. Carbon normalization uncertainty come from the carbon elastic cross section study, $\approx 8\%$ disagreement between measured cross section and simulated cross section.

4.2.3 N_2 and ^{3}He Cross Section Results

Cross section results for ^{3}He and N_2 targets for the three beam energies are shown in Table 4.6 and Table 4.7. The results agree within their uncertainties. These results on two different nuclei and different beam energies and HRS central momentum, combined with elastic carbon results, give us the confidence that our transport matrix and the cross section extraction method based on focal plane plane and target plane variables works well for both foil and extended length targets. The disagreement between experimental and simulated ^{12}C elastic cross section is possibly caused by sources such as: the imperfect transport function, the assumption of angular, momentum and y_{tg} acceptances are 100% within the analysis cut.

Energy / DP	^{3}He Run Number	σ_{sim} (nb/sr)	$\sigma_{experimental}$ (nb/sr)	%
1.1 GeV				
Dp = -2%	1913	188222	170084	10
Dp = 0%	1904	185285	184956	1
Dp = 2%	1897	190517	200949	-5
1.5 GeV				
Dp = 0%	1609	76864	75289	2
2.2 GeV				
Dp = 0%	2087	10147	10314	-2

Table 4.6: Comparison of simulated and experimental cross sections for elastic scattering off ^{3}He. At high energy, quasi-elastic contribution can't be neglected and an 8% correction is applied to the 2.2 GeV cross section result.

Energy / DP	N_2 Run	σ_{sim} (μb/sr)	$\sigma_{experimental}$ (μb/sr)	%
1.1 GeV				
Dp = 0%	1903	1416	1465	-3
Dp = 2%	1894	1455	1544	-6
1.5 GeV				
Dp = 0%	1608	414.5	412.6	1
2.2 GeV				
Dp = 0%	2082	17.247	16.801	3

Table 4.7: Comparison of simulated and experimental cross sections for elastic scattering off N_2 target.

4.3 Elastic ^{3}He Asymmetry

Elastic scattering asymmetry results for the first period were extracted with the target polarized longitudinally (either 0° or 180° with respect to the beamline). There are three beam energy settings: 1.1, 1.5, and 2.2 GeV. A cut on ν as shown in the fourth column in Table 4.8 was used to select elastic peak. Quasi-elastic dilution is not corrected but the contribution should be small. These results are shown in Table 4.8, and Fig 4-3 and Fig 4-4. Each data point is the average of all runs for that particular setting of beam energy, target spin direction and beam IHWP status.

Run	$A_{simulation}$	$A_{data} \pm (stat) \pm (syst)$	ν cut (MeV)
1904	0.007040	0.012177 ± 0.002383 ± 0.001461	$\leq$ 10
1906	-0.007040	-0.010379 ± 0.002453 ± 0.001245	$\leq$ 10
1610	0.009378	0.009761 ± 0.001542 ± 0.001171	$\leq$ 10
1620	-0.009378	-0.012681 ± 0.001549 ± 0.001522	$\leq$ 10
1625	0.009378	0.008496 ± 0.001696 ± 0.001020	$\leq$ 10
1634	-0.009378	-0.009138 ± 0.001892 ± 0.001097	$\leq$ 10
2086	0.013434	0.018370 ± 0.004189 ± 0.002204	$\leq$ 20
2092	-0.013434	-0.007325 ±0.004397± 0.000879	$\leq$ 20
2096	0.013434	0.022969 ± 0.006264± 0.002756	$\leq$ 20
2099	-0.013434	-0.010613± 0.005998 ± 0.001274	$\leq$ 20

Table 4.8: Elastic ^{3}He asymmetry for three beam energies.

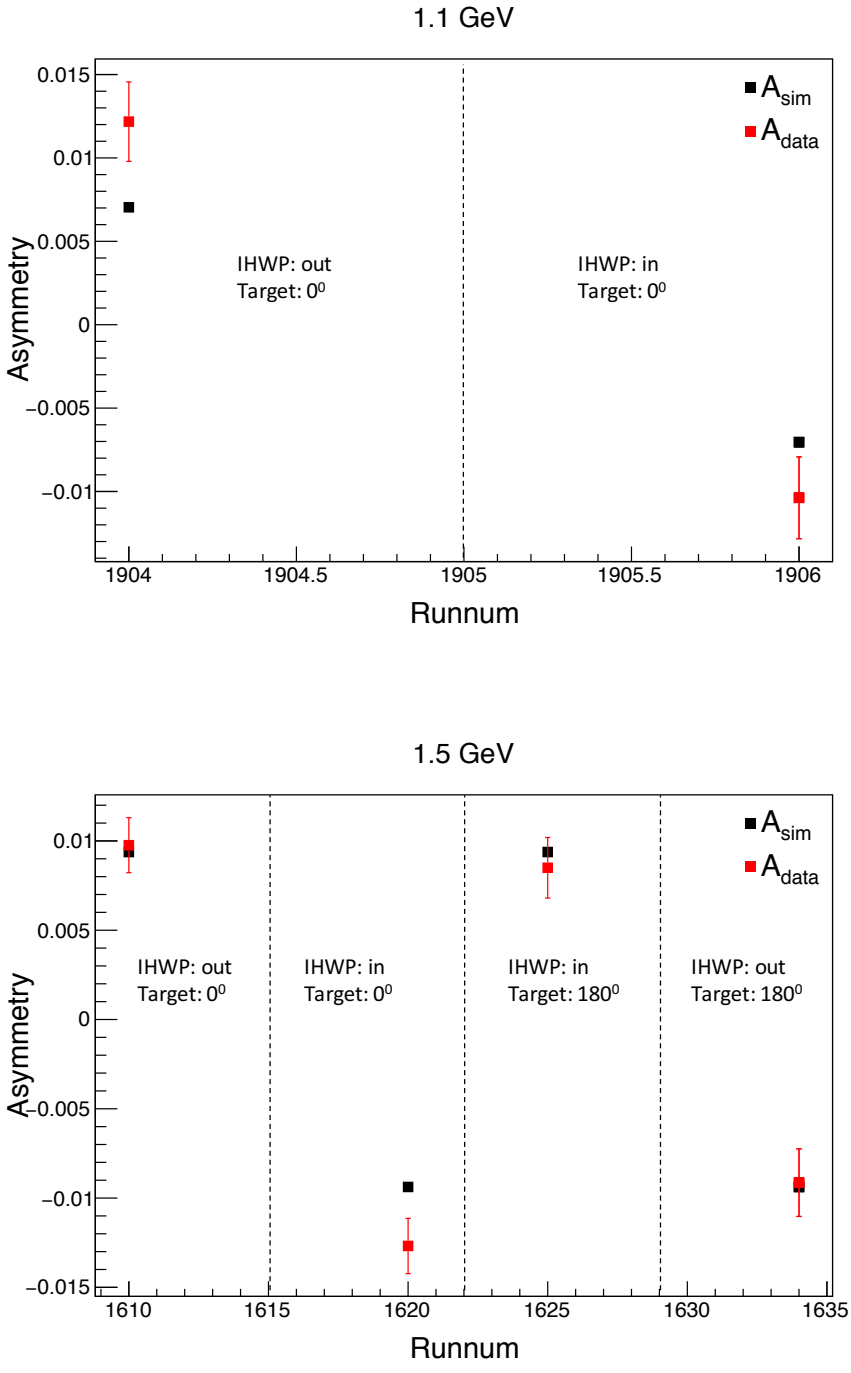

Figure 4-3: Elastic longitudinal asymmetry for 1.1 and 1.5 GeV. Error bars are statistical uncertainties. Red squares are experimental asymmetry, black squares are simulated asymmetry.

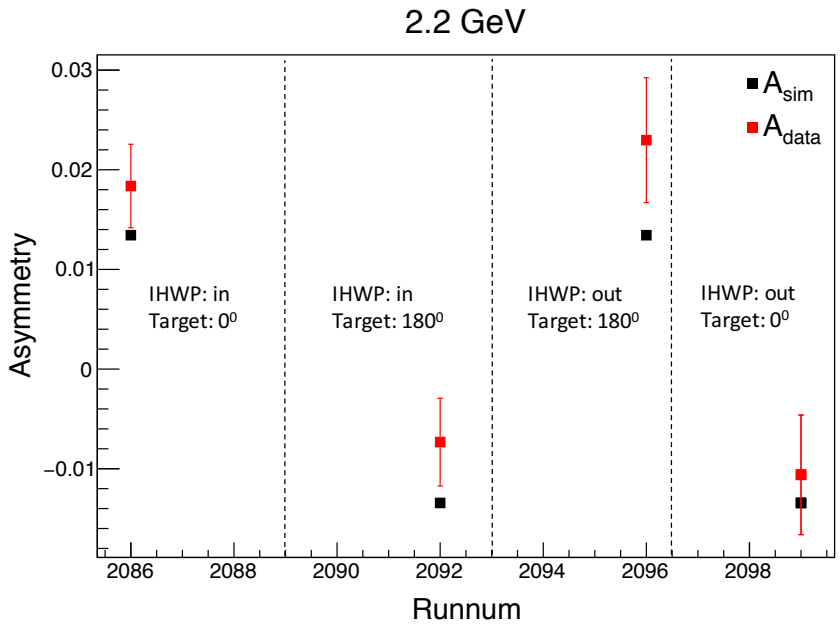

Figure 4-4: Elastic longitudinal asymmetry for 2.2 GeV. Error bars are statistical uncertainties. Red squares are experimental asymmetry, black squares are simulated asymmetry.

Chapter 5

Production Data Analysis, Results and Conclusions

To fulfill the physics goal of experiment E97110, asymmetries and cross sections were measured for polarized inelastic electron scattering from polarized ^{3}He. In this chapter the analysis of these data, preliminary results for inelastic ^{3}He asymmetries, unpolarized cross sections and polarized cross sections are presented. The only input to these results that is not final is the target polarimetry, and radiative corrections. Once the polarimetry is final, cross section results presented here will be updated and be used to form the GDH and other moments. During the run of E97-110, it was clear that the defective septum would complicate the analysis and restrict significantly the statistical precision of the data, since only a small area of the acceptance could be used. Hence it was decided for the first period to only measure moments with enough statistical precision. The g_1, g_2 and σ_{TT} measurement presented here were not intended to be precisely measured.

5.1 Detector Efficiencies

For cross section analysis, efficiencies of detectors must be well controlled. Since this work is generic, it will be applied not only to the elastic analysis but also to the production analysis. In efficiency studies, detector cuts are optimized such that one

can distinguish good electrons from background events. These background events mostly come from negative charged pions and low-energy electrons. The detector cuts involve VDCs, scintillators, Cherenkov and the total shower calorimeter. Since detector efficiencies are in principle helicity independent, they should not affect the asymmetry analysis.

5.1.1 VDC Efficiency

The VDC efficiency is defined as [57]:

$$\epsilon = \frac{N_{good}}{N_{tot}}, \tag{5.1}$$

where N_{tot} is the total number of events that survive the acceptance and PID cuts (sample events), and N_{good} is the number of events with a successful track reconstruction that is verified its consistency with the lead glass calorimeter signal location. PID cuts used here in N_{tot} are the combination of Cherenkov and lead glass cuts and do not contain any tracking information.

For the analysis, only events from main trigger (T1 events see the next section) are kept. For E97110, the total rate was typically between 4 kHz and 250 kHz, which resulted for the latter in a large number of events having multiple tracks for some kinematics. This occurred especially for elastic and quasi-elastic kinematics as well as for nitrogen data (a small amount of nitrogen was added to ^{3}He target, see Chapter 6), and has to be corrected due to detector inefficiency in counting good electrons at high rates. The VDC multi-track efficiency for E97110 was done by J. Liu [57]. Fig. 5-1 shows the VDC efficiency correction applied to both cross section and asymmetry analyses.

5.1.2 Scintillator Efficiency

The Right HRS contains two plastic scintillator planes (S1 and S2) separated by 2 m. They trigger the data acquisition [6]. Two trigger types, T_1 and T_2, were used during the experiment. T_1 is formed if there are signals in both S_1 and S_2 and if

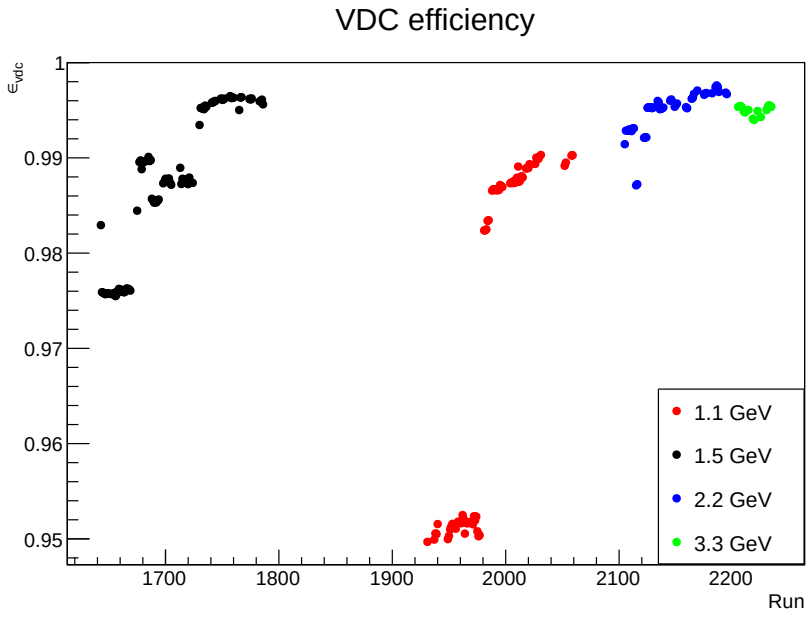

Figure 5-1: RHRS VDC efficiency vs run number for first period. Different colors represent different beam energies. Here only ^{3}He target runs are plotted. The first several data points for each energy are quasi-elastic runs, which high rates explain their lower VDC efficiency. Elastic runs are not listed.

the particle trajectory has a very small angle with respect to the central ray of the spectrometer. T_2 is formed if there are signals either in both S_1 and Čerenkov but not S_2, or in both S_2 and Čerenkov but not S_1. The T_2 type is often from either cosmic ray events, or particles rescattered off the edge of the acceptance. Only main trigger events T_1 are used in the analysis, whereas secondary triggers T_2 are used to determine the trigger efficiency. The trigger or scintillator efficiency is given by

$$\epsilon_{trig} = \frac{T_1}{T_1 + T_2}. \tag{5.2}$$

In most case, the scintillator efficiency is greater than 99% as shown in Fig. 5-2 and excluding the T_2 events has a negligible impact. However, there are two run with low trigger efficiency: run 1923 and run 1930 which have efficiencies close to 98%. There were about twenty other runs which exhibits similar efficiency, see Table 5.1. All runs are in the quasi-elastic region (momentum setting $DP = 10\%$) and the higher quasi-elastic rate, explains the lower the trigger efficiency.

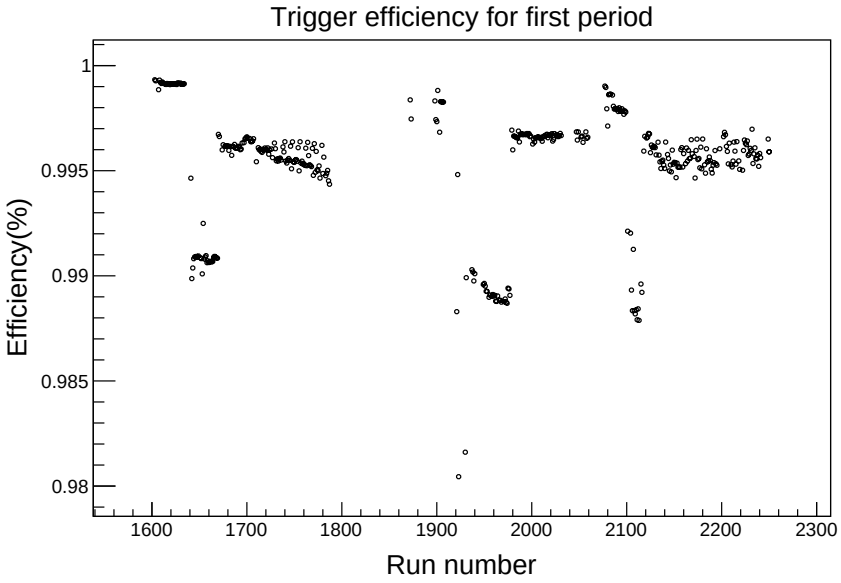

Figure 5-2: Scintillator (or T_1 trigger) efficiency vs run number for the first period data.

Runs	Beam energy (GeV)	P_0 (GeV)	DP (%)
1921, 1923, 1930, 1931, 1939, 1949-1953, 1955, 1956, 1958-1964, 1966-1968	1.148	1.068	10
1642	1.542	1.418	9
2105, 2106, 2108-2113, 2115, 2116	2.237	2.071	8

Table 5.1: List of runs with $\epsilon_{trig} < 98\%$. All are quasi-elastic runs with high rate and thus lower efficiency.

5.1.3 Charge Asymmetry

Each production run is different in conditions such as charge asymmetry, liveime, etc. The beam charge asymmetry is due to a difference between the helicities H+ and H- gated beam charges Q^+ and Q^-, where Q^+ and Q^- are the accumulated charges for $+$ and $-$ helicity states, respectively.

After applying the corresponding charge and livetime corrections to our measured asymmetries, we can obtain physics asymmetries which should be independent from charge and livetime asymmetries. The charge asymmetry is defined as

$$A_Q = \frac{Q^+ - Q^-}{Q^+ + Q^-}, \tag{5.3}$$

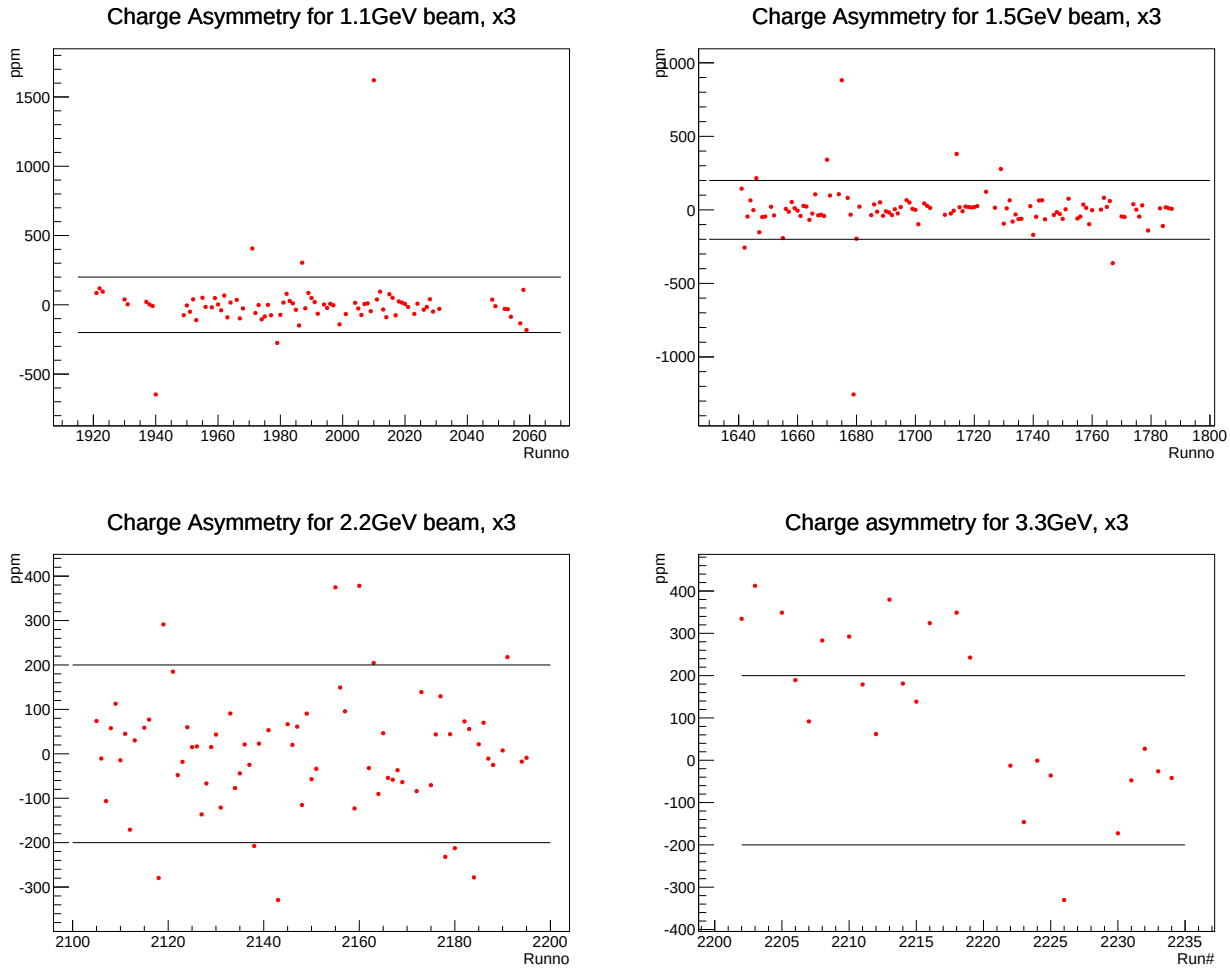

Figure 5-3: Charge asymmetry for first period, calculated using the $\times 3$ gain BCM-scalers. Each panel corresponds to a different beam energies.

The charge asymmetry for production runs on polarized ^{3}He is shown in Fig 5-3. Most of the time, the charge asymmetry is small, within 200 ppm [58]. For some runs, however, beam trips create a large A_Q.

5.1.4 Livetime Correction

A large livetime (1 - deadtime) asymmetry can be caused by a large physics asymmetry, a large charge asymmetry, high deadtime or/and a high DAQ rate. Usually, the deadtime should be kept below 20% and the DAQ rate around 4kHz (these conditions are for the 6 GeV DAQ setup used for E97-110). The livetime asymmetry is calculated as the following:

$$A_{LT} = \frac{\frac{N^+_{acc}}{N^+} - \frac{N^-_{acc}}{N^-}}{\frac{N^+_{acc}}{N^+} + \frac{N^-_{acc}}{N^-}}, \tag{5.4}$$

where N_{acc} is the number of accepted triggers for each helicity, and N is the number of total triggers for each helicity. Fig. 5-4 shows livetime asymmetries for four beam energies. In this analysis, both N_{acc} and N are from the T_1 trigger.

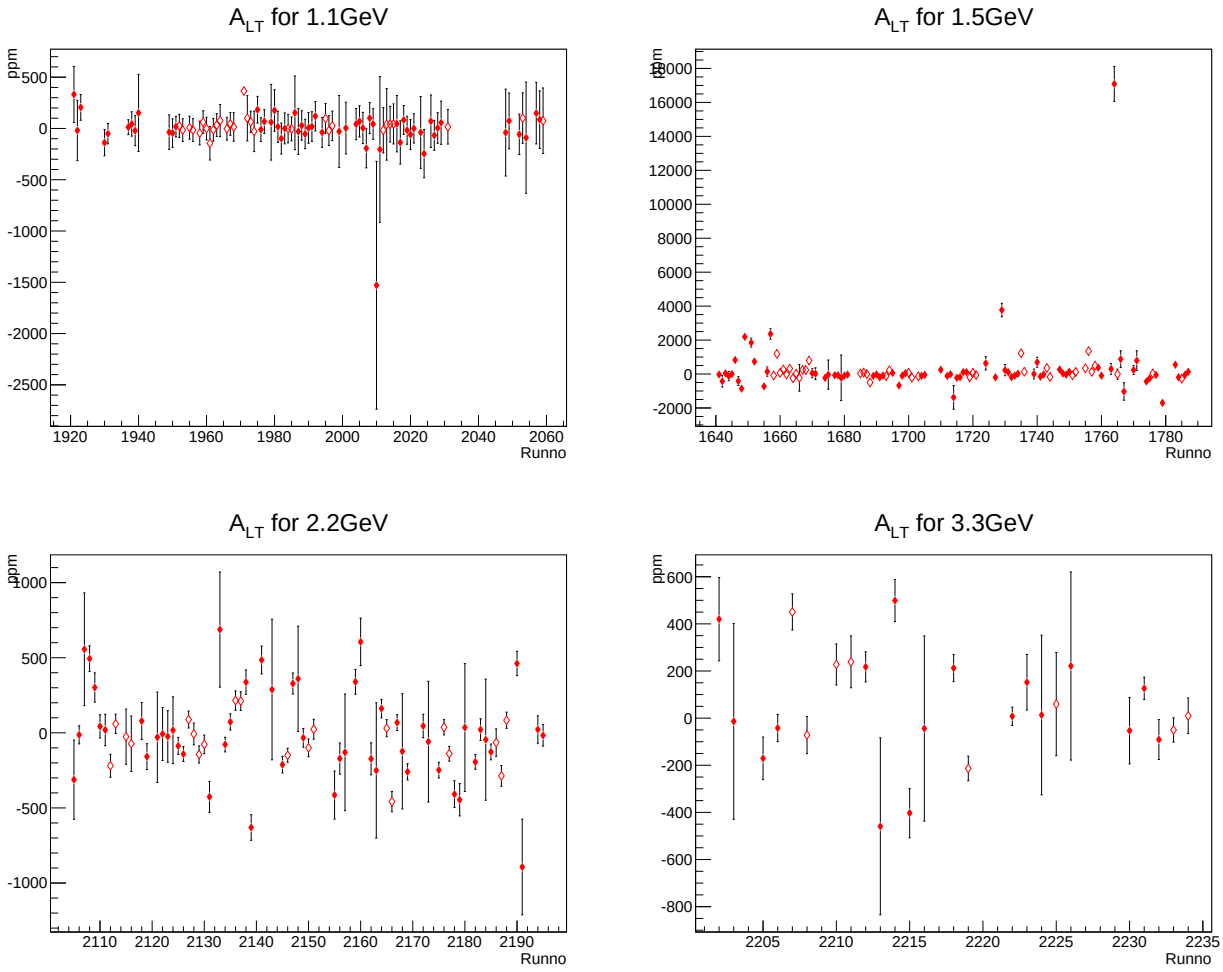

Figure 5-4: Livetime asymmetry for the first E97110 run period with different beam energies. The solid diamonds are for runs in which the target and beam polarizations are parallel to each other. Open diamonds are for the perpendicular case.

5.1.5 Dilutions

In the following section, I will discussed dilution analysis which is relevant only for ^{3}He runs (except for cross section difference analysis), but not for carbon analysis.

Ideally the experiment yield is contributed purely from the electron scattering off the ^{3}He target. However, contaminations from the nitrogen gas and the glass cell walls cannot be simply separated from the reaction channel of interest, i.e. the inclusive scattering of $^3\vec{\text{He}}(\vec{e}, e')$. The raw asymmetries measured in the experiment can be expressed as:

$$A_{raw} = \frac{1}{2}\frac{\Delta Y(^3\text{He}) + \Delta Y(\text{N}_2) + \Delta Y(\text{glass})}{Y(^3\text{He}) + Y(\text{N}_2) + Y(\text{glass})}, \tag{5.5}$$

with $\Delta Y = Y^+ - Y^-$ and $Y = \frac{Y^+ + Y^-}{2}$ where $Y^\pm$ are yield with $\pm$ helicity from different materials in the experimental runs. The unpolarized yield difference $\Delta Y(\text{N}_2) = 0$ and $\Delta Y(\text{glass}) = 0$, so these contaminations only dilute the real asymmetry value rather than adding unwanted asymmetry. Therefore, a dilution factor is introduced to correct this effect.

Nitrogen dilution for the elastic reaction

To estimate the dilution caused by the $\approx$1% unpolarized N_2 mixed in the ^{3}He cell, data were taken on a reference cell filled with N_2. The N_2 dilution factor f_{N_2} [67] is given by:

$$1 - f_{N_2} = \frac{Y_{N_2}}{Y_{^3He}} = \frac{\sigma_{N_2}}{\sigma_{^3He}}\frac{n_{N_2}}{n_{^3He}}, \tag{5.6}$$

where Y_{N_2} ($Y_{^3He}$) is the N_2 (^{3}He) yield[1], $\sigma_{^3He}$ is the ^{3}He cross section from the polarized ^{3}He cell data, σ_{N_2} is the N_2 cross section from reference cell N_2 data, and n_{N_2} ($n_{^3He}$) is the N_2 (^{3}He) density inside the polarized ^{3}He cell under running conditions. Since temperature affects both N_2 and ^{3}He densities of the cell in the same way, one can use fill density measurement results for ^{3}He (performed at room temperature) and the N_2 fill density measured when the cell was filled (also given at room temperature). The cross sections $\sigma_{^3He}$ and σ_{N_2} are obtained from data with exactly the same acceptance, cut in $W_{^3He}$ (the invariant mass calculated from Eq. 1.3 using $M = M_{^3He}$), and PID cuts.

[1] Yield $= \frac{PS_1 \times N}{LT \times Q \times \epsilon}$, where PS_1 is the prescaler factor for trigger T_1, N is number of event, LT is livetime, Q is charge, ϵ is the total efficiency.

Runs	psig	atm	σ_N^{MC} (nb)	$\text{Yield}_{\text{cor}}$
2081	29	2.973	17519	650.55
2082	73	5.967	17114	1234.58
2083	110	8.485	16753	1767.52
2085	147	11.003	16437	2284.16

Table 5.2: List of nitrogen runs for pressure curve study. The reference cell was filled with nitrogen at different pressures. The second and third columns are pressure at different unit. The fourth column is simulated nitrogen cross section. And the last column is the corrected nitrogen yield.

There are two methods to determine n_{N_2} from elastic data. The first method compares the N_2 elastic peaks measured from the reference cell and the polarized target cell. The second method uses reference cell runs in which the pressure of the nitrogen filling the reference cell was varied and that provide the N_2 pressure versus its yields [59]. This so-called pressure curve and the nitrogen elastic peak in the polarized target cell to determine n_{N_2}. Using the pressure curve, it was determined that the N_2 pressure in cell Proteus is 0.122 atm at 320 K, shown in Fig 5-5, which is equivalent to $n_{N_2} = 0.104 \pm 0.002$ amg[2] at 273 K. The filling density of Proteus is 0.0914 amg. The two results differ by 15%, which agree within the fit uncertainty, the statistic uncertainty, and the pressure uncertainty.

Table 5.2 shows list of runs and filled pressure for each run.

Nitrogen dilution for inelastic kinematics

The inelastic N_2 dilution factor is defined as:

$$f_{N_2} = 1 - \frac{Y_{N_2} - Y_{empty}}{Y_{^3He} - Y_{empty}} \times \frac{n_{pol}}{n_{ref}} \tag{5.7}$$

where Y_{N_2}, Y_{empty}, and $Y_{^3He}$ are yields from the nitrogen reference cell, empty cell and polarized ^{3}He cells respectively. The nitrogen densities in the polarized ^{3}He cell, and reference cell are given by n_{pol} and n_{ref}. The use of empty cell eliminates the contribution from cell glass windows.

[2]An amagat is a practical unit of number density. It is defined as the number of ideal gas molecules per unit volume at 1 atm and 0°.

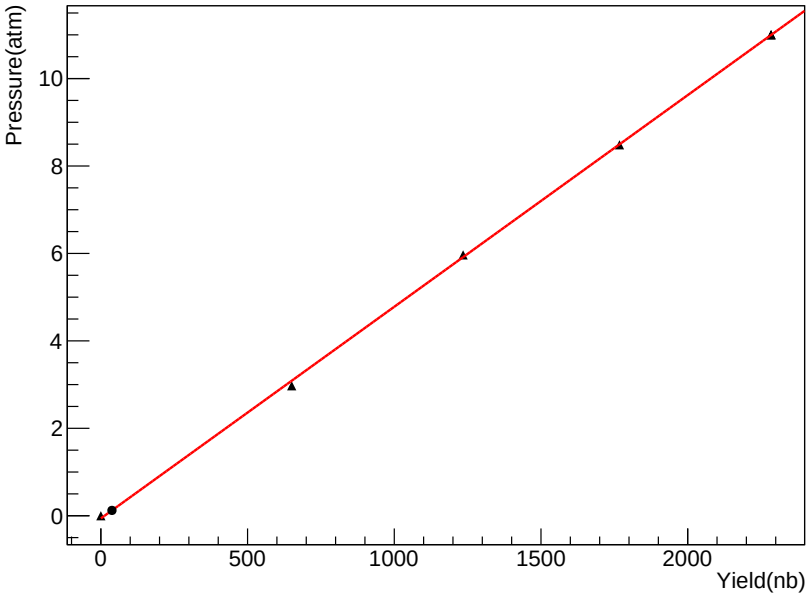

Figure 5-5: N_2 pressure curve. The triangle data are results from the nitrogen reference cell filled at different pressures. The circle data is the N_2 elastic yield from cell Proteus at 320 K. Each data point has an uncertainty in pressure of 0.1 atm, which can be significant for low pressure runs. The pressure is molecule pressure. The red line is a fit through the triangle data, $P(atm) = (0.004841 \pm 4.9 \times 10^{-5})Yield + (-0.06088 \pm 0.07805)$.

Fig. 5-6 shows the nitrogen dilution factors for the four beam energies at 6°. The dilution factors were found to be between 0.45 and 0.91. This result depends on cuts, and because we will use dilution factor in asymmetry, so the cuts are the same as asymmetry cuts.

Since collimators were used to remove the target windows from the acceptance, the dilution from the glass contamination should be small. However, due to a two step process[3], the contamination from the glass actually increases significantly with decreasing spectrometer momenta. The dilution factor from the glass is defined as follows:

$$f_{glass} = 1 - \frac{Y_{empty}}{Y_{^3He} - (Y_{N_2} - Y_{empty})\frac{n_{pol}}{n_{ref}}}. \tag{5.8}$$

[3]Electron from the primary beam scatter off the beryllium entrance window then rescatters off the glass wall of the target cell [60].

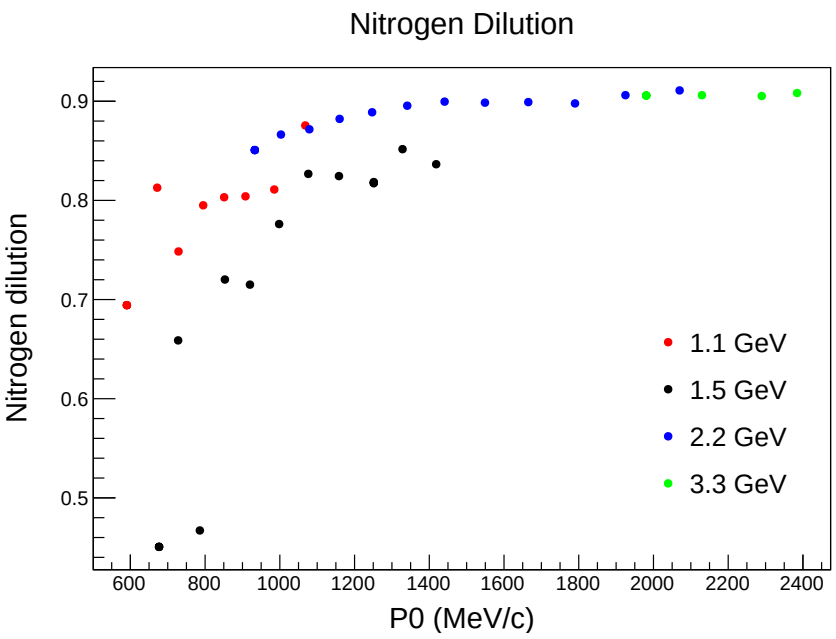

Figure 5-6: Nitrogen dilution factors for the first period.

Fig. 5-7 shows the contamination from the glass.

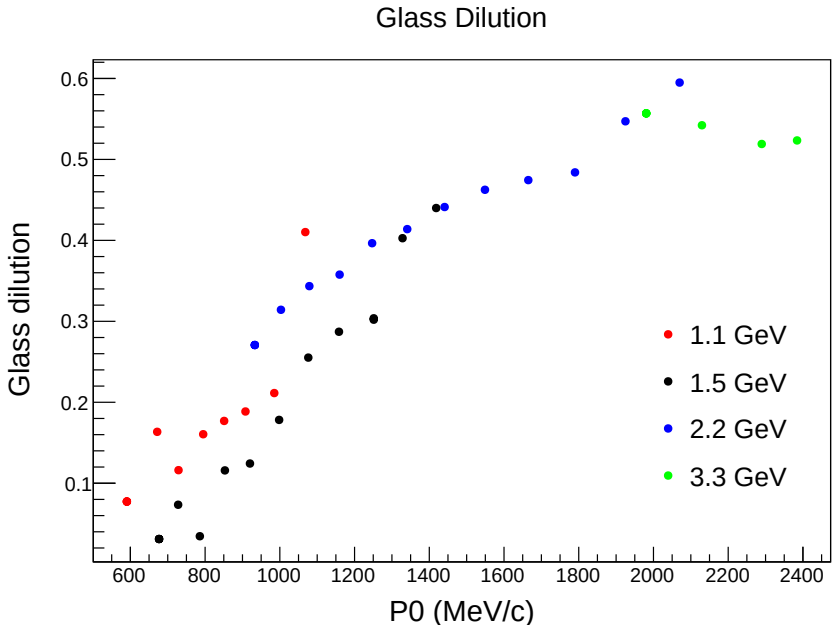

Figure 5-7: Glass dilution factors for the first period.

5.2 Asymmetry Results

5.2.1 Extraction of Experimental Asymmetry

The longitudinal and transverse physics asymmetries are defined by taking the ratio of the difference in polarized cross sections to their sum:

$$A_{\parallel} = \frac{\frac{d^2\sigma^{\downarrow\Uparrow}}{dE'd\Omega} - \frac{d^2\sigma^{\uparrow\Uparrow}}{dE'd\Omega}}{\frac{d^2\sigma^{\downarrow\Uparrow}}{dE'd\Omega} + \frac{d^2\sigma^{\uparrow\Uparrow}}{dE'd\Omega}}, \tag{5.9}$$

and

$$A_{\perp} = \frac{\frac{d^2\sigma^{\downarrow\Rightarrow}}{dE'd\Omega} - \frac{d^2\sigma^{\uparrow\Rightarrow}}{dE'd\Omega}}{\frac{d^2\sigma^{\downarrow\Rightarrow}}{dE'd\Omega} + \frac{d^2\sigma^{\uparrow\Rightarrow}}{dE'd\Omega}}, \tag{5.10}$$

where $\uparrow$ and $\downarrow$ refer to the electron spin, pointing either parallel or anti-parallel to the beamline, and $\Uparrow$ designates that the target is polarized along the electron beam direction. For the transverse $A_{\perp}$ case, $\Rightarrow$ indicates that the target is polarized perpendicular to the beamline.

From data the raw asymmetries are calculated from the number of events within the chosen acceptance and detector cuts:

$$A_{raw} = \frac{\frac{N^+}{LT^+Q^+} - \frac{N^-}{LT^-Q^-}}{\frac{N^+}{LT^+Q^+} + \frac{N^-}{LT^-Q^-}}, \tag{5.11}$$

where $N^{\pm}$, $Q^{\pm}$, and $LT^{\pm}$ are the number of accepted events, the total charge and the correction for the computer deadtime. The $\pm$ refers to the electron beam helicity.

The physics asymmetries are then calculated from the raw experimental asymmetries using:

$$A^{exp}_{\parallel,\perp} = \pm\frac{A^{raw}_{\parallel,\perp}}{f P_t P_b}, \tag{5.12}$$

where f is the dilution factor (see Section 5.1.5), and P_b and P_t are the beam and target polarizations, respectively. The sign on the right hand side of Eq. 5.12 depends on the configuration of the insertable beam half-wave plate (IHWP) and the target spin direction.

5.2.2 Asymmetry Sign Convention

The sign on the right hand side of Eq. 5.11 depends on the configuration of the IHWP and the target spin direction. The status of the IHWP is either 'IN' if it is inserted or 'OUT' if not. For each polarized ^{3}He run, the sign should be multiplied by -1 if the IHWP is 'OUT', and +1 if IHWP is 'IN' for 2.2 and 3.3 GeV, and opposite for 1.1 and 1.5 GeV. The target polarization sign depends on the direction that the target spin is pointing. With the ^{3}He target setup, in particular that of laser system, there are four possible target orientations: 0°, 90°, 180° and 270°. For experiment E97110, the 90° configuration was not used because its configuration entails lower polarization. Hence, we obtain the following sign convention for target polarization [6]:

- 0°: longitudinal field points toward the Hall A beam dump, target spin = -1.
- 180°: longitudinal field points toward the Møller polarimeter, target spin = +1.
- 270°: transverse field points toward L-HRS, target spin = +1.

For example, for longitudinal configuration, the sign on the R-HRS of Eq 5.12 is the product of the sign of the beam IHWP and the target polarization. $sign = +1$ if (IHWP, target) = (OUT, 0°) or (IN, 180°) and $sign = -1$ if (IHWP, target) = (IN, 0°) or (OUT, 180°).

5.2.3 Inelastic ^{3}He Asymmetry Results

Results for the physics asymmetry without radiative corrections are shown in Figure 5-8 versus the invariant mass W[4]. The parallel configuration is represented with red squares and the perpendicular with black squares. The error bars are statistical. The quasi-elastic region is located around $W = 938$ MeV since M_N was used in Eq. 1.3. As W approaches the $\Delta(1232)$ region, both asymmetries cross over zero near the pion production threshold. As mentioned in the introduction of this chapter, because only a small part of scattered electrons could make to the detector plane due

[4]Here, W is defined in terms of the nucleon mass using Eq 1.3

to the mis-wired septum, the statistic errors are large. In addition, after acceptance cuts the number of electrons survived become smaller. Moreover, a large contribution from the two step process dominates the background for large W, which contributes to dilution. Figure 5-9 shows a comparison of parallel asymmetries at 2.2 GeV beam energy between the first and second periods. As one can see, statistic uncertainties from the second period are much better.

Source	Systematic Uncertainty
Target polarization	10%
Beam polarization	4 %
Dilution	$< 10\%$
Pion rejection	$< 1\%$
$\delta A_{\rm exp}/A$	12%

Table 5.3: ^{3}He asymmetry systematic uncertainty. The target polarization uncertainty is preliminary from online result and will be improved with further study. Beam polarization uncertainty was given in Sec 2.3. Dilution uncertainty is less than 10%, fortunately, we will use a different method to extract cross section difference which does not have dilution factor.

In Table 5.3, the systematic uncertainty on the asymmetry is given. The uncertainty on the target polarization is preliminary from online result and will be improved with further study [63]. Beam polarization uncertainty is estimated to be about 4% [6].

5.3 Unpolarized Cross Sections

Extraction of the elastic cross section is given by Eq. 4.1. Extraction of the inelastic unpolarized raw cross section is similar except that there is a E' dependence:

$$\frac{d\sigma_0^{raw}}{d\Omega dE'} = \frac{N_{raw}}{N_{tg}} \times \frac{PS_1}{LT \times Q/q \times \epsilon} \times \frac{RC \times Acc}{\Delta\Omega_{geo}\Delta E'}, \tag{5.13}$$

where $N_{tg} = \rho\Delta Z$ (ρ is the target density, ΔZ is the target length), $\Delta E'$ is the momentum bite for each spectrometer setting.

The ^{3}He cross section is determined by subtracting the nitrogen contribution:

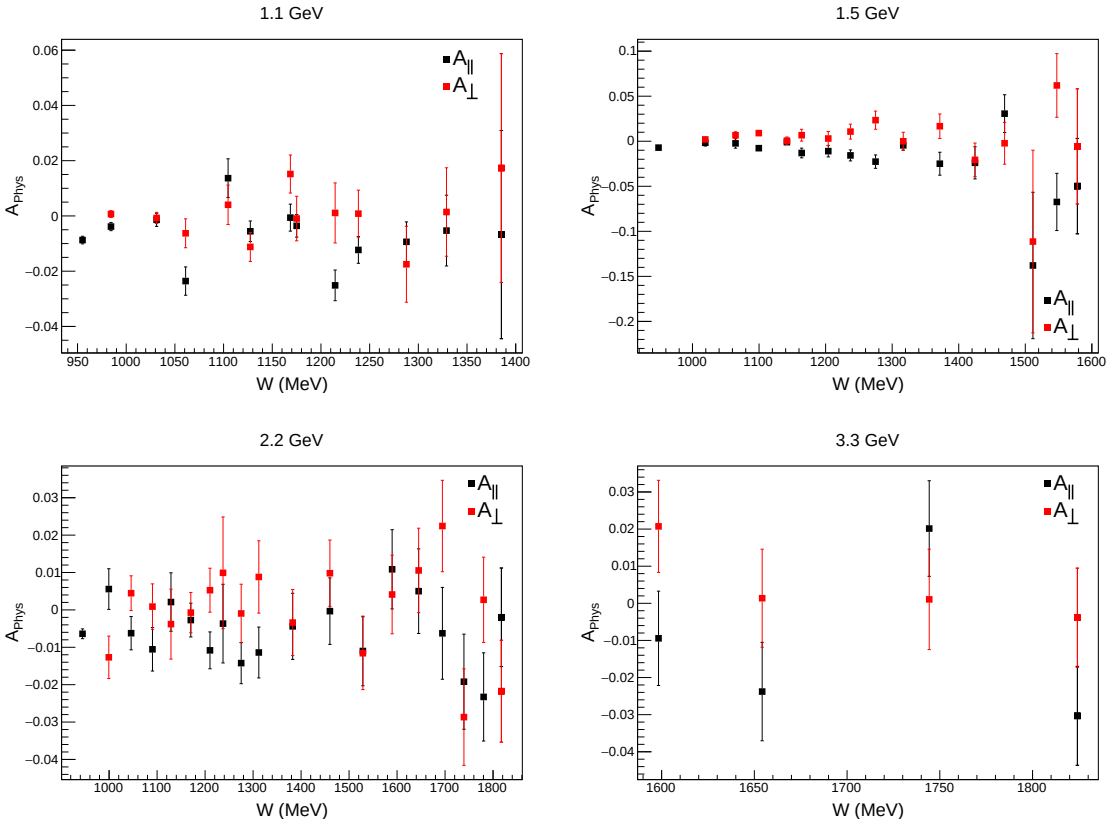

Figure 5-8: Inelastic asymmetries for four beam energies at 6°, extracted using Eq. 5.12. These asymmetries are not corrected for radiation effect yet. Error bars are statistical only.

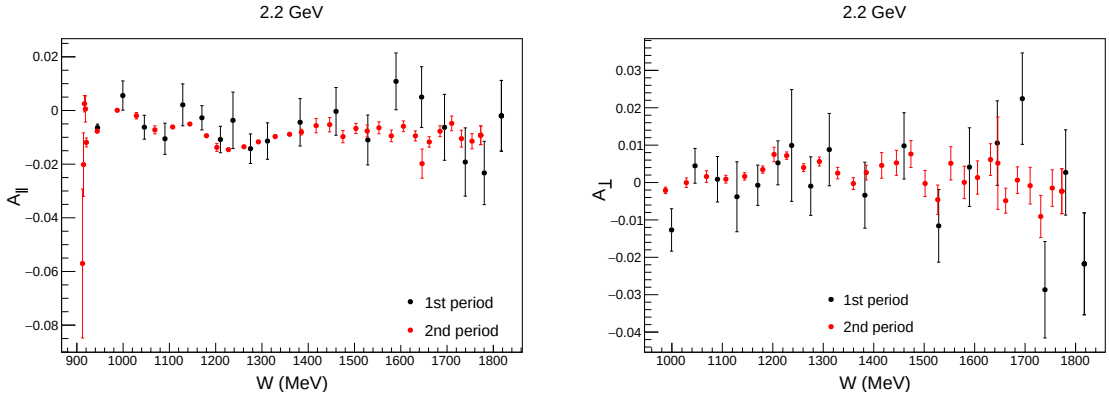

Figure 5-9: Inelastic asymmetry comparison between first (black circles) and second periods (red circles). Data from second period were taken with 2.135 GeV while for first period it was 2.2 GeV at 6°. The statistics from second period is much better than first period for which precision was intended for moments (W-integrated) only. Here both data have not been corrected for radiation effects yet.

$$\frac{d\sigma^{exp}_{0,^3He}}{d\Omega dE'} = \frac{d\sigma^{raw}_0}{d\Omega dE'} - \frac{\rho_N}{\rho_N + \rho_{He}} \frac{d\sigma_N}{d\Omega dE'}, \tag{5.14}$$

where ρ_N and ρ_{He} are the atomic densities of nitrogen and ^{3}He, respectively, inside the polarized cell, and σ_N is the nitrogen cross section.

The extraction of inelastic cross sections differs from that of the elastic case in several ways:

- Inelastic analysis results are not compared to the simulation as in elastic analysis because no reliable polarized inelastic event generator is available in the M.C.

- The target length ΔZ: As mentioned in Section 4.2, a target length of 34.3 cm is used for elastic analysis. In elastic simulation, we simulated an extended target length of 34.3 cm, and the events that pass the collimators are the events that should be compared with detected events. However, for inelastic analysis since there is no simulation that accounts for the collimation, we should use the actual target length seen by the spectrometer. A target length of 9.15 cm is used for inelastic cross section. This number is obtained by running the M.C. simulation with phase space selected for event generation and with same number of events for one setting without target collimator and the other with target collimator. Comparing the two numbers of events that arrives at the HRS provides the 9.15 cm determination.

- Geometry solid angle $\Delta\Omega_{geo}$ is obtained from simulation (phase-space setting).

- The acceptance cuts used are the same as that of the elastic analysis. They include focal plane acceptance cuts (a 2D cut on ϕ_{fp} vs y_{fp} plane) and reconstructed angles cuts (a 2D cut on θ_{tg} vs ϕ_{tg} plane). However, we do not apply invariant mass cut here.

Figs. 5-10 and 5-11 show the unpolarized cross section versus W for the four incident beam energies without radiative corrections. The unpolarized cross sections presented show slight discontinuities between momentum settings which is the effect of small momentum acceptance. Overall, the four spectra looks reasonable, at 2.2

GeV we can see the $\Delta(1232)$ resonance around $W = 1232$ MeV, at lower energy, the peak is not that clear.

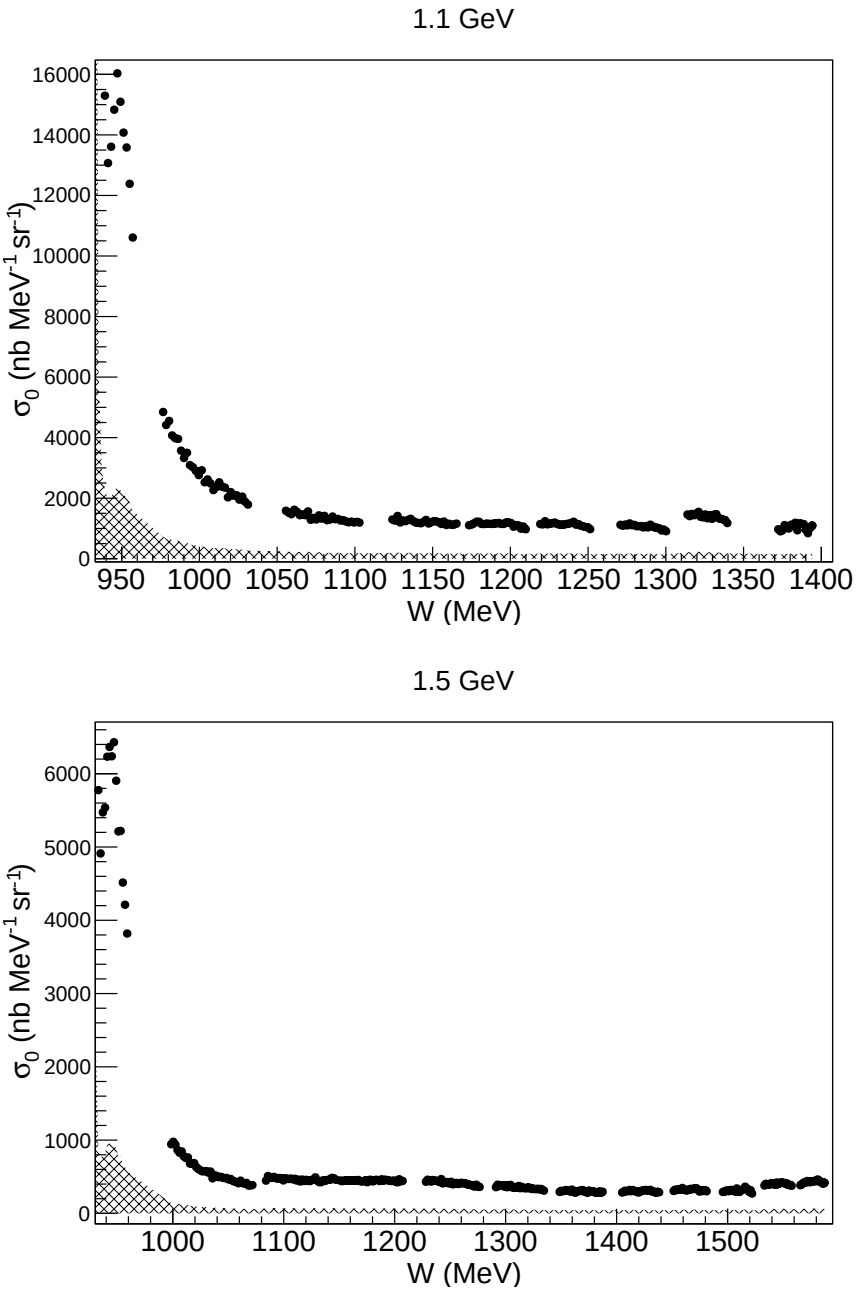

Figure 5-10: Preliminary unpolarized cross sections for incident beam energies of 1.1 GeV (top) and 1.5 GeV (bottom) without radiative corrections. The horizontal bands show the systematic uncertainty. Statistic uncertainties are small and not visible in the plot.

Fig. 5-12 shows a comparison of unpolarized cross sections between first and

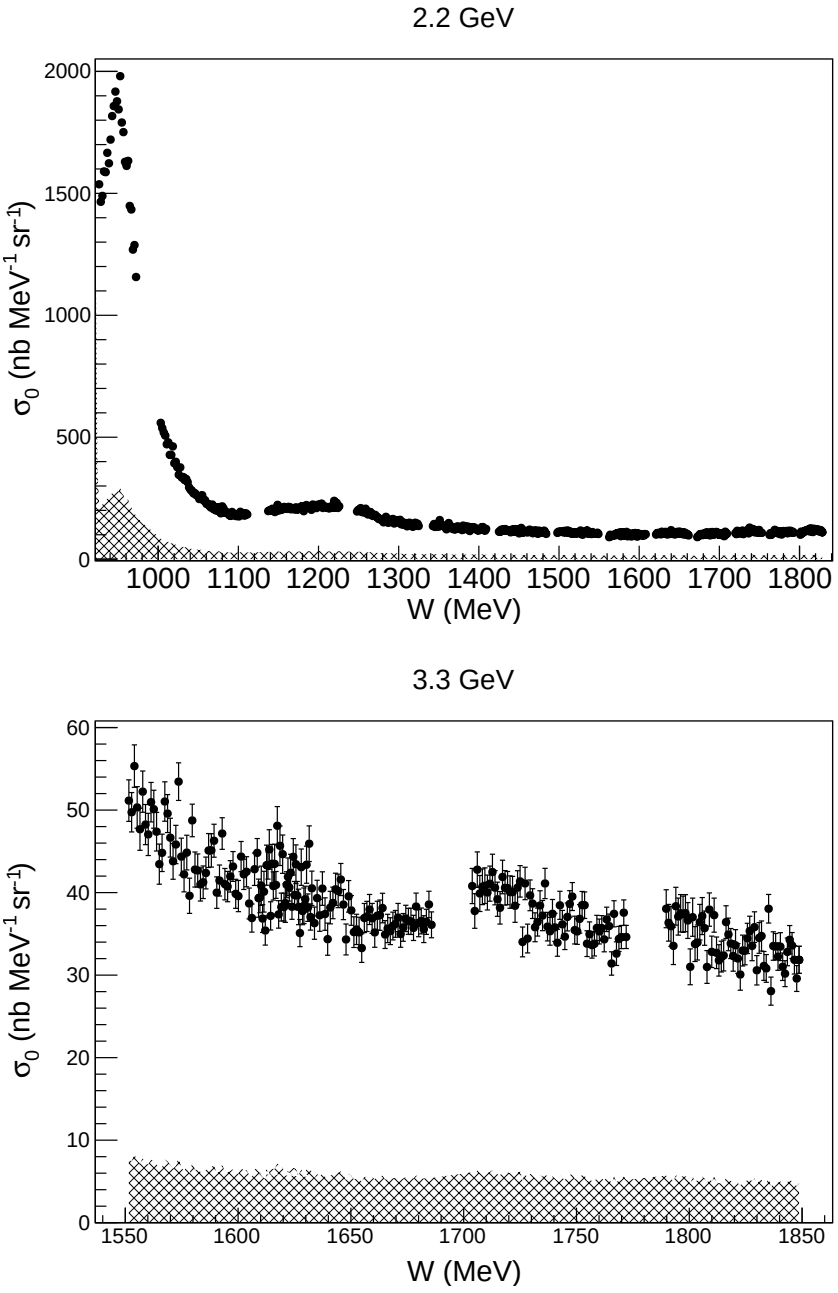

Figure 5-11: Preliminary unpolarized cross sections for incident beam energies of 2.2 GeV (top) and 3.3 GeV (bottom) without radiative corrections. The horizontal bands show systematic uncertainty. For 2.2 GeV statistic uncertainties are small and not visible in the plot.

second periods. For an accurate comparison, data from the second period are obtained by interpolating (linearly) between the 2.1 GeV and 2.8 GeV data from second period to match the 2.2 GeV energy of first period data.

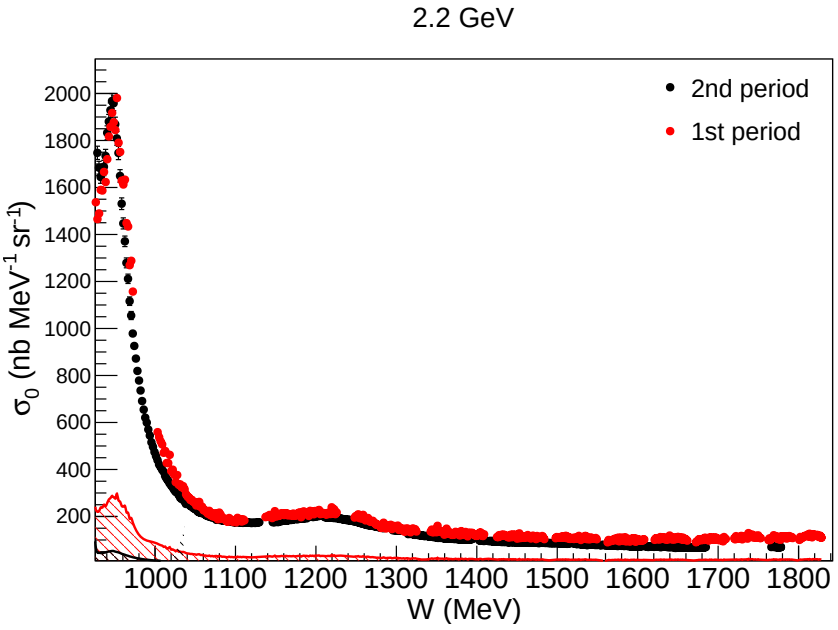

Figure 5-12: Unpolarized cross section comparison between first and second periods. For beam energy $E_{beam} = 2.2$ GeV at 6°. The black circles are the second period, the red circles are for the first period. Second period data already had radiative correction applied while first period data are not (this cause the quasi-elastic peak for the first period to be slightly larger (due to the unsubtracted elastic and quasi-elastic tails). The two lower bands are systematic uncertainties.

5.3.1 Background Study

The wall thickness of the reference cell differs from that of the polarized cell, and this needs to be taken into account. The first order correction is the wall thickness which contributes to the two step process. The thicker the thickness, the higher the rate of two step process. This first order correction is made by rescaling the glass contribution when we subtract the glass contribution from the ^{3}He signal. The average wall thickness of the reference cell is 0.8809 mm and that of the ^{3}He cell is 0.7084 mm. In addition, this correction is different for asymmetry and cross section analyses, due to the different cuts applied. For cross sections, with a small solid angle cut on reconstructed angles, the number of events remaining is less than that of asymmetries (see Appendix A.2). The only backgrounds to consider for cross section are from two-step process and downstream glass window on reconstructed y_{tg}. However for the asymmetries there are upstream, two-step process and downstream backgrounds.

To determine the correction, the weighted average from three gaussians is fitted to y_{tg} for asymmetry and two gaussians is fitted to that of cross section analysis.

In addition, the second order corrections due to differences in radiation lengths between reference and polarized cells need to be corrected as well. These differences are due to different gas radiation length (nitrogen versus mostly ^{3}He), densities, and number in the glass entrance window. Consequently, when subtracting the nitrogen from ^{3}He, the nitrogen cross section in the reference cell is different compared to that in ^{3}He cell. The first difference in radiation length is in glass windows and glass exit thicknesses. The second is nitrogen density and radiation length inside reference cell $\approx$ 7.0 amg while that in ^{3}He cell is $\approx$ 0.105 amg. These differences make the radiation effects between the two cells different. A simulated elastic nitrogen tail which takes into account the difference in radiation lengths provides the correction factor to experimental cross section. This correction is different for various kinematic because it depends on the value of ν (or δp). For all beam energies, this correction varies from 82% to 95%.

5.3.2 Momentum Acceptance Correction

Ideally, the extracted unpolarized cross section should depends only on kinematics. However, the cross section extracted here can be distorted by momentum acceptance (the momentum acceptance of spectrometer) which so far has been assumed to be 100%. Hence, momentum acceptance correction may need to be applied. In the carbon, ^{3}He, and N_2 elastic analysis, we made assumption that the acceptance inside our analysis cuts is one (no losses). Comparing the experimental extract elastic cross section to the simulated carbon, ^{3}He, and N_2 cross section with momentum gives us the momentum acceptance correction at the specific δp values at which the elastic peak was set. We then applied a linear fit between the points to obtain the correction function for any δp value within our analysis cuts. The applied function corrects for momentum acceptance and makes the cross section smooth. The acceptance function for first period is found to be:

$$\sigma_0^{cor} = \sigma_0(-4.5 \times \delta p + 1.0), \tag{5.15}$$

where δp is the reconstructed momentum. The same acceptance function is applied to all four beam energies.

5.4 Radiative Corrections

The Feynman diagram for electron scattering in Fig. 1-1 is the leading order process, i.e. the one photon exchange process, which is considered in the theoretical predictions. In addition, the measured quantities at the detector plane have kinematics difference compared with that at interaction vertex. These are due to external radiations, which come from the energy loss of both incident and scattered electrons when they pass through materials. Furthermore, internal radiations exist, which are due to internal bremsstrahlung, vertex corrections and vacuum polarization. Therefore, the measured quantities need to be corrected before to be compared with theoretical calculations, and these corrections are referred to as the radiative corrections.

There are three major effects that contribute to radiative corrections:

- Loop diagram contribution (internal): in addition to the first order Feynman diagram illustrated in Fig. 1-1, higher orders also contribute to the scattering process. Next-to-leading-order effects include: vacuum polarization, and vertex correction. These contributions need to be removed from the measured data.

- Ionization (external): electron loses its energy when passing through materials before and after the interaction vertex. This energy loss change the electron kinematics at the vertex. This energy loss is expected to be small (few MeV level) compared to the beam energies at the level of GeV.

- Photon radiations via Bremsstrahlung (both internal and external): Bremsstrahlung is produced by the change in the electron trajectory in the electromagnetic field of atomic nucleus. The effects are further categorized into internal and external Bremsstrahlungs see Fig 5-13. The former happens during the interaction

between the electron and the nucleon/nucleus on which the hard scattering of Fig. 1-1 occurs, while the latter is caused by the electron passing through materials such as the glass cell wall or other ^{3}He atoms.

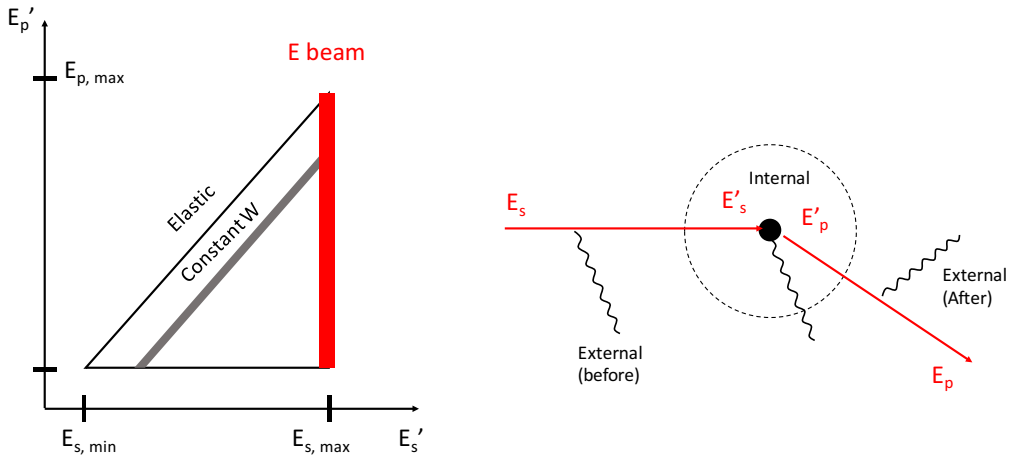

Figure 5-13: Radiative correction. In the plot of beam energy vs scattering energy (left), precise knowledge about the radiative effects requires knowing the cross section in a triangular region for the data set at a constant energy (indicated by the red vertical bar). Right plot: An illustration of the external and internal Bremsstrahlung radiations.

The radiative corrections to extract Born polarized cross section from measured values is given as follows:

$$\begin{aligned} \frac{d\sigma_0^{Born}}{d\Omega dE'} &= \frac{d\sigma_0^{exp}}{d\Omega dE'} + \Delta\sigma_{RC}, \\ \frac{d\sigma_{\parallel,\perp}^{Born}}{d\Omega dE'} &= \frac{d\sigma_{\parallel,\perp}^{exp}}{d\Omega dE'} + (\Delta\sigma_{\parallel,\perp})_{RC}, \end{aligned} \tag{5.16}$$

where $\Delta\sigma_{RC}$ and $(\Delta\sigma_{\parallel,\perp})_{RC}$ are the radiative corrections for unpolarized cross section and polarized cross section differences, respectively.

Before radiative corrections are applied, the elastic (and quasi-elastic) radiative tail needs to be subtracted from the experimental cross section. Due to the high

resolution of the HRS, the elastic peak itself can be well separated from the inelastic region. However, the radiative effect of the elastic channel produces a long tail that extends into the inelastic spectrum. Hence it must be subtracted using a calculation. We used a special procedure due to collimator punch-through effects, which effectively add radiation length for some of the events [60].

Typically cross section models are used to determined radiative corrections, which are applied to the measured data using Eq 5.16. This will introduce model dependency. For E97-110 analysis, the model dependency is minimized by an iterative procedure. In each iteration, the radiative correction results are applied to the measured cross sections, producing cross sections which is then used to update the input model of the corrections. The iteration is repeated until the result converges, producing final results on the Born cross section and the radiative corrections $\delta\sigma_{RC}$. Details of the radiative corrections for second period can be found in C. Peng's thesis [64]. The first period is following the same procedure.

The final uncertainty on the cross section is determined by combining the uncertainty on the radiative corrections $\delta\sigma_{RC}$ with that from the experimental cross section $\delta\sigma_{exp}$:

$$\delta\sigma_{Born} = \sqrt{(\delta\sigma_{exp})^2 + (\delta\sigma_{RC}^{int})^2 + (\delta\sigma_{RC}^{ext})^2}. \tag{5.17}$$

5.5 Polarized Cross Section Differences Results

The polarized cross section differences are calculated by taking the product of the results of experimental asymmetries and unpolarized cross sections:

$$\Delta\sigma_{\perp,\parallel}^{\text{exp}} = 2 \cdot A_{\perp,\parallel}^{\text{exp}} \cdot \sigma_0^{\text{exp}}. \tag{5.18}$$

There are two ways to proceed to form $\Delta\sigma$. The first way (hereafter called "method 1") is take the physical asymmetry (after correcting for glass cell, and nitrogen dilution) and the physical of cross section (after subtracting glass and nitrogen backgrounds), see Eq. 5.19.

$$
\begin{aligned}
A_{^3He}^{physics} &= \frac{A_{^3He}^{raw}}{f \times P_b P_t}, \\
\sigma_{^3He}^{physics} &\propto \sigma_{^3He}^{raw} - \sigma_{N_2}^{raw} - \sigma_{glass}^{raw}, \\
\Delta\sigma_{^3He}^{physics} &= A_{^3He}^{physics} \times \sigma_{^3He}^{physics}.
\end{aligned}
\tag{5.19}
$$

However, due to the poor determination of y_{tg} in the first period, no accurate y_{tg} cut can be applied. Hence the full contamination from unpolarized material affects to our results. All of these contaminations are corrected in the asymmetry by applying a dilution factor, and corrected in the cross section by background subtraction. However, the systematic uncertainty due to these corrections is large. The second way (method 2) is by taking products of diluted ^{3}He asymmetry and background-contaminated cross section see Eq. 5.20.

$$
\begin{aligned}
A_{^3He}^{diluted} &= \frac{A_{^3He}^{raw}}{P_b P_t}, \\
\frac{d\sigma_{^3He}^{cont.}}{d\Omega dE'} &= \frac{d\sigma_{^3He}^{raw}}{d\Omega dE'}, \\
\Delta\sigma_{^3He}^{physics} &= A_{^3He}^{diluted} \times \sigma_{^3He}^{cont.},
\end{aligned}
\tag{5.20}
$$

where the dilution of the asymmetry is cancelled by the background contamination. If the backgrounds are unpolarized and if the analysis cut for $A_{^3He}^{diluted}$ and $\frac{d\sigma_{^3He}^{cont.}}{d\Omega dE'}$ are identical, then the cancellation is exact. This method, does not introduce more systematic uncertainties due to background subtraction. Ideally, the two methods should give us the same result. However, due to small acceptance cut imposed for the cross section analysis by the defective septum, cuts applied to the cross section and asymmetry are quite different. The cuts on asymmetry are wider compare to that of cross section since on the one hand statistics is critical for the asymmetry while on the other hand, good knowledge of the acceptance is unnecessary. Because of this, the cancellation of background in the second method may not be perfect. Hence a careful study was conducted to compare results between the two methods.

Fig. 5-14 and Fig. 5-15 show the consistent check between the two methods for

the 2.2 GeV beam setting. The bottom plot shown the difference between results from two methods $\Delta = \Delta\sigma_{\text{method 1}} - \Delta\sigma_{\text{method 2}}$ and the estimate uncertainty $\delta\Delta = \sqrt{\frac{1}{(\frac{1}{\delta\Delta\sigma_{method1}})^2 - (\frac{1}{\delta\Delta\sigma_{method2}})^2}}$. The two methods are consistent with each other, hence, we trust the background does not contaminate the extracted cross section in both methods. Because the statistical uncertainty from method 2 is better than that of method 1, method 2 will be used for our final results on the cross section differences.

Once radiative corrections are applied, the cross section difference is expressed as:

$$\Delta\sigma_{\perp,\parallel}^{\text{Born}} = \Delta\sigma_{\perp,\parallel}^{\text{exp}} + \delta(\Delta\sigma_{\perp,\parallel})^{\text{RC}}. \tag{5.21}$$

For the analysis presented here, radiative corrections were applied to the cross section differences directly. Because the polarized cross section differences are generated from multiplying experimental unpolarized cross sections with parallel or transverse asymmetries, the systematic uncertainties come from the uncertainties on the experimental cross sections ($\approx 10\%$) see Table 4.5, and asymmetry (estimate $\approx 12\%$).

Results for the cross section differences are shown in Fig 5-16. The parallel configuration is represented by the black squares, while the perpendicular is shown by the red squares.

5.6 Spin Structure Functions Results

From the cross section differences, one can obtain the ^{3}He spin dependent structure functions:

$$\begin{aligned} g_1 &= \frac{MQ^2}{4\alpha^2}\frac{\nu E}{(E-\nu)(2E-\nu)}\left[\Delta\sigma_{\parallel} + \tan\frac{\theta}{2}\Delta\sigma_{\perp}\right], \\ g_2 &= \frac{MQ^2}{4\alpha^2}\frac{\nu^2}{2(E-\nu)(2E-\nu)}\left[-\Delta\sigma_{\parallel} + \frac{E+(E-\nu)\cos\theta}{(E-\nu)\sin\theta}\Delta\sigma_{\perp}\right]. \end{aligned} \tag{5.22}$$

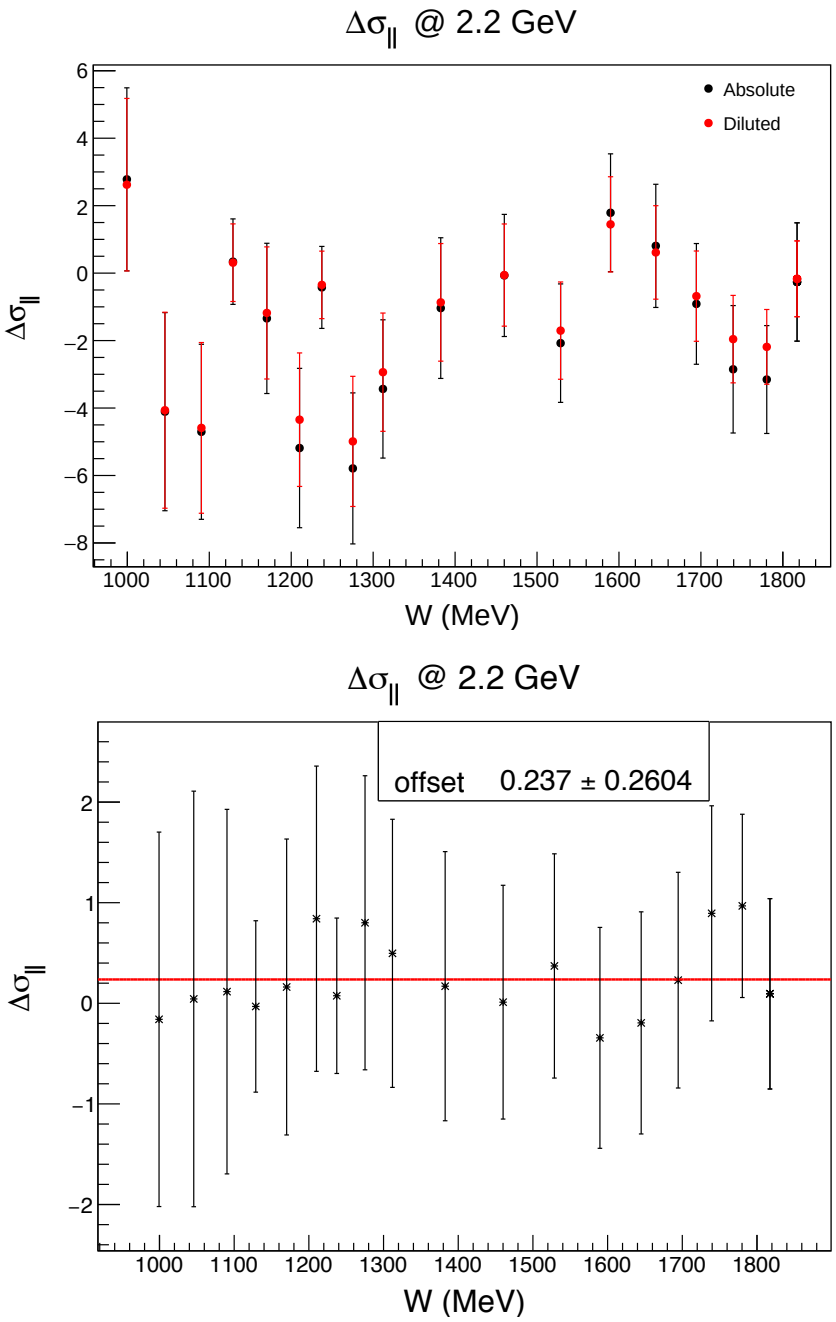

Figure 5-14: Difference in the extracted polarized cross sections (parallel) between two methods, $\Delta\sigma_{method1} - \Delta\sigma_{method2}$, with a constant fit ("offset"). See text for details for the calculation of the uncertainty. Because the "offset" value is consistent with zero, we can conclude the two methods are consistent with each other.

And results on the virtual photoabsorption cross section can be calculated as:

$$\begin{aligned} \sigma_{TT} &= \frac{4\pi^2\alpha}{MK}\left(g_1 - \frac{Q^2}{\nu^2}g_2\right), \\ \sigma_{LT} &= \gamma\frac{4\pi^2\alpha}{MK}(g_1 + g_2), \end{aligned} \tag{5.23}$$

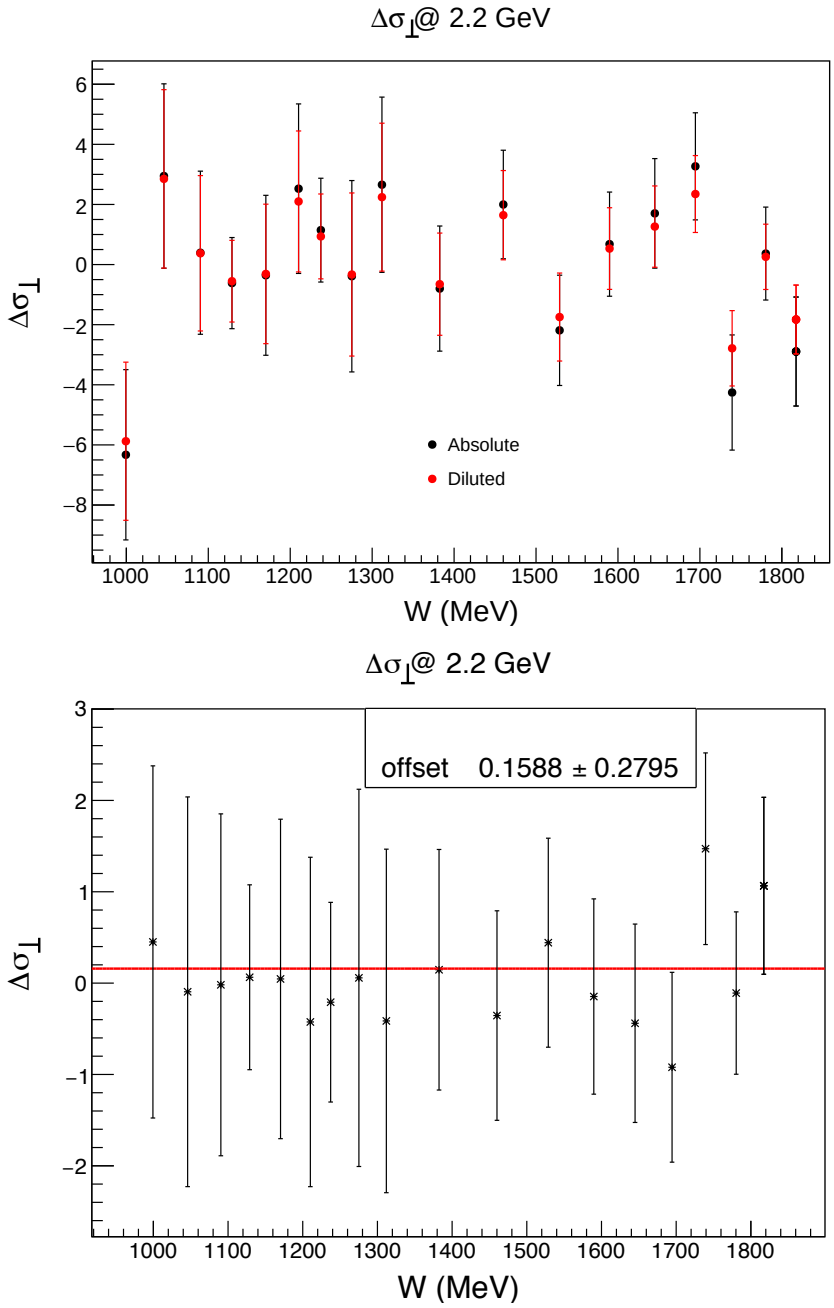

Figure 5-15: Difference in the extracted polarized cross sections (perpendicular) between two methods, $\Delta\sigma_{method1} - \Delta\sigma_{method2}$, with a constant fit ("offset"). See text for details for the calculation of the uncertainty. Because the "offset" value is consistent with zero, we can conclude the two methods are consistent with each other.

where we used the Gilman convention $K = \sqrt{\nu^2 + Q^2}$. Or in term of measured cross

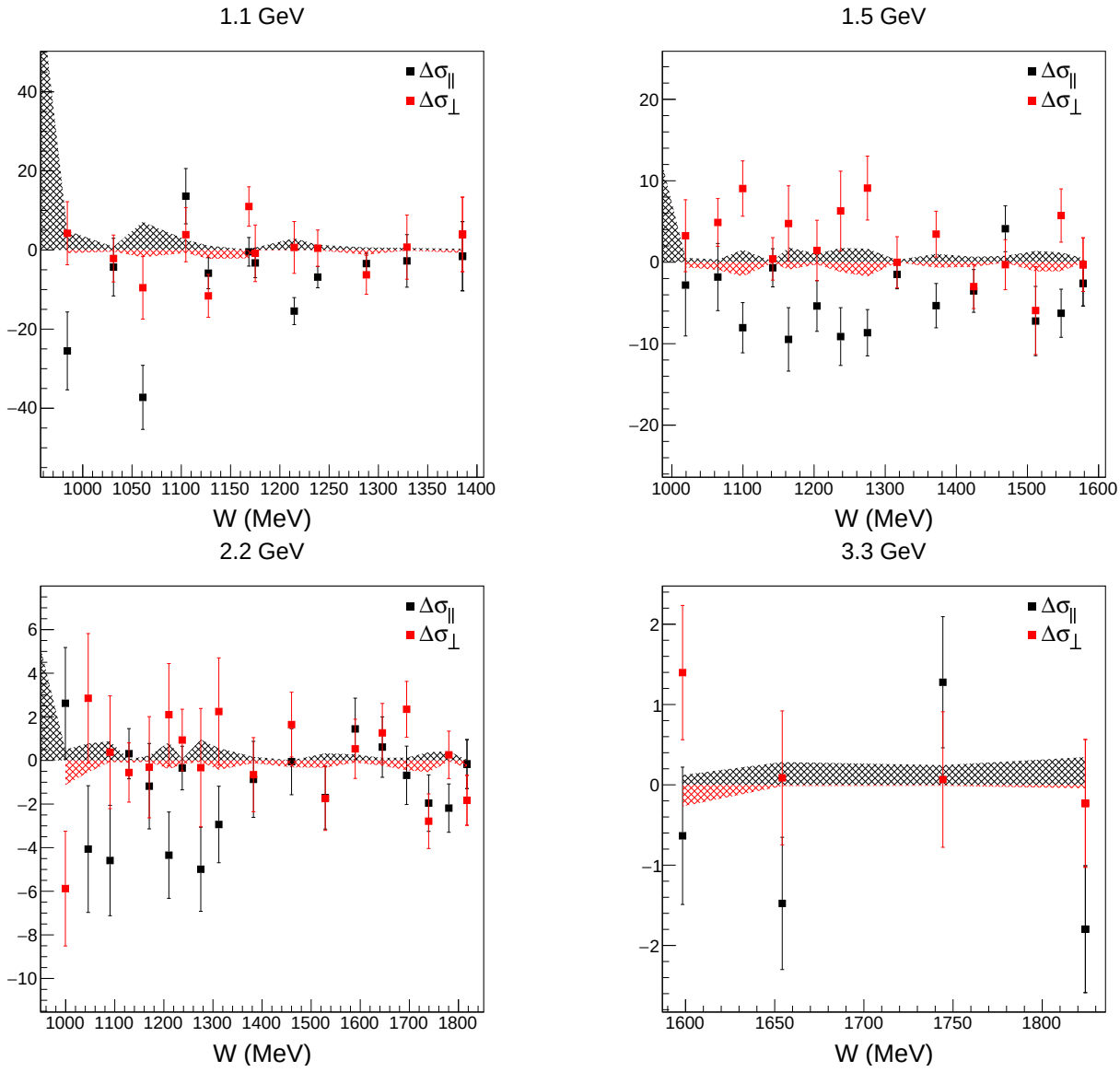

Figure 5-16: Preliminary cross section differences for four beam energies for first period. The $\Delta\sigma_{\parallel}$ is represented by black square. The $\Delta\sigma_{\perp}$ is represented by red square. The error bars are statistical uncertainties and the error bands are systematic uncertainties. Results are corrected for radiative effect.

section differences:

$$\sigma_{TT} = \frac{\pi^2 Q^2}{\alpha K} \frac{1}{(1-y)(2-y)} \left[\Delta\sigma_{\parallel} - (\Delta\sigma_{\parallel}\cos\theta + \Delta\sigma_{\perp}\sin\theta)(1-y)\right], \qquad (5.24)$$

where $y = \frac{\nu}{E}$.

The ^{3}He spin structure functions are plotted versus x, as measured at constant

energy, in Fig. 5-17 and Fig. 5-18. The error bars represent statistical uncertainties and the error bands represent systematic uncertainty. Proceeding right to left along the horizontal axis, we encounter the quasi-elastic peak, the $\Delta(1232)$ resonance, and then the inelastic region.

Fig. 5-19 shown σ_{TT} at constant energy for four beam energies. Results are before radiative corrections. An estimate of Γ_1 (given in 1.29) and its statistical uncertainty are shown in Fig. 5-20.

In resonance region, and at low Q^2, one does not know how to do extract of neutron results from ^{3}He for g_1, g_2, σ_{LT}, σ_{TT}. So these results remain on ^{3}He.

5.7 The Phenomenological MAID Model

The MAID model [30] uses phenomenological fits to photo- and electroproduction data on the nucleon to provide various scattering cross sections and partial cross sections in the domain from the pion-production threshold to $W = 2$ GeV. It satisfies gauge invariance and unitarity. The model contains Born terms, mesons and nucleon resonances up to the third resonance region. The model assumes the resonances have the Breit-Wigner shape as follows:

$$\sigma_{1/2(3/2)} = \frac{4M}{W_{res}\Gamma_{res}} A^2_{1/2(3/2)} B(\nu, Q^2), \tag{5.25}$$

where W_{res} and Γ_{res} are the mass and width of the resonance, respectively. $A_{1/2(3/2)}$ are the helicity dependent amplitudes. $B(\nu, Q^2)$ represents the generalization to electroproduction of the Breit-Wigner form.

The model agrees well, in general, with existing experimental data for pion photo- and electroproduction on the nucleon for both unpolarized and polarized differential cross sections. The model agrees well with data from the proton GDH sum rule. However, it does not agree with GDH sum at the real photon point for the neutron.

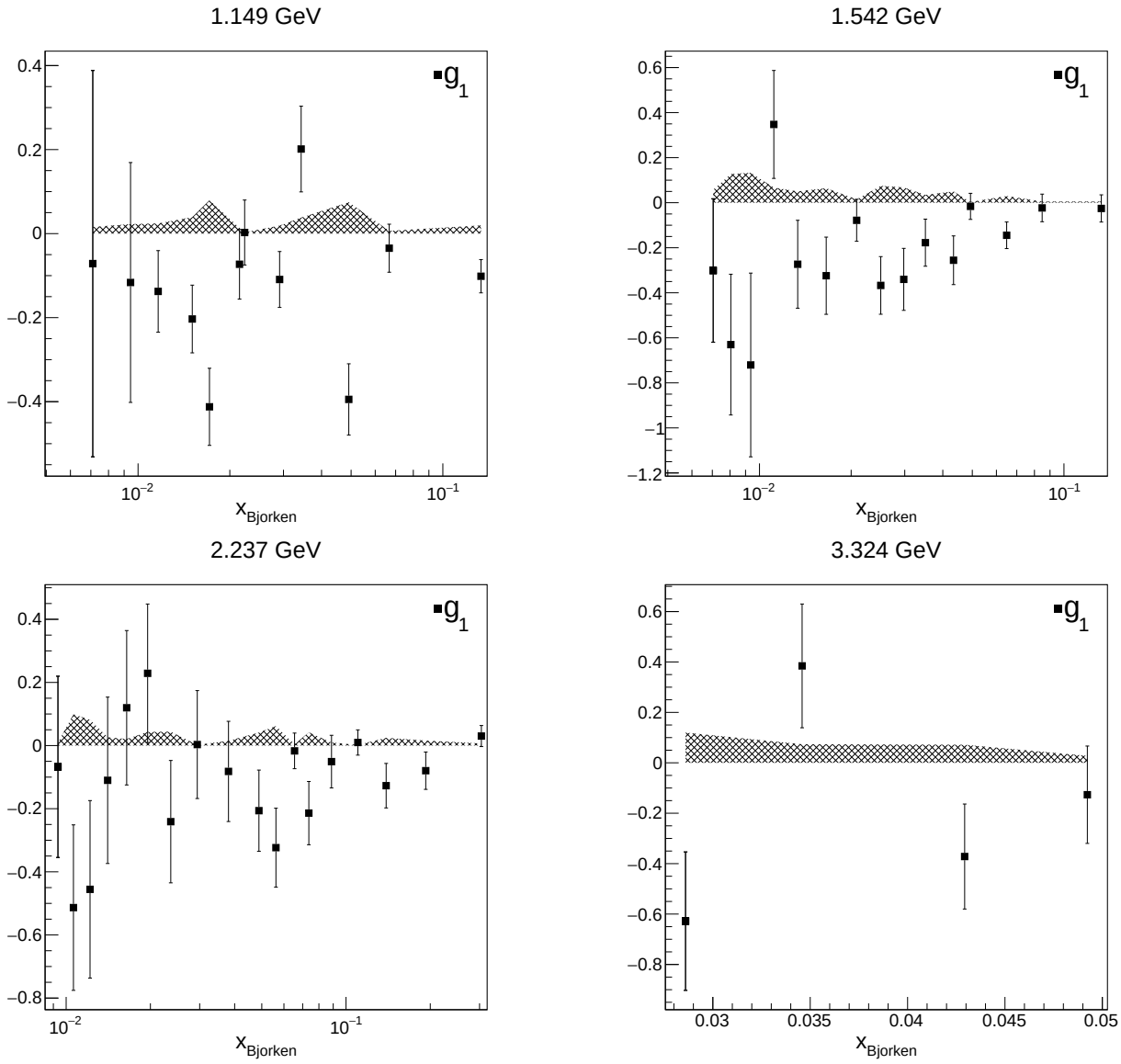

Figure 5-17: Preliminary results on neutron structure functions g_1 at constant beam energy. The error bars represent statistical uncertainty and the error bands represent systematic uncertainty. Results are before radiative correction.

5.8 Conclusions and Outlook

The E97-110 experiment successfully collected data to extract the cross section difference in the Q^2 range from 0.02 to 0.3 GeV^2. In this thesis, the preliminary results of asymmetry, unpolarized cross section, cross section difference, spin structure function, σ_{TT}, and Γ_1 are presented. The generalized GDH sum rule of ^{3}He is firstly

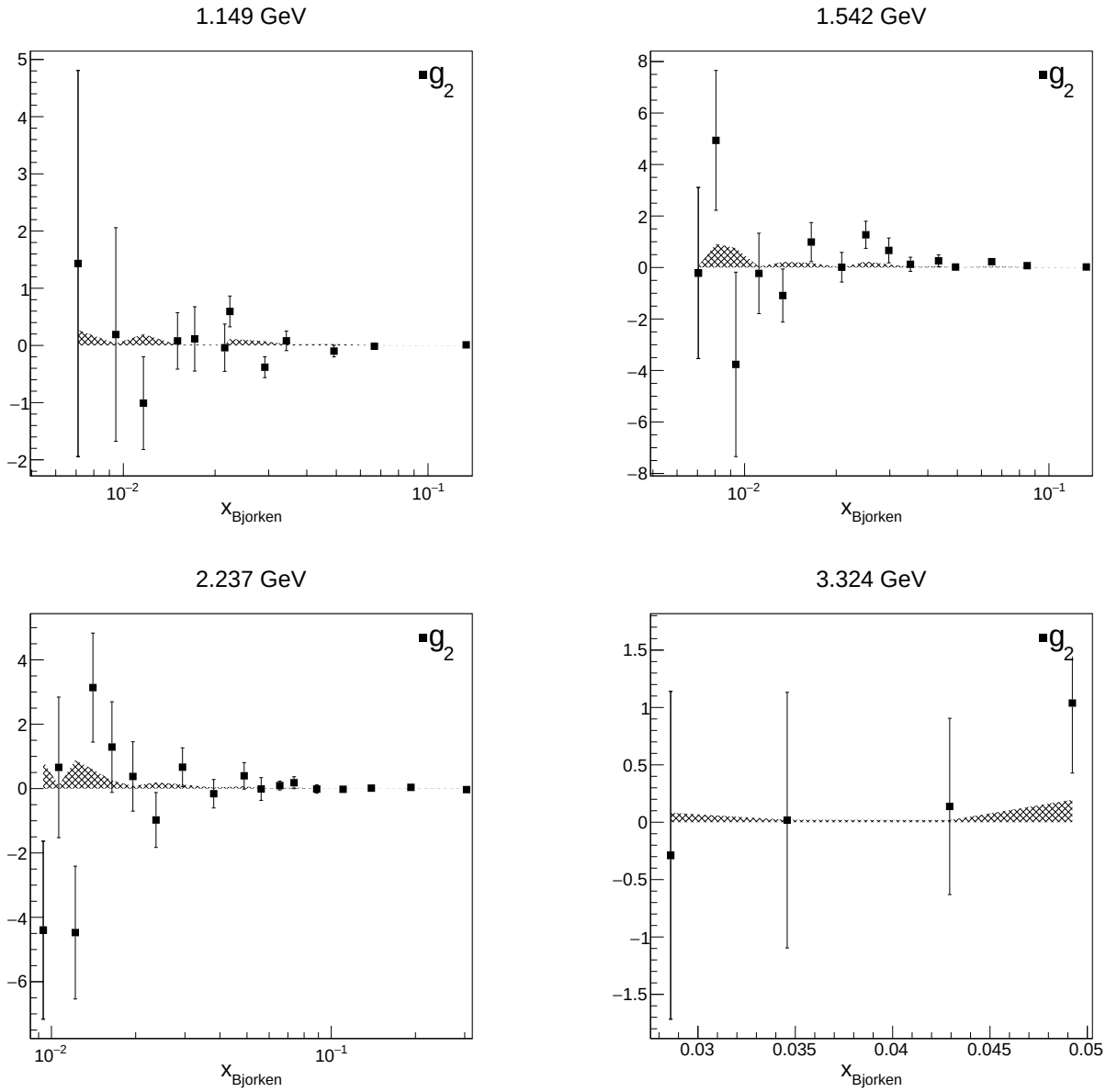

Figure 5-18: Preliminary results on neutron structure functions g_2 at constant beam energy. The error bars represent statistical uncertainty and the error bands represent systematic uncertainty. Results are before radiative correction.

measured for $Q^2 < 0.1$ GeV^2, and the experimental data reveal the "turn-over" point of $I_{GDH}(Q^2)$ at around 0.1 GeV^2. In addition, our data exhibit a sharp change in slope of $I_{GDH}(Q^2)$ at lower Q^2, and hence suggest the recovery of the GDH sum rule at the real photon point. Radiative correction and target polarization are ongoing. Once these two numbers are finalized, interpolation at different energies will be required to obtain Γ_1 and I_{TT} at constant Q^2. After that, these are final results and reach

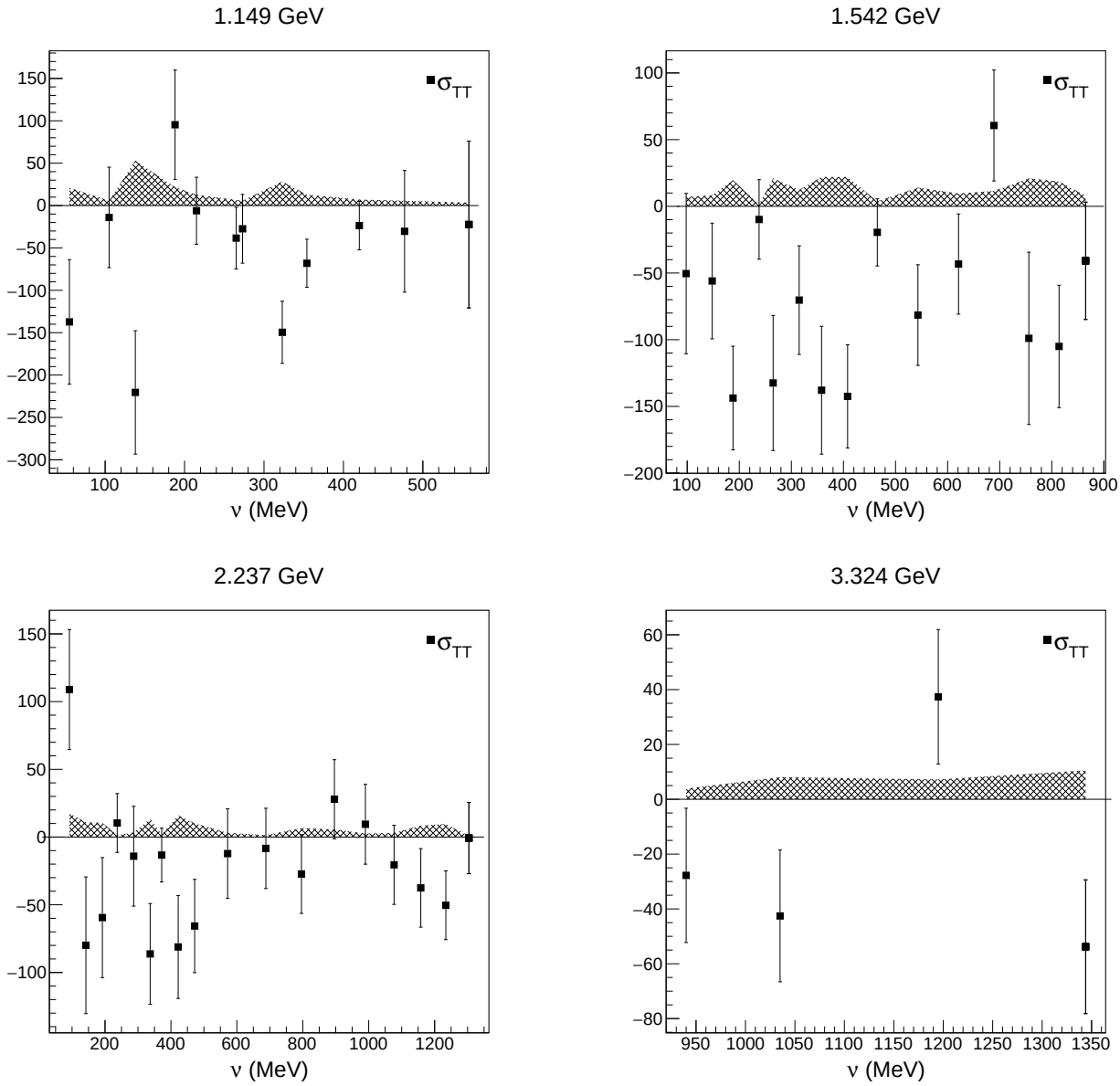

Figure 5-19: Preliminary results on σ_{TT} (μb) at constant beam energy. The error bars represent the statistical uncertainty. The error bands represent the systematic uncertainty. Results are before radiative correction.

publishable level.

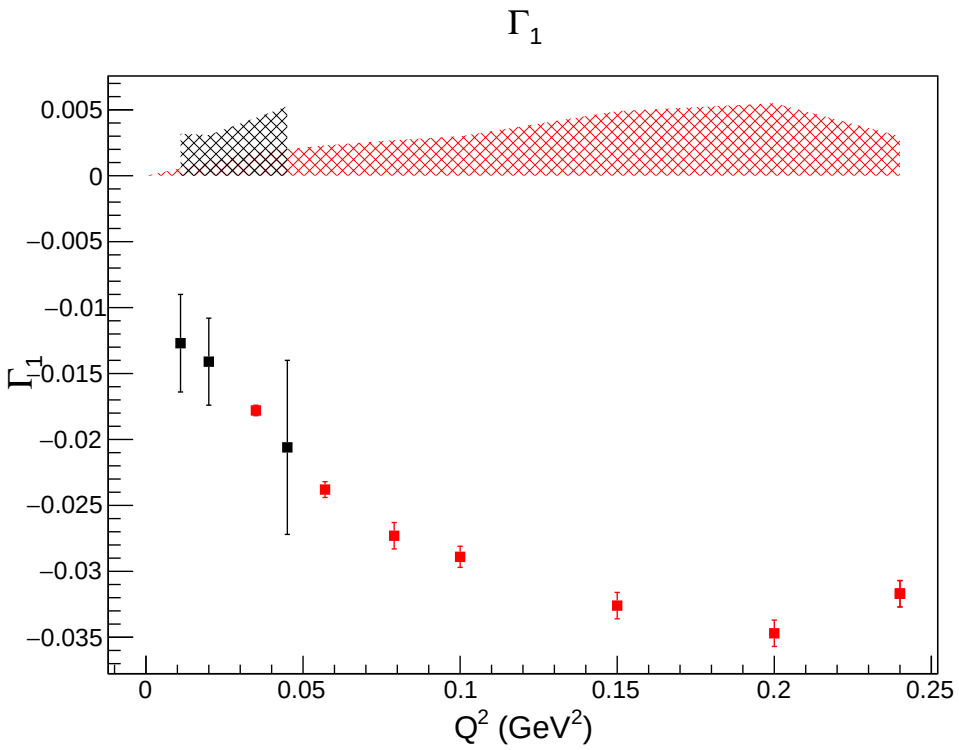

Figure 5-20: Γ_1^n preliminary results on both period. Black squares are first period data, red squares are second period data. Results from first period are before radiative correction. Results from second period are after radiative correction. The bands are systematic uncertainties.

Chapter 6

The Upgrade of The Polarized ^{3}He Target

The 6 GeV era ^{3}He target has been using in many experiments at JLab.This chapter will discussed about the upgrade of the polarized ^{3}He target at JLab.

6.1 JLab ^{3}He Lab Setup

The target system at JLab includes a laser/optic system, an oven, the ^{3}He cell and three pairs of Helmholtz coils as shown in Fig. 6-1. The cell is held at the center of the target where the pumping chamber of the cell is mounted inside the oven that is heated to 250°C. Three pairs of Helmholtz coils are used to create a uniform magnetic field in three dimensions. The magnetic field average strength is 25 G and a typical gradient in the region occupied by the cell is 2-10 mG/cm.

6.1.1 Upgrade in Laser and Hybrid Mixture

In recent years, an advanced technique called Rb-K hybrid spin-exchange optical pumping was developed and greatly improved the spin-exchange efficiency. The main reason is that K relaxation is much slower than Rb, thus the spin-exchange efficiency is about one order of magnitude higher. However, there is no commercial and high-

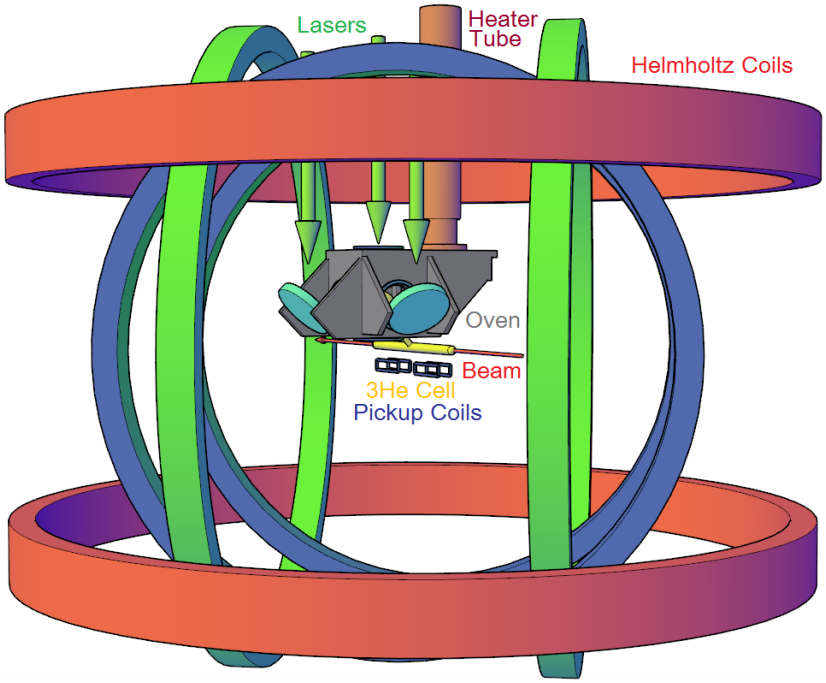

Figure 6-1: Target overview during Transversity experiment E06010 [65].

power narrow-width laser to polarized K directly. On the other hand, K can be polarized through the fast Rb-K spin-exchange and the K vapor can reach almost the same polarization as Rb vapor. Hence, the tradition Rb cell is replaced by Rb-K hybrid cell.

In addition, the optical pumping has been greatly improved with the advance of laser techniques. The newly available narrow-linewidth diode lasers (COMET, QPC, Raytum) with FWHM$\approx$ 0.25 nm provide a much higher optical pumping efficiency than the board-width diode lasers (Coherent) with FWHM$\approx$ 1.5 nm and the in-beam ^{3}He target polarization subsequently increased from 40% (during E97-110 in 2003) to 60% (during Transversity [69] in 2009). If the laser light has a very large line width, a significant amount of light is not within the absorption line-width and wasted. In addition, the unusable light also adds to the thermal depolarization.

6.1.2 Target Cells

The target cell is a glass cell containing high pressure ^{3}He gas with very thin windows. A typical target cell of the 6 GeV era is shown in Section 2.7. With this type of cell, the polarization is transferred from pumping to target chamber through diffusion which takes a long time and creates a large polarization gradient between the two chambers. The larger the length of the transfer tube, the larger the polarization difference. This polarization gradient can be reduced by using a convection cell where the gas inside circulates faster thanks to a convection flow. This convection flow is accomplished by using two transfer tubes instead of one, and a heating coil to create the convection as shown in Fig. 6-2. The convection-type cells are planned to be used for the 12 GeV running of JLab.

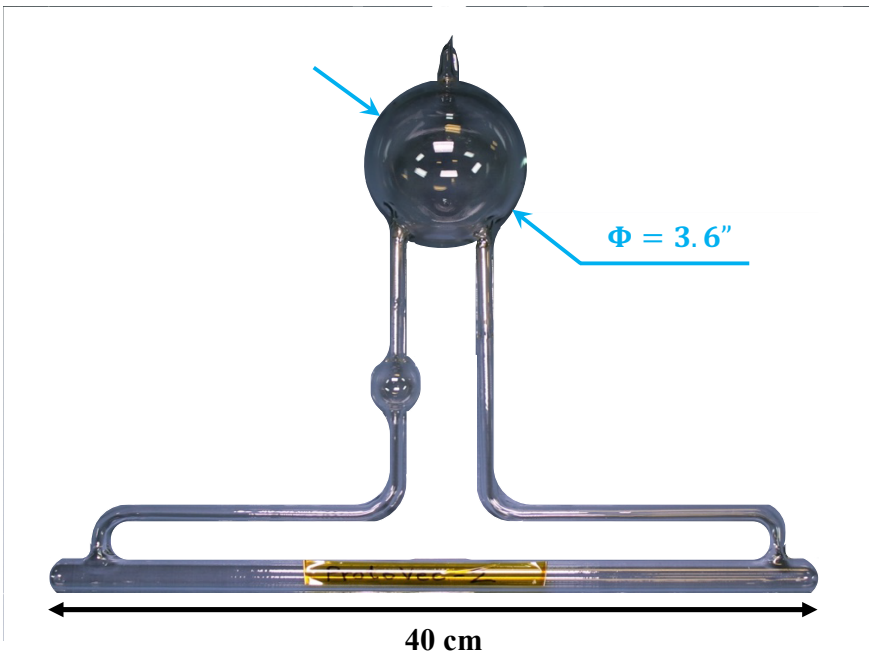

Figure 6-2: Convection-type cells for upgrade ^{3}He target.

6.2 NMR Polarimetry

For JLab ^{3}He target, there are three methods to measure the ^{3}He polarization - Nuclear Magnetic Resonance (NMR) polarimetry, electron paramagnetic resonance (EPR) polarimetry and Pulse Nuclear Magnetic Resonance (PNMR) polarimetry. There is another way to measure the polarization is using elastic asymmetry. The NMR measures the electromagnetic signal induced by the ^{3}He spin reversal through the adiabatic fast passage (AFP) [68] and is used to extract the ^{3}He polarization relatively. The EPR measures the frequency shift in the Rb EPR and provides an absolute polarization measurement to calibrate the ^{3}He NMR and PNMR signal. PNMR measure the signal induced by the precession of ^{3}He spin decaying after being brought to resonance.

6.2.1 NMR Principle

In order to describe the NMR principle, suppose we are in an isolated spin system where spins do not interact with each other (if they interact, which will be discussed later, spin start to relax to equilibrium). As the first step, consider a magnetic moment $\vec{M}$ placed in a static magnetic field $\vec{H}$, the spins will precess with an equation of motion:

$$\frac{d\vec{M}}{dt} = \gamma\vec{M} \times \vec{H}, \tag{6.1}$$

with $\vec{M} = M_x\hat{x} + M_y\hat{y} + M_z\hat{z}$ and $\vec{H} = H_0\hat{z}$ and γ is the ^{3}He gyromagnetic ratio ($\gamma = -3.243$ kHz/G).

Solving this differential equation we obtain:

$$\vec{M} = M_{x0}(\cos\omega t\hat{x} - \sin\omega t\hat{y}) + M_{z0}\hat{z}. \tag{6.2}$$

This means that the magnetization rotates clock-wise around z-axis with angular velocity $\omega = \gamma H_0$.

Then, a second, rotating field $\vec{H_1}$ is added perpendicular to the static field $\vec{H}$.

The rotating field can be expressed as

$$\begin{aligned}\vec{H}_1 &= 2H_1\cos(\omega t)\hat{x} = H_1[\cos(\omega t)\hat{x} - \sin(\omega t)\hat{y}] + H_1[\cos(\omega t)\hat{x} + \sin(\omega t)\hat{y}] \\ &= H_1^{CW} + H_1^{CCW},\end{aligned} \tag{6.3}$$

where CW (CCW) stands for clockwise (counter clockwise) with respect to lab frame.

In the rotating frame (x', y', z) of the magnetization $\vec{M}$, the clockwise component is static, while the counter clockwise component is rotating at twice the frame frequency and in opposite direction, thus $\vec{H}_1 = H_1\hat{x}' + H_1(\cos 2\omega t\hat{x}' + \sin 2\omega t\hat{y}')$.

In the clockwise frame:

$$\frac{\partial\vec{M}}{\partial t} = \gamma\vec{M} \times (\vec{H} - \frac{\vec{\omega}}{\gamma}). \tag{6.4}$$

where $\frac{\vec{\omega}}{\gamma}$ is the fictitious field due to rotation and ω is the angular velocity of the rotating frame. The equation of motion can be rewritten as:

$$\frac{\partial\vec{M}}{\partial t} = \gamma\vec{M} \times \vec{H}_{eff}, \tag{6.5}$$

$$\text{with } \vec{H}_{eff} = (H_0 - \frac{\omega}{\gamma})\hat{z} + H_1\hat{x}'. \tag{6.6}$$

At resonance, $\omega = H_0\gamma$, the magnetization will rotate around $\vec{H}_1$.

Now let us examine the other component of H_1, rotating in the opposite direction:

$$\begin{aligned}\vec{H}_{eff} &= (H_0 + \frac{\omega_0}{\gamma})\hat{z} + H_1\hat{x}'' \\ &= 2H_0\hat{z} + H_1\hat{x}''\end{aligned} \tag{6.7}$$

The magnitude of the effective field is $|H_{eff}| = \sqrt{4H_0^2 + H_1^2}$. The angle between magnetization $\vec{M}$ and the main field $\vec{H}$ is $\theta = \tan^{-1}(H_1/2H_0)$, with $H_1 \ll H_0$ and thus the angle is very small. So the effect of the counter clockwise component is very small compare to the clockwise one.

In summary, $\vec{M}$ would follow $\vec{H}_1$ and can be flipped completely if $\vec{H}_1$ is applied a long enough time. In the next section we explain the adiabatic fast passage (AFP),

which is a condition that minimizes polarization loss during such spin flips.

Adiabatic Fast Passage

For minimal losses of polarization to occur during an AFP magnetic field sweep, two conditions must be satisfied. First, the sweep must be slow enough for the magnetization to follow the effective field adiabatically. This is possible only if the rotation of magnetization around the static field in the laboratory frame (which is characterized by frequency ω) is much faster than the rotation of the effective field H_{eff}. This condition ensures that the initial relationship of the magnetization with respect to the effective field remains valid throughout the sweep.

If the variation of the field with time is slow enough, the angle of magnetization with the instantaneous direction of the fields is also a constant of motion. In the rotating frame, the effective field is given by Eq. 6.6. If the static magnetic field is varied in time, then H_z is a time-varying field $H_z(t)$, the change of effective field with time is

$$\begin{aligned} \frac{d\vec{H}_{eff}}{dt} &= \frac{dH_0\hat{z}}{dt} = \dot{H}_0\hat{z} \\ &= \cos\theta\frac{\dot{H}_0}{H_e}\vec{H}_e + \sin\theta\frac{\dot{H}_0}{H_{eff}}(\hat{n}\times\vec{H}_e), \end{aligned} \tag{6.8}$$

where the unit vector along H_0 can be rewritten as $\hat{z} = \cos\theta\hat{H}_{eff} + \sin\theta(\hat{n}\times\hat{H}_{eff})$. $\hat{n}$ is a unit vector orthogonal to $\vec{H}_0$ and $\vec{H}_1$. The variation with time of a vector $\vec{H}$ can be written as

$$\frac{d\vec{H}}{dt} = \vec{\Omega}\times\vec{H} + \Omega_1\vec{H}. \tag{6.9}$$

Comparing this equation to Eq. 6.8 gives

$$\Omega = \sin\theta\frac{\dot{H}_0}{H_{eff}} = H_1\frac{\dot{H}_0}{H_{eff}^2}. \tag{6.10}$$

Combining with the adiabatic condition $|\Omega| \ll |\gamma H_e|$ [68], we have $\dot{H}_0 \ll \frac{\gamma H_e^2}{\sin\theta}$. At resonance, $\dot{H}_0 \ll \gamma H_1^2$. This is the first condition of AFP.

The magnetic field sweep rate is chosen so that no appreciable relaxation takes place during the sweep. It means that it must be fast enough so that minimal transverse relaxation occurs during sweep. This condition ensures that the magnetization vector remains constant in length during the sweep (or not so much loss). In particular, if the nuclei were in thermal equilibrium with the surrounding to begin with so that the macroscopic magnetization pointed along the static field, it will follow the effective field during the passage and will end up 180 degrees rotated by the passage.

In our AFP-NMR, dB_z/dt =1.2 G/s, B_1 ∼0.1 G, and the resonance frequency is f_{3He} = 91 kHz. Therefore, $\frac{dB_z/dt}{B_1} \ll \omega$.

6.2.2 NMR Setup and Analysis

When spins pass through the nuclear magnetic resonance, they will induce an EMF signal in a pair of pickup coil set around the cell. The signal height is proportional to the target polarization. Hence, the polarization can be extracted from signal height. However, we need to calibrate this signal with a well-known polarization, such as that measured for the thermal polarization of water through the water NMR measurement.

There are three sets of coils for NMR polarimetry: the Helmholtz coils provide the uniform main holding field (along z-axis which is pointing along the main holding field). The RF coils provides the RF field perpendicular to the main holding field with a much smaller magnitude compared to the holding field (a typical RF field is ∼ 100 mGauss whereas the main holding field is 25 Gauss). The third sets of coils is the pickup coils. These are mounted perpendicular to both the main and the RF fields. A imperfect mounting of the pickup coils can introduce noise into our signal.

There are two types of AFP sweeps. The first is the NMR-AFP field sweep, in which the RF field magnitude is kept 91 kHz while the main holding field is swept from 25 Gauss through resonance (∼ 28 Gauss) to 32 Gauss then swept back. The signal from pickup coil is sent to a preamplifier. The signal is then fed to a lock-in amplifier as shown in Fig. 6-3. The second type of sweep is the NMR-AFP frequency sweep, the main field is kept constant at 25 Gauss and the RF frequency is swept from 78 kHz to 85 kHz.

The pickup coils are mounted on both sides of the target chamber as shown in Fig. 6-3. This orientation will reduce background and enhance the signal. The detected signal is proportional to the ^{3}He magnetization and polarization as follows:

$$S_{NMR}(t) \propto M_T \propto \langle P_{^3He} \rangle \frac{H_1}{\sqrt{(H(t) + \frac{\omega}{\gamma})^2 + H_1^2}}, \tag{6.11}$$

where $P_{^3He}$ is the ^{3}He polarization. The second term comes from the transverse component of the magnetization as a function of the magnetic field, where the angle between the total magnetization and z-axis can be written as follow:

$$\theta = \arctan \frac{H_1}{\sqrt{(H + \frac{\omega}{\gamma})^2 + H_1^2}}. \tag{6.12}$$

A typical NMR signal is shown in Fig. 6-4. This signal is fitted with

$$S(t) = \frac{hH_1}{\sqrt{H_1^2 + (H(t) - H_0)^2}} + AH(t) + B, \tag{6.13}$$

where h is the signal height, H_1 is the RF field, H_0 is the field at resonance, A and B are coefficients to account for a linear background.

6.2.3 Extracting Polarization From AFP-NMR Signal

^{3}He polarization is contained in the value h in Eq. 6.13. The polarization can be extracted from h by performing an NMR water measurement. The water is contained in a glass cell made similarly to the helium cells. The proton in water have a magnetic moment that can be aligned in a magnetic field which gives the water a small, but well-known polarization. This polarization can be described by $P_w = \chi H$ where $\chi = 3.4616 \times 10^{-10}$/Gauss at 22°C.

The polarization of the NMR [49] can be extracted as follows:

$$\frac{P_{^3He}}{P_w} = \left(\frac{h}{h_w}\right) \left(\frac{\mu_p n_p \Phi_{tot}}{\mu_{^3He}(\Phi_{pc} N_{pc} + \Phi_{tc} n_{tc} + \Phi_{tt} n_{tt})}\right) \left(\frac{G_p^w C_\Delta^w C_\tau^w}{G_p C_\Delta C_\tau}\right), \tag{6.14}$$

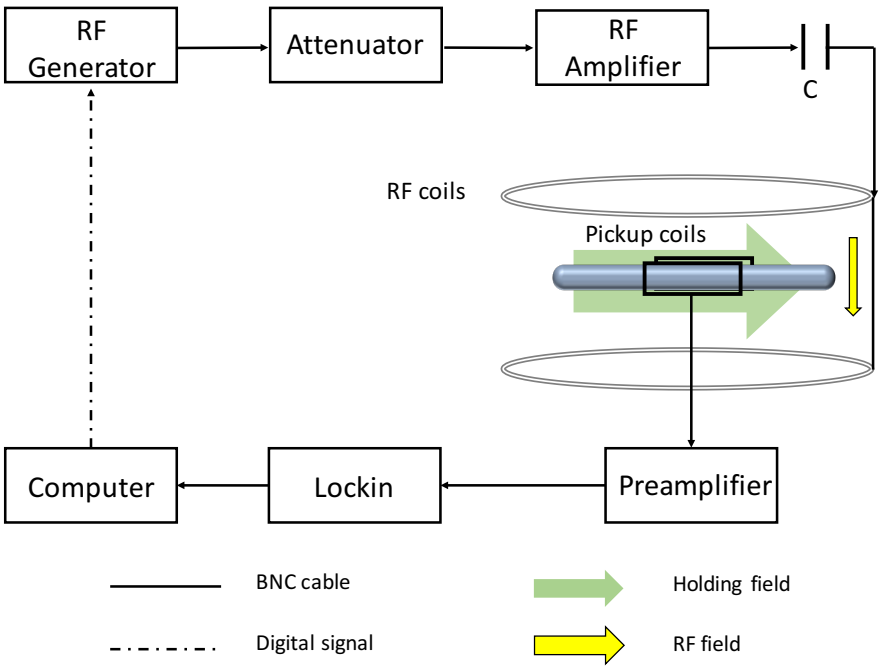

Figure 6-3: NMR setup.

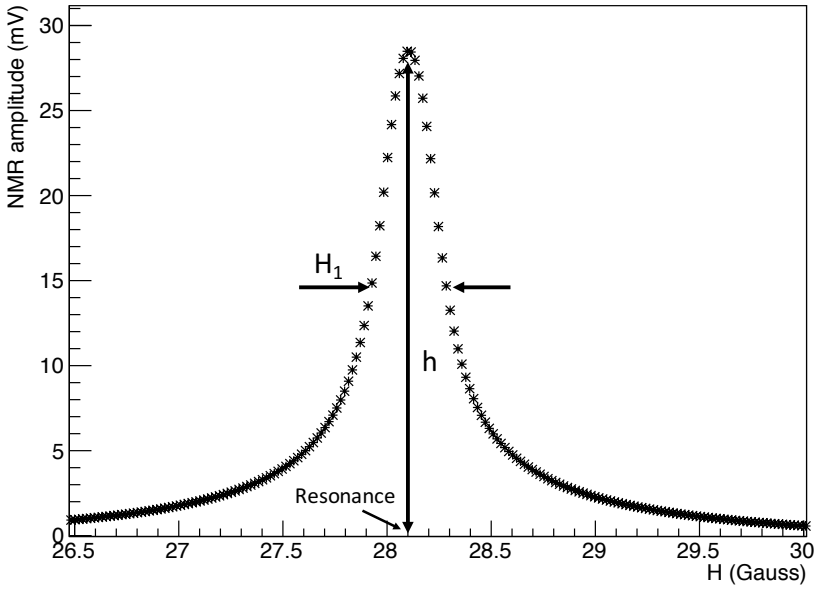

Figure 6-4: NMR signal at the target chamber. The signal width is proportional to H_1 ($\sim$ 90 mGauss). H_0 (28.1 Gauss) is the field at resonance for ^{3}He at 91 kHz.

Parameter	Description
h/h_w	NMR signal height of ^{3}He/water
P_{th}	Thermal polarization of water (7.481×10^{-9})
$\mu_{^3He}$	magnetic moment of ^{3}He (1.155×10^{-13} MeV/T)
$\Phi_{pc,tc,tt}$	magnetic flux of PC, TC and TT through pickup coil
Φ_{tot}	Total magnetic flux of cell through the pickup coil
$n_{pc,tc,tt}$	^{3}He density in PC, TC and TT
N_c	number of windings in pickup coils
G_c	Gain of the pickup coils
G_p	Gain of the pre-amplifier
G_l	Gain of the lock-in amplifier
C_Δ	Correction factor due to the holding field gradient
C_τ	Correction factor due to the lock-in time constant
C_α	Correction factor due to the attenuation in the cable

Table 6.1: Parameters used in extracting polarization from NMR signals. PC: pumping chamber, TC: target chamber, TT: transfer tube.

where parameters are given in Table 6.1. Since P_w is known, after measurement of the water signal h_w a calibration constant c_w is calculated:

$$c_w = \left(\frac{P_w}{h_w}\right)\left(\frac{\mu_p n_p \Phi_{tot}}{\mu_{^3He}(\Phi_{pc}n_{pc} + \Phi_{tc}n_{tc} + \Phi_{tt}n_{tt})}\right)\left(\frac{G_p^w C_\Delta^w C_\tau^w}{G_p C_\Delta C_\tau}\right) \tag{6.15}$$

then the polarization from NMR measurements on ^{3}He can be extracted with $P_{^3He} = c_w h$.

6.3 EPR Polarimetry

The second polarimetry measures the shift of electron paramagnetic resonance (EPR) frequency in the rubidium electrons states when the polarization direction of the polarized ^{3}He nuclei is reversed. The EPR frequency is caused by the Zeeman splitting between electron state $F = 3, m = -3$ to $F = 3, m = -2$ (the D2 line). This frequency depends on the total magnetic field which is the sum of main holding field and a much smaller contribution from the polarized ^{3}He nuclei. From the frequency difference between before and after reversing the spins, one can precisely determine the additional magnetic field due to the polarized ^{3}He gas. Unlike NMR polarimetry,

EPR provides an absolute polarization measurement for the ^{3}He in the pumping chamber.

The frequency difference is measured by the frequency at which electrons in the $F = 3, m = -3$ state can absorb photons and be transferred to the $F = 3, m = -2$ state. This is done by using an excitation coil near the pumping chamber of the target cell. This perturbation (EPR RF) field greatly increases the electron population in the $F = 3, m = -2$ state. The increase in D_2 light is large enough to be measured by a photodiode. The EPR frequency shift is shown in Fig 6-5.

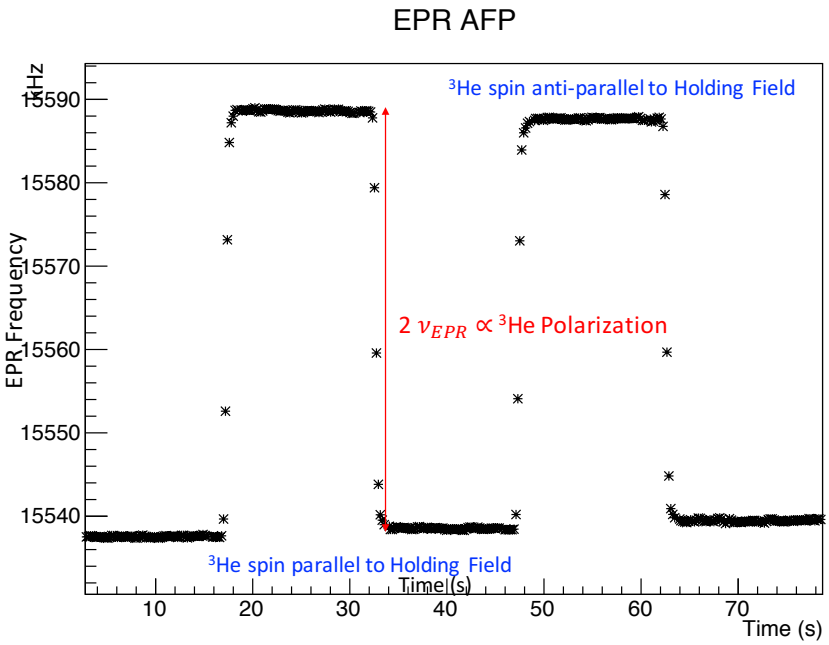

Figure 6-5: EPR frequency shift spectrum during AFP frequency sweep when pumped by σ_+ light.

The frequency difference ($2\Delta\nu$) is proportional to the polarization:

$$2\Delta\nu = \frac{4\mu_0}{3}\frac{d\nu_{EPR}}{dB}\kappa\mu_{^3He}n_{pc}P_{^3He}, \tag{6.16}$$

where $\mu_{^3He}$ is the magnetic moment of ^{3}He, n_{pc} is the number density of the pumping chamber, $P_{^3He}$ is the polarization of the ^{3}He in the pumping chamber and the derivative $d\nu_{EPR}/dB$ and κ are constants obtained from atomic physics measurements.

Detailed analysis of $d\nu_{EPR}/dB$ and κ can be found in [67].

6.4 Pulse NMR Polarimetry

While a beam current of up to 15 μA was used in the 6 GeV era (E97-110 used typically a few μA. The typical current for other experiments was 10 μA), future experiments of the 12 GeV era will require the target to withstand beam currents of up to 60 μA. To handle this high current, the glass windows of the current cell design will be replaced by metallic ones. The metal windows introduce challenges as well: NMR RF field cannot penetrate metal parts, and cannot be used to reliably determine the target polarization. It is consequently important to have another polarimetry which can operate locally along the glass transfer tube. The Pulsed NMR (PNMR) method was developed for this purpose.

6.4.1 Pulse NMR Principle

As described in Section 6.2, the NMR frequency sweep is a method to record a spectrum in the continuous wave mode by applying monochromatic RF radiation to a sample and varying its frequency to locate absorption maximum. Whereas, Pulse NMR uses a radiation right at the absorption maximum and record the spectra.

When magnetization is created inside a magnetic field, there exists a macroscopic magnetization vector parallel to the applied field. This magnetization is a result of the individual orientation of each nucleus being quantized with respect to the static magnetic field. The macroscopic magnetization obeys the Larmor relation and precesses about any static magnetic field. The precession occurs with a constant cone angle in the absence of external work or friction. Once the rotation field is removed, the spin or magnetization decays back to equilibrium by transmitting energy to the surrounding. If we apply a magnetic field rotating at the Larmor frequency in the plane perpendicular to the static field, we can cause the individual nuclear magnetic moments to flip which causes the magnetization to tip away from the static field.

The method of tipping the spins away from the static field is the same as for NMR.

However, instead of completely reversing the spin as in AFP, the magnetization is rotated by a desired amount by using an appropriate combination of the intensity and rotating field duration. If the RF is turned on at resonance for a time t_{pulse}, the magnetization vector will be rotated by an angle $\theta_{tip} = \frac{1}{2}\gamma H_1 t_{pulse}$ with H_1 the strength of RF field.

After the RF is turned off, the magnetization will precess freely and eventually return to equilibrium. If a coil is mounted perpendicular to the static field, the decaying magnetization can induce an RF current at the Larmor frequency. The signal induced in the coil is a free precession signal and its decay is called free induction decay (FID).

The FID induces a signal in the PNMR pick up coil. The signal amplitude $S(t)$ is proportional to the ^{3}He polarization [70]:

$$S(t) \propto M_z \sin(\theta_{tip}) e^{-t/T_2}, \tag{6.17}$$

where M_z is the longitudinal magnetization (z-axis is pointing along the main holding field), θ_{tip} is the tipping angle between the magnetization and main field and T_2 is the transverse relaxation time, as described below.

6.4.2 Relaxation

There are two relaxation mechanisms happening to nuclear spin: the longitudinal and the transverse relaxations. Longitudinal relaxation described how fast spins go to equilibrium (a measure of the coupling of spin to its environment).

When spins are in the transverse plane, magnetic moments interact with one another and lose their phase coherence in the xy-plane (this plane is perpendicular to the main holding field along z-axis). The loss of transverse polarization is characterized by the time constant T_2, called spin-spin or transverse relaxation time. T_2 decay is not due to the tilting of the magnetization vector away from the transverse plane, however. It is due to the interaction of all of spins dephasing from each other. The main field in the coil area is not perfectly uniform so ^{3}He in different parts of the coil

precess at slightly different frequencies and become out of phase with one another, thereby gradually decreasing the net magnetization.

6.4.3 PNMR Setups

There are two designs for the PNMR method. The first design uses an oscilloscope to record data. This setup can record the data very fast but it cannot handle low signal very well. The second design is an improved version of the first design. It uses a Lockin amplifier and a DAQ card to record signals and it can improve the signal-to-noise ratio. I will discuss the setup and results for each design below.

The Oscilloscope Setup

The PNMR system schematic with the oscilloscope setup is shown in Fig. 6-6.

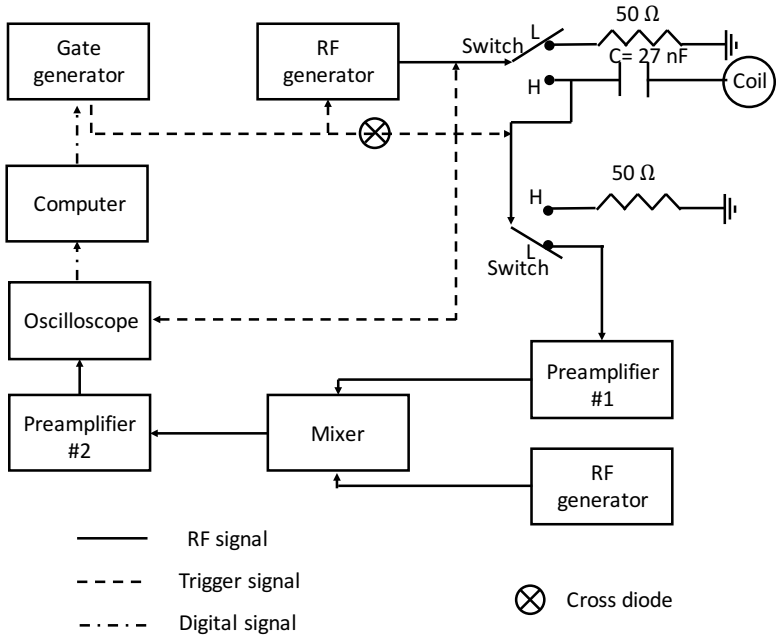

Figure 6-6: PNMR oscilloscope setup at JLab. The signal is controlled by the trigger from the gate generator. The output signal is recorded by an oscilloscope and then transferred to the acquisition computer.

Labview sends a software trigger to the gate generator (which generates a square

wave, TTL signal). This gate controls the function generator, switches and the oscilloscope. The TTL signal has a high, and a low signal, and based on low or high, switches either connect to 50 Ω terminal or connect to other instruments. If the TTL signal is high, the function generator will receive a TTL trigger from the gate generator. The function generator then sends a sine signal at Larmor frequency at $\sim$ 81 kHz to the PNMR coil. When the TTL signal is low, a FID signal from the coil passes the lower switch, then goes through the rest of the setup including Preamplifier #1 and the mixer. After passing through Preamplifier #2, the signal is in the radio frequency range and is sent to the oscilloscope. Data recorded by the oscilloscope are then sent to the computer.

In order to test this new polarimetry, several tests were conducted and compared with AFP-NMR. First, both NMR and PNMR coils are mounted on the target chamber. The expected relation between the two polarimetries is linear, which we verified, see Fig. 6-7. The reason for linearity is that the PNMR and NMR signals are in polarization equilibrium and the polarizations at these two locations are almost the same (since the coils are located near each other) on the target chamber. This measurement confirmed the reliability of our new polarimetry.

During actual 12 GeV experiments in the future, the PNMR pick-up coil will be mounted along the transfer tube in order to minimize background introduced by electrons rescattering off the coil[1]. Therefore, another measurement was done with the PNMR coil located on the transfer tube and the NMR coils located on the target chamber, see in Figs. 6-8 and 6-9. The nonlinear behavior in Fig. 6-8 is due to the fact that the initial polarization from these two locations are not in equilibrium. The polarized gas moves from the pumping chamber to the target chamber via diffusion if there is no convection. Due to the long diffusion time, polarizations at the two locations are not the same, which explains the reason why signals detected by two pick-up coils are not linear in proportion. If the gas is circulated by convection, then the polarization at the target chamber is expected to achieve equilibrium quickly with

[1]During experiment E97-110, it was found that events scattering off the NMR pickup coils caused some background.

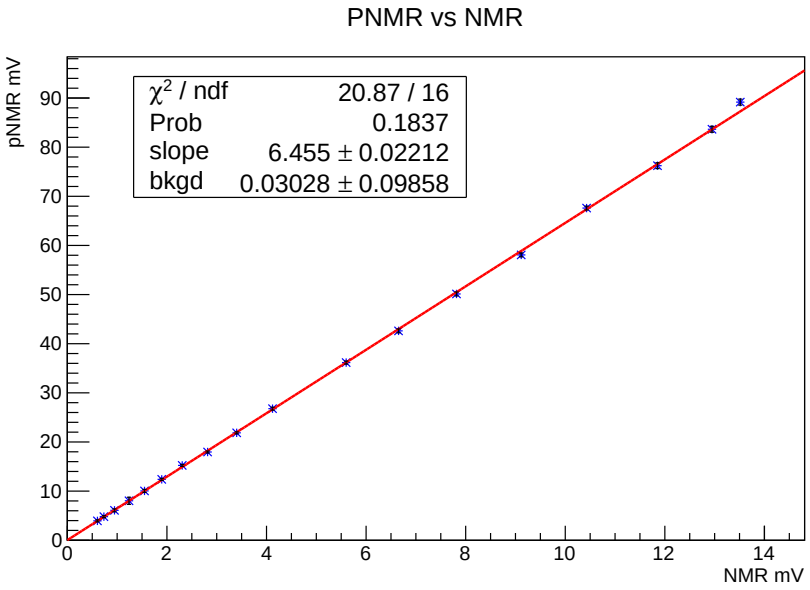

Figure 6-7: PNMR vs NMR signals when both PNMR and NMR coils are located on the target chamber. This measurement was performed during a "hot spindown", which is the polarization decay process when there is no optical pumping and the oven is kept at high temperate, and the convection was not occuring. Measurements were done every two hours.

the one in the transfer tube. In this case, the linear relationship is restored, as shown in in Fig. 6-9. Results shown in Fig. 6-9 indicate that PNMR can be used to provide reliable measurements on the target chamber polarization during actual experiment.

Lockin Amplifier with DAQ Card Setup

In the second setup, a Lock-in amplifier is used to detect the signal. Backgrounds at frequencies other than the signal frequency can be attenuated and the signal-to-noise ratio can be improved.

The PNMR system schematic with Lockin Amplifier and DAQ card is shown in Fig. 6-10.

Several measurements were done to test this new configuration. Unfortunately, they are not linear. Fig. 6-11 show the non-linearity of the measurement using DAQ card and Lockin Amplifier. More works need to be done to make the new system work and achieve our polarimetry uncertainty goal.

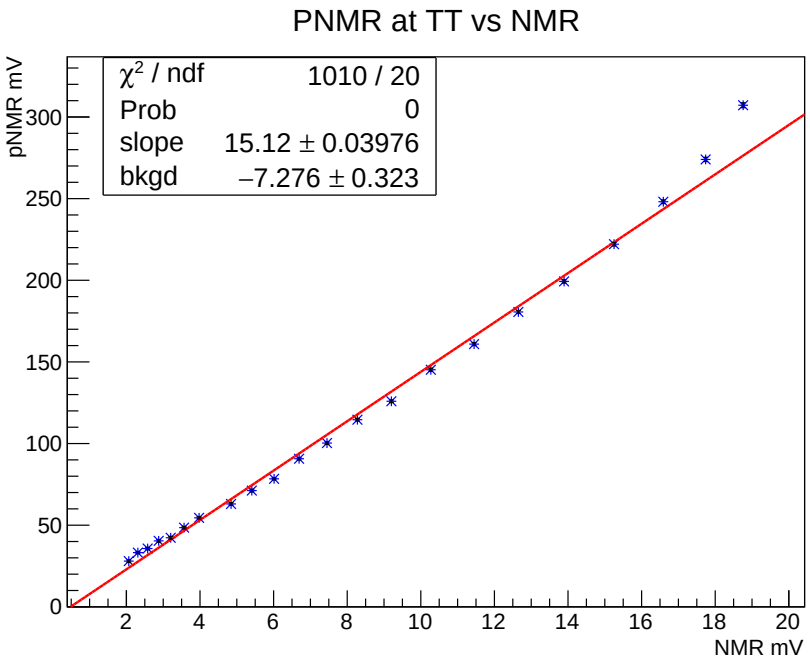

Figure 6-8: PNMR vs NMR Polarimetry signals for the case where the PNMR coil was at the transfer tube and NMR coils at target chamber. This measurement was performed during a "cold spindown", which is polarization decay as a function of time when there is no optical pumping, the oven is kept at room temperature, and convection is not occuring. Measurements were done every two hours.

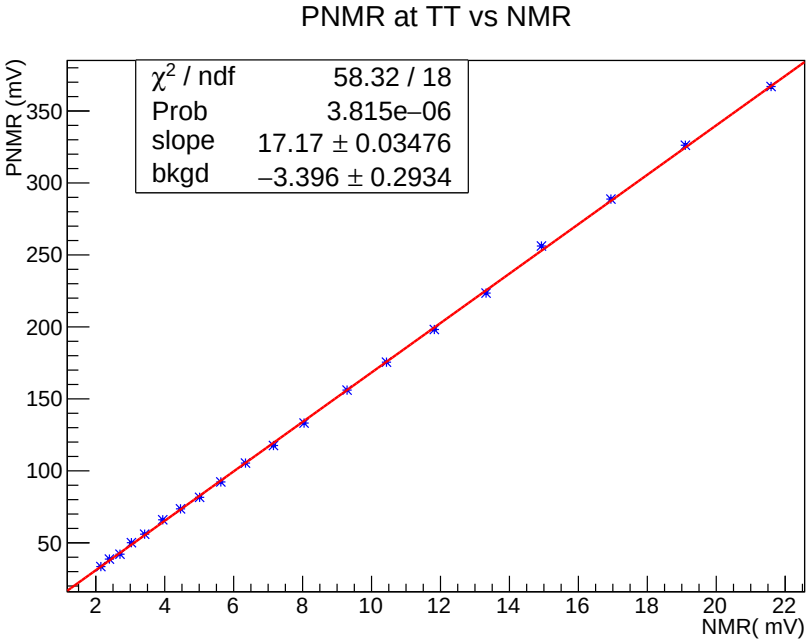

Figure 6-9: Same setting as Fig. 6-8 but with convection enable.

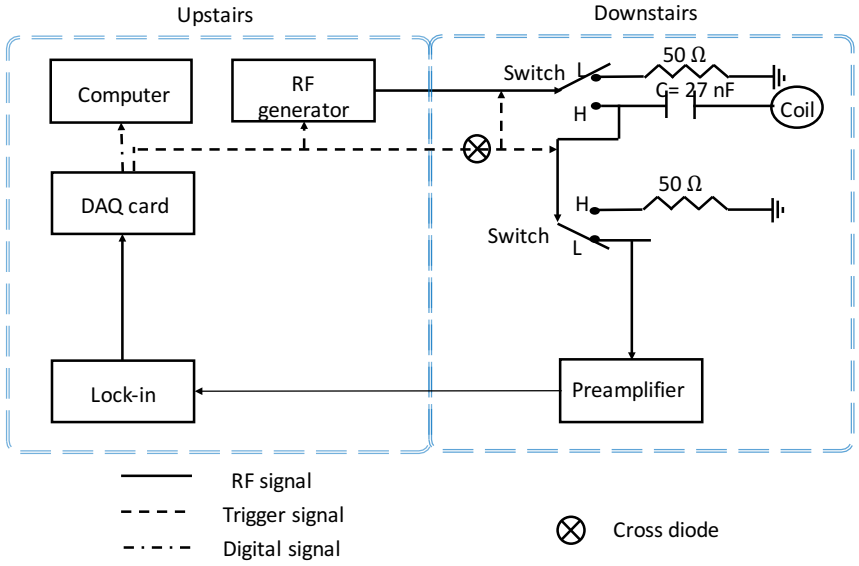

Figure 6-10: PNMR lockin setup at JLab. The signal is controlled by the trigger from the DAQ card. The output signal is recorded by a Lockin amplifier and then transferred to the DAQ card.

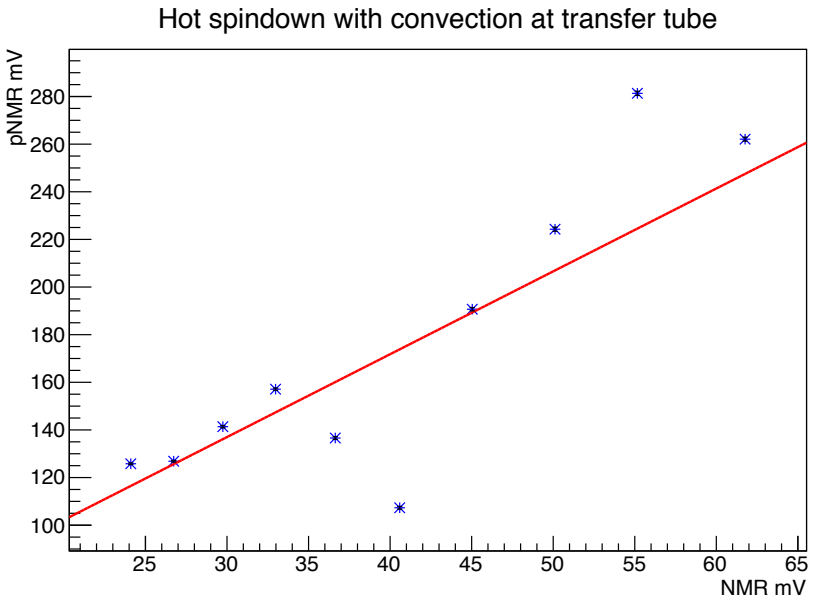

Figure 6-11: PNMR vs NMR measurements using DAQ and Lockin.

6.5 Conclusion

The JLab polarized ^{3}He target had a world-record performance during the 6 GeV era. R&D activities are ongoing to upgrade the target for the 12 GeV program. Initial tests of the convection cells and the pulsed NMR system have been made and proven successful. Full polarization tests and systematic studies are being studied further by new students. The target is ready for the A_1^n experiment and it will run from November 25, 2019 to May 6, 2020.

Appendix A

Appendix

A.1 Acceptance cut on the focal plane

A.1.1 Acceptance cut on the focal plane

A six-corner polygon is used to define the 2D cut on the focal plane. The corners are given in Table A.1

Corner	y_{fp}		ϕ_{fp}	
	δ_{tg}	offset	δ_{tg}	offset
1	-0.227484	0.009650	-0.120625	0.027118
2	-0.162115	-0.017178	-0.088537	0.012184
3	0.203004	-0.015755	0.209205	-0.020337
4	0.524234	0.012906	0.677652	-0.029080
5	-0.260981	0.024819	0.105192	0.044547
6	-0.394433	0.020599	-0.057926	0.047079

Table A.1: Acceptance cuts at focal plane. We make an assumption that inside this cut the acceptance is equal to one. An event passing this cut is considered to be a good event.

A.2 Cuts Applied for Asymmetry and Cross Section Analysis

Due to the defective Septum magnet, the number of events that survive at the detector is much smaller compare to that of second period. For cross section and asymmetry analysis, different cuts are applied. The cuts applied for asymmetry analysis are listed as follows:

1. Cherenkov cut: $350 < R.cer.asum_c < 100000$.

2. Loose shower cut: $E.ps.e > 10$ and $E.sh.e > 10$.

3. $(DR.evtypebits\&(1 \ll 1)) > 0$

4. $R.tr.n = 1$

5. Six-corner polygon acceptance cut at focal plane, as mentioned in the previous section.

6. Momentum cut: $-2.5 \leq \delta p \leq 3.5$ which is wider than the optic optimization range $(-2.0 \leq \delta p \leq 3.0)$.

For cross section all above cuts are applied, and an additional cut on the reconstructed angles (θ_{tg}, ϕ_{tg}) was applied. These cuts are listed in Table 4.4. This additional cut makes the number of events that pass all cuts to be much less than that of asymmetry analysis.

A.3 Spectrometer Acceptance

As mentioned in the cross section analysis (Chapter 4), the solid angle acceptance $\Delta\Omega$ is determined from simulation. Due to the fields created by the spectrometer magnets, the acceptance may not coincide with the geometrical aperture of the spectrometer. The acceptance instead depends on the particle's trajectory, momentum

and interaction vertex. Hence, the acceptance is determined from a Monte Carlo simulation.

In the simulation [62], random trajectories are generated that cover an illuminated area that is larger than the actual acceptance in the momentum and the solid angle. The simulation uses the forward transport matrix obtained from optic study and a set of analysis cuts (see Table 4.4) to determine if a randomly generated ray reaches the spectrometer's focal plane. The acceptance is then extracted by forming the ratio of number of events that pass through the spectrometer apertures and analysis cuts, to the total number of generated events.

Bibliography

[1] M. Gell-Mann, *Physics Letters* **8**, 3 (1964).

[2] G. Zweig, *CERN Report No..8182/TH.401.*

[3] M. J. Alguard, *et al., Phys. Rev. Lett.* **51**, 1135 (1983).

[4] J. Ashman, *et al., Phys. Lett. B* **206**, 364 (1988).

[5] S. Kuhn *et al., Prog. Part. Nucl. Phys.* **63**, 1 (2009).

[6] V. A. Sulkosky, *Ph.D thesis*, College of William and Mary, Williamburg, Virginia (2007).

[7] E. Rutherford *Philosophical Magazine* **6**, 21 (1911).

[8] N. F. Mott, H. S. W. Massey *The Theory of Atomic Collisions. (Third Edition), Oxford University Press*, New York (1965).

[9] J. D. Bjorken, E. A. Paschos, *Phys. Rev.* **185**, 1975 (1969).

[10] A. W. Thomas, W. Weise, *The Structure of the Nucleon,* Wiley-Vch, Berlin, Germany, 2001.

[11] J. Callan, Curtis G. and D. J. Gross, *Phys. Rev. Lett.* **22**, 156 (1969).

[12] Y. Dokshitzer, *Sov. Phys. JETP* **46**, 1649 (1977); V. N. Gribov and L. .N. Lipatov, *Sov. Nucl. Phys.* **15**, 438 and 675 (1972); G. Altarelli, G. Parisi, *Nucl. Phys.* **B126**, 298 (1977).

[13] K. G. Wilson, *Phys. Rev.* **179**, 1499 (1969).

[14] D. Drechsel and L. Tiator, *J. Phys.* **G18**, 449 (1992).

[15] D. Drechsel, S. S. Kamalov, and L. Tiator, *Phys. Rev.* **D63**, 114010 (2001).

[16] W. Marciano and H. Pagels, *Phys. Rept.* 3**6**, 137 (1978).

[17] M. Tanabashi *et al.* (Particle Data Group), *Phys. Rev. D* **98**, 030001 (2018).

[18] S. Scherer, *Adv. Nucl. Phys.* **27**, 277 (2003).

[19] J. Gasser, M.E. Sainio, and A. Vars. Nucleons with chiral loops. *Nuclear Physics B,* 307(4):779-853, 1988.

[20] V. Bernard, N. Kaiser, and ULF-G. Meißner. Chiral dynamics in nucleons and nuclei. *International Journal of Modern Physics E,* 04(02):193-344, 1995.

[21] T. Becher and H. Leutwyler. Baryon chiral perturbation theory in manifesly lorentz invariant form. *The European Physical Journal C - Particles and Fields,* 9(4):643-671, Jul 1999.

[22] X.-D. Ji, C.-W. Kao and J. Osborne, *Phys. Lett.* **B472**, 1 (2000).

[23] S. B. Gerasimov, Yad. Fiz. **2**, 839 (1965).
S. D. Drell and A. C. Hearn, *Phys. Rev. Lett.* **162** 1520 (1966).

[24] R. Shankar, *Princiles of Quantum Mechanics*, New Haven, Connecticut (1994).

[25] F. E. Low, *Phys. Rev.* **96**, 1428 (1954).
M. Gell-Mann, M. Goldberger and W. Thirring, *Phys. Rev.* **95** 1612 (1954).

[26] M. Anselmino, B. .L. Ioffe, and E. Leader, *Sov. J. Nucl. Phys.* **49**, 136 (1989).

[27] X.-D. Ji and J. Osborne, *J. Phys.* **G27**, 127 (2001).

[28] J. D. Bjorken, *Phys. Rev.* **148**, 1467 (1966).

[29] U. Stiegler, *Phys. Rep.* **277**, 1 (1996).

[30] D. Drechsel, O. Hanstein, S. S. Kamalov and L. Tiator, *Nucl. Phys.* **A645**, 145 (1999).

[31] V. Burkert and Zh. Li, *Phys. Rev.* **D47**, 46 (1993).

[32] V. Bernard, N. Kaiser and U-G. Meissner, *Phys. Rev.* **D48**, 3062 (1993).

[33] M. Amarian *et al., Phys. Rev. Lett.* **89**, 242301 (2002).

[34] V. Sulkosky *et al., arXiv:1908.05709* (2019).

[35] K. Ackerstaff *et al., Phys. Lett.* **B444**, 531 (1998).

[36] V. Bernard, E. Epelbaum, H. Krebs, and U.-G. Meissner *Phys. Rev. D* **87**, 054032 (2013).

[37] V. Lensky, J. M. Alarcon, and V. Pascalutsa, *Phys. Rev. C* **90**, 055202 (2014).

[38] J. E. Clendenin, *et al.,* SLAC Publication SLAC-PUB-7619, 1997.

[39] J. Alcorn, *et. al., Nucl. Instr. Meth.* **A 522**,294 (2004).

[40] T. Holmstrom, private communication.

[41] C. Yan, Technical Report, Hall C Raster system - The second Generation, Jefferson Lab, (unpublished), (1997).

[42] J. Singh, Small Angle GDH Run Summary webpage, https://userweb.jlab.org/~singhj/runsummary/

[43] K. Nakamura *et al.* [Particle Data Group], *J. Phys. G* **37**, 075021 (2010).

[44] J. L. Friar, B. Gibson, G. Payne, A. Bernstein, and T. E. Chupp, *Phys. Rev. C* **42**, 2310, (1990).

[45] F. Colegrove, L. Schearer, and G. Walters, *Phys. Rev.* **132**, 2561, (1963).

[46] T. E. Chupp, M. E. Wagshul, K. P. Coulter, A. B. McDonal, and W. Happer, *Phys. Rev. C* **36**, 2244, (1987).

[47] V.R. Skoy, *et al., Nucl. Instr. Meth. in Phys. Res.* **A 501**,547-552 (2003).

[48] R. K. Ghosh, *Ph. D. thesis*, Princeton University, Princeton, New Jersey (2009).

[49] M. V . Romalis, *Ph. D. thesis*, Princeton University, Princeton, New Jersey (1997).

[50] Z. Wu, T.G. Walker, and W. Happer, *Phys. Rev. Lett.* **54**, 1921 (1985).

[51] T. G. Walker *at. al., Phys. Rev. A* **40**, 4959 (1989).

[52] L. Gamblin and T. R. Carver, *Phys. Rev.* **138**, A964, (1965).

[53] N. Liyanage, Technical Report, JLab-TN-01-049, Jefferson Lab, (unpulished), http://hallaweb.jlab.org/publications/Technotes/technote.html, (2001).

[54] N. Liyanage, Technical Report, JLab-TN-02-012, Jefferson Lab, (unpulished), http://hallaweb.jlab.org/publications/Technotes/technote.html, (2002).

[55] https://root.cern.ch/doc/master/classTMinuit.html

[56] https://www.jlab.org/accel/survalign/documents/dthalla/A879r.PDF

[57] J. Liu,*Ph. D. thesis*, University of Virginia, Charlottesville, Virginia (2017).

[58] https://hallaweb.jlab.org/experiment/E97-110/tech/firstperiod_normalization.pdf

[59] https://hallaweb.jlab.org/experiment/E97-110/tech/nitrogen_dilution.pdf

[60] A. Deur, Two step process for the rising tail background. E97-110 Technical Report, 2003. https://hallaweb.jlab.org/experiment/E97-110/tech/tech_notes.html

[61] http://hallaweb.jlab.org/experiment/E97-110/tech/ice_uncertainty.pdf

[62] A. Deur. Elastic cross section analysis. E94010 Technical Note E94010TN35. 2000.

[63] J. Chen, private communication.

[64] C. Peng,*Ph. D. thesis*, Duke University, Durham, North Carolina (2018).

[65] Y. Qiang, AIP Conf. Proc. 1182, 864 (2009).

[66] J. Singh, *et. al.,* AIP Conf. Proc. **1**149, 823 (2009).

[67] X. Zheng, *Ph. D. thesis*, Massachusetts Institue of Technology (2002).

[68] A. Abragam, *Principles of Nuclear Magnetism*, (Oxford University Press 1961).

[69] Q. Xin, *et. al., Phys. Rev. L* **107**, 072003, (2011).

[70] E. Fukushima, S.B.W. Roeder, *Experimental Pulse NMR: A Nuts and Bolts Approach*, (Westview Press 1993).

[71] https://www.minicircuits.com/pdfs/ZYSWA-2-50DR.pdf

[72] http://www.markimicrowave.com/assets/appnotes/mixer_basics_primer.pdf.

[73] http://www.minicircuits.com/pdfs/ZAD-8.pdf